DISSERTATION

# Experiments and FLUKA simulations of $^{12}$C and $^{16}$O beams for therapy monitoring by means of in-beam Positron Emission Tomography

ausgeführt zum Zwecke der Erlangung des akademischen Grades eines Doktors der technischen Naturwissenschaften unter der Leitung von

**Univ. Prof. Dipl.-Ing. Dr. techn. Hannes Aiginger**

E141
Atominstitut der Österreichischen Universitäten

eingereicht an der Technischen Universität Wien
Fakultät für Physik

von

**Dipl.-Ing. Florian Sommerer**

Matrikel Nr. 9625884

Untere Hauptstraße 27
3495 Rohrendorf

Wien, am 12. September 2007

*To my family and my friends*
*for their love, help and support*

# Kurzfassung

Seit 1997 wurden mehr als 350 Patienten an der $^{12}$C Ionentherapie-Pilotanlage an der Gesellschaft für Schwerionenforschung (GSI) in Darmstadt, Deutschland, behandelt. Die Therapie wird mit einem speziellen Positronen Emissions Tomographen (PET) überwacht, der vollständig in den Bestrahlungsplatz integriert ist. Die gemessene $\beta^+$-Aktivität entsteht durch inelastische Kernreaktionen zwischen den Ionen des Strahls und den Atomkernen des Patientengewebes. Da die Messung während der Bestrahlung durchgeführt wird, wird diese Methode "in-beam PET Monitoring" genannt. Das grundlegende Prinzip dieser Methode ist ein Vergleich zwischen der gemessenen $\beta^+$-Aktivität und einer Simulation dieser Aktivität. Derzeit werden diese Simulationen mit dem PETSIM Code durchgeführt, der nur die Aktivitätsproduktion von $^{12}$C Ionenstrahlen behandeln kann.

In zukünftigen Therapiezentren wie dem Heidelberger Ionenstrahl-Therapiezentrum (HIT), Heidelberg, Deutschland werden neben $^{12}$C Strahlen auch Protonen, $^3$He und $^{16}$O Strahlen zur Verfügung stehen und die Überwachung der Bestrahlung soll mittels in-beam PET durchgeführt werden.

Weil PETSIM nicht leicht auf andere Ionenstrahlen erweitert werden kann, soll es durch einen anderen Code, der in der Lage ist die $\beta^+$-Aktivitätsproduktion von allen in der Therapie verwendeten Ionen vorherzusagen, ersetzt werden. Der Monte Carlo Teilchentransport Code FLUKA ist ein geeigneter Kandidat für diesen Zweck, da der FLUKA Code

- Computertomogramme importieren und verarbeiten kann

- bereits gute Ergebnisse für die Vorhersage der durch Protonenstrahlen erzeugten $\beta^+$-Aktivität gezeigt hat

- gute Ergebnisse in der Berechnung der von Ionenstrahlen erzeugten Dosis erzielt

- kürzlich um eine Schnittstelle zu einem Eventgenerator erweitert wurde, der niederenergetische inelastische Kernreaktionen behandeln kann

Das Ziel der vorliegenden Arbeit war es, die Eignung von FLUKA für die in der in-beam PET Überwachung einer Therapie mit $^{12}$C und $^{16}$O Strahlen notwendigen Simulationen der $\beta^+$-Aktivität zu untersuchen.

Dafür wurden homeogene Targets aus Wasser, Polymethylmethacrylat (PMMA) und Graphit mit $^{12}$C Strahlen von 260 $A$MeV und $^{16}$O Strahlen von 200, 250, 300, 350 $A$MeV bestrahlt. Für $^{16}$O Strahlen wurden solche Experimente noch nie zuvor durchgeführt.
Der Aufbau der $\beta^+$-Aktivität wurde während der Bestrahlung mit der PET Kamera gemessen. Die Auswertung erfolgte nur in den Spillpausen, da während der Strahlextraktion das PET Signal durch prompte $\gamma$-Strahlung aus den inelastischen Kernreaktionen gestört wird.

Nach dem Ende der Bestrahlung wurden die Messungen 30 Minuten weitergeführt. Die erhaltenen Zerfallskurven wurden analysiert um das Mengenverhältnis der $\beta^+$-aktiven Nuklide zu erhalten. Auf Basis dieses Verhältnisses wurde die relative Produktion von $\beta^+$-aktiven Nukliden pro Spill berechnet. Die Effizienz der PET Kamera für Koinzidenzdetektion wurde mit eine $^{22}$Na Quelle gemessen. Damit konnte die relative Produktion in die absoluten Werte umgerechnet werden.

Rückprojektionen wurden für zwei verschiedenen Zeitfenstern durchgeführt. Die Rückprojektion im ersten Zeitfenster beinhaltet alle Koinzidenzen während der Spillpausen. Zu dieser Zeit ist die Aktivität vom Zerfall kurzlebiger Nuklide dominiert. Das zweite Zeitfenster ist von 10 bis 20 Minuten nach Bestrahlungsende definiert. Zu dieser Zeit ist die Aktivität vom Zerfall von $^{11}$C dominiert, damit konnte eine genauere Untersuchung der Verteilung dieses Nuklids durchgeführt werden.

Sowohl für $^{12}$C als auch für $^{16}$O Strahlen wurde die Position der Aktivitätsmaxima bestimmt. Für $^{16}$O Strahlen ist das Maximum während der Bestrahlung durch $^{15}$O dominiert, von 10 bis 20 Minuten nach Bestrahlungsende dominiert $^{11}$C. Da sich die Maxima von $^{11}$C und $^{15}$O an unterschiedlichen Stellen befinden, kann eine zeitliche Änderung der Position des Gesamtmaximums festgestellt werden. Diese zeitliche Änderung wurde untersucht. Zusätzlich wurde das Verhältnis der Höhe des Maximums zur Höhe des Plateaubereichs vor dem Maximum bestimmt und seine zeitliche Veränderung untersucht.

Vier PMMA Targets wurden mit $^{16}$O Strahlen mit benachbarten Energien bestrahlt und mittels in-beam PET gemessen. Die Energieunterschiede entsprechen Reichweitendifferenzen im Bereich von weniger als einem Millimeter. Es konnte gezeigt werden, dass es möglich ist die Positionsunterschiede der Aktivitätsmaxima aufzulösen.

Die laterale Aufweitung der $\beta^+$-Aktiviät mit zunehmender Eindringtiefe wurde für alle Experimente berechnet. Zusätzlich wurde mittels einer Wassersäule variabler Länge die Strahlaufweitung eines $^{16}$O Strahls mit 350 $A$MeV gemessen und mit der Aufweitung der $\beta^+$-Aktivität verglichen.

Die so gewonnenen Daten wurden für einen Vergleich mit den FLUKA Simulationen benutzt. Dabei wurde besonderes Augenmerk auf den neuen Eventgenerator BME gelegt, der die niederenergetischen inelastischen Kernreaktionen unter 100 $A$MeV behandelt. Ohne BME kann unter 100 $A$MeV keine $\beta^+$-Aktivität produziert werden.

Die Simulationen wurden mit verschiedenen Ansätzen durchgeführt. Jeder Ansatz war detaillierter als der vorhergehende. Eine Schnittstelle zwischen FLUKA und jenem Teil von PETSIM, der die Detektion und die Umwandlung in das auch im Experiment verwendete list-mode Datenformat durchführt, wurde programmiert. Damit war es möglich die Simulationen mit den selben Programmen auszuwerten, die auch zur Auswertung der Experimente benutzt werden. Dadurch konnten Unsicherheiten bei der Simulation der Detektion und bei der Rückprojektion ausgeschlossen werden.

Um die benötigte Rechenzeit zu verkürzen wurden die in FLUKA eingebauten Methoden zur Varianz-Reduktion (Biasing) verwendet. Die benötigten Rechenzeiten waren aber immer noch inakzeptabel lang, da aufgrund der Doppelkopfgeometrie der PET Kamera nur ein Bruchteil der simulierten Annihilationsphotonen den Detektor erreicht und deswegen Rechenzeit für die Produktion und den Transport von nicht detektierten Annihilationsphotonen aufgewendet wird. Deswegen wurde FLUKA um eine Biasing Methode erweitert, die es ermöglicht Annihilationsphotonen in eine bevorzugte Richtung, in diesem Fall die Detektorköpfe, zu lenken (decay direction biasing). Die Verwendung diese Methode brachte eine eklatante Verkürzung der benötigten Rechenzeit.

Eine gute Übereinstimmung zwischen gemessenen und simulierten Aktivitätsverteilungen konnte für die Experimente mit $^{12}$C Strahlen erzielt werden. Für $^{16}$O konnte gute Übereinstimmung der Aktivitätsverteilung nur für die höheren Energien erzielt werden. Die Verwendung von BME führte im Allgemeinen zu verbesserten Aktivitätsverteilungen in Bezug auf Position und Höhe des Maximums.
Wenn inelastische Kernreaktionen unter 100 $A$MeV in der Simulation nicht berücksichtigt werden, dann fehlt Aktivität vor dem Maximum. Dies ist besonders dramatisch für die Simulationen der 200 $A$MeV $^{16}$O Strahlen. Die Benutzung von BME verbessert zwar die Aktivitätsverteilung, aber nicht in genügendem Umfang.

Die absolute Anzahl an $\beta^+$-aktiven Kernen wurde simuliert und mit den Experimenten verglichen. Jene Simulationen, die ohne BME durchgeführt wurden zeigten eine Unterschätzung der Produktion von $\beta^+$-aktiven Nukliden. Jene Simulationen, die mit BME durchgeführt wurden zeigten zwar eine höhere Produktion von $\beta^+$-aktiven Nukliden, es werden aber noch immer zu wenige $\beta^+$-aktive Nuklide produziert um die experimentellen Werte zu erreichen.

# Abstract

Since 1997, more than 350 patients have been treated at the experimental $^{12}$C ion therapy facility at Gesellschaft für Schwerionenforschung (GSI), Darmstadt, Germany. The therapy is monitored with a dedicated positron emission tomograph, fully integrated into the treatment site. The measured $\beta^+$-activity arises from inelastic nuclear interactions between the beam particles and the nuclei of the patients tissue. Because the monitoring is done during the irradiation the method is called in-beam PET. The underlying principle of this monitoring is a comparison between the measured $\beta^+$-activity distribution and a simulated one. The simulations are presently done by the PETSIM code which is dedicated to $^{12}$C beams.

In future ion therapy centers like the Heidelberger Ionenstrahl Therapiezentrum (HIT), Heidelberg, Germany, besides $^{12}$C also proton, $^3$He and $^{16}$O beams will be used for treatment and the therapy will be monitored by means of in-beam PET.

Because PETSIM is not extendable to other ions in an easy way, a code capable to predict the $\beta^+$-activity distributions created by all ions of interest, including possible future ones, is needed to enable in-beam PET monitoring. A candidate for such a role is the multi purpose particle transport and interaction Monte Carlo code FLUKA, because:

- its ability to read and handle computed tomography (CT) data

- it shows good results in predicting the $\beta^+$activity induced by proton beams

- good results in calculating dose distribution in ion therapy

- its recently added interface with a module which is capable to handle nuclear reactions at low energies

The objective of this thesis is to investigate the ability of FLUKA to predict the $\beta^+$-activity distributions induced by $^{12}$C and $^{16}$O beams, necessary for in-beam PET.
Irradiations of homogeneous targets of water, polymethyl methacrylate (PMMA) and graphite were performed with $^{16}$O beams of 200, 250, 300 and 350 $A$MeV and $^{12}$C beams of 260 $A$MeV. In case of the $^{16}$O beams this was done for the first time. During the irradiation the build up of $\beta^+$-activity was measured. The evaluation of the build up could be done only during the pauses of the spills because during beam extraction the PET signal is compromised by prompt $\gamma$ from the nuclear reactions.

After irradiation end the measurement was continued for 30 minutes. By fitting the obtained decay curves the ratio between the number of the different $\beta^+$-active nuclei could be determined. On basis of this ratio the relative production of the individual $\beta^+$-active nuclei per spill could be calculated. The coincidence detection efficiency of the PET detector was measured with a $^{22}$Na source. Based on this measurement the absolute production of $\beta^+$-active nuclei could be calculated.

Backprojections of the $\beta^+$-activity were computed at different time windows. The first time window included all annihilations during the pauses of the spills. At this time the nuclides with short half-lives dominate the activity. The second time window was from 10 to 20 minutes after irradiation end. At this time for all targets the activity is dominated by $^{11}$C which allows to investigate deeper the distribution of this nuclide.

For both beams the positions of the $\beta^+$-activity peaks was determined. For $^{16}$O beams the activity in the peak is dominated by $^{15}$O during the irradiation and by $^{11}$C in the time from 10 to 20 minutes after the irradiation, because the $^{15}$O is already decayed. Because the $^{15}$O and the $^{11}$C activity have peaks at slightly different positions, the position of the resulting $\beta^+$-activity changes over time. This peak shift was investigated. Furthermore the peak to plateau ratio of the activity distributions and its time dependency was investigated.

Four PMMA targets were irradiated with $^{16}$O beams of energies corresponding to less than 1 millimeter difference in range of the primary particles. Aim of this experiment was to investigate if the activity distributions can be resolved, which was successfully demonstrated.

For all experiments the lateral broadening of the $\beta^+$-activity in dependency of the penetration depth was calculated. An additional experiment with an $^{16}$O beam of 350 $A$MeV on a water target of variable length was performed and the broadening of the beam was measured. The broadening of the beam was compared to the broadening of the $\beta^+$-activity.

The experimental data was used for benchmarking FLUKA and its implemented nuclear reaction modells. Of special interest was the performance of the recently added event generator BME, which handles nucleus-nucleus interactions below 100 $A$MeV. Without BME no $\beta^+$-activity can be created below this energy.

The simulations were done in several consecutive approaches, each more sophisticated then the one before. FLUKA was interfaced with the part of PETSIM which modells the detector response and stores the detected events in list mode data format. This enables to process the simulated data exactly the same way than in the experimental case and avoids uncertainties due to the detection and backprojection.

To reduce the computing time, full advantage of the biasing options in FLUKA was taken which improved the computing time but the simulations where still too time consuming. Because of the double head geometry of the in-beam PET only a small fraction of the created annihilation photons can be detected. Because most of the annihilation photons produced are

not detected, a lot of computing time is wasted. To futher speed up the simulations decay direction biasing for annihilation photons was introduced. This biasing preferentially emits the annihilation photons into a wanted direction, i.e. the detector heads. The use of this biasing additionally with other standard biasing methods brought a dramatic improvement in terms of computing time.

Good agreement between measured and simulated $\beta^+$-activity distributions could be obtained for the simulations of the $^{12}$C beams. For $^{16}$O beams good agreement of the $\beta^+$-activity distributions could be obtained only for the higher energies. In general the results could be improved by the use of BME in terms of position and height of the $\beta^+$-activity peak.

If inelastic nuclear interactions below 100 $A$MeV are not included in the simulation, a lack of $\beta^+$-activity in front of the peak is found. This effect is dramatic in the simulation of the 200 $A$MeV $^{16}$O beam. The use of the BME event generator improved the $\beta^+$-activity distributions. However, BME does not produce enough nuclei to created realistic $\beta^+$-activity distributions for this low energy.

The absolute amount of $\beta^+$-active nuclei was simulated and compared to the experiments. The simulations without BME showed a too low production of $\beta^+$-emitters. In the simulations including BME the amount of $\beta^+$-active nuclei increased compared to the simulations without BME but still the production is too low.

# List of Abbreviations

| | |
|---|---|
| $A$MeV | Mega electron Volt per mass number |
| BME | Event generator based on the Boltzmann Master Equation Theory |
| CT | Computed tomography |
| DKFZ | Deutsches Krebsforschungszentrum |
| FLUKA | Fluktuierende Kaskaden, multi purpose particle transport code |
| FOV | Field of view |
| FWHM | Full with of half maximum |
| FZD | Forschungszentrum Dresden - Rossendorf e.V., Dresden, Germany |
| GSI | Gesellschaft für Schwerionenforschung, Darmstadt, Germany |
| HIT | Heidelberger Ionentherapie Zentrum |
| IDL | Interactive Data Language, data analysis software |
| in-beam PET | PET during ion beam irradiation |
| LOR | line of respons |
| PET | Positron Emission Tomography |
| PETSIM | Monte Carlo code for calculating the $\beta^+$-activity in $^{12}$C therapy at GSI |
| PMMA | polymethyl methacrylate (Plexiglas$^{\circledR}$) |
| ROOT | Object-oriented data analysis framework |
| voxel | A volume element representing a value on a regular grid in three dimensional space |

# Contents

# Chapter 1

# Introduction

In Europe, the disease which is the reason for the second most causes of death after cardio-vascular diseases, is cancer. At the time of diagnostics about 58 % of the tumors are localized and have not formed metastases yet. About 22 % of all patients can be cured with surgery, 12 % with radiotherapy and about 6 % by a combination of both [GSI99]. However, the local treatment fails for about 18 % of the patients which corresponds to about 280 000 deaths per year in Europe [Sch96a]. A part of these patients could be cured if local tumor treatment techniques could be improved.

The treatment with heavy charged particles i.e. protons and ions up to about $^{16}O$ has the potential to improve present treatment methods. The rationale for using protons and ions is the favorable depth dose profile as can be seen from figure 1.1. At high energies the energy loss is low leading to an almost constant plateau in the entrance channel. At the end of the particle range the dose rises and drops sharp afterwards. This is often called "inverse depth dose profile" with respect to the depth dose profiles of photons and electrons. Variation of the beam energy allows to precisely locate the sharp dose maximum within the tumour. Proton and ion beams offer additionally less lateral scattering and higher biological efficiency.

The first proposal for a treatment with protons was from R. R. Wilson in 1946 [Wil46]. Only a few years later, in 1954, the Lawrence Berkeley Laboratory started the first treatment with protons and later also treatments with He, Ar, Si and Ne were performed. Since then the number of proton and ion centers has permanently grown. A historical review can be found in [Kra00]. A recent overview over proposed therapy centers and centers in operation can be found in [Sis05].
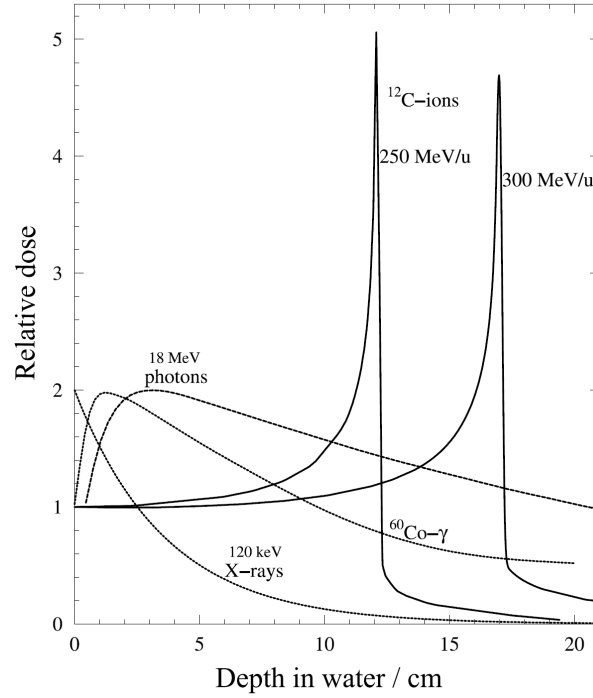
**Figure 1.1:** *Comparison between depth dose profiles of photons, $\gamma$ and X-rays from different radiation sources and $^{12}C$ beams of 250 and 300 AMeV (after [Kra00], image source [Par04]).*

## 1.1  Physical background

### 1.1.1  Interactions of ions with matter

**Energy loss of ions**

Heavy charged particles with kinetic energies in the range of therapeutic interest, i.e. from about 80 to 400 $A$MeV ($A$ indicates the mass number), loose their energy by inelastic collisions with the electrons of the target material. The differential energy loss per unit length dE/dx is called electronic stopping power and is described by the Bethe-Bloch equation [Bet30, Blo33]:

$$-\frac{\mathrm{d}E}{\mathrm{d}x} = 2\pi r_e^2 m_e c^2 N \frac{Z^2}{\beta^2} \left[ \ln\left( \frac{2m_e c^2 \beta^2 T_{max}}{I^2(1-\beta^2)} \right) - 2\beta^2 - 2\frac{C}{Z_t} - \delta \right] \qquad (1.1)$$

where $\beta$ is the velocity of the projectile and $Z$ is its charge. $r_e$ is the classical electron radius, $m_e$ the electron rest mass, $N$ is the electronic density, $T_{max}$ is the maximum energy that can be transfered in a single collision with a free electron, $I$ is the ionization potential and $Z_t$ is the atomic number of the target material. $C$ is a shell correction which takes into account that with lower energy of the beam particle the contribution of the inner shells decreases. $\delta$ is the correction for the density effect i.e. the effect that the medium is polarized by the traversing charged particle and this polarization screens the electrons of atoms farer away leading to a
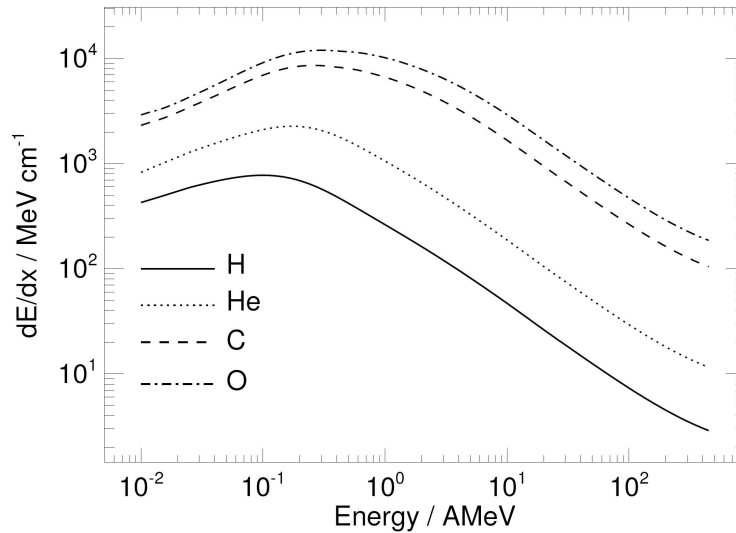
**Figure 1.2:** *Electronic stopping power of different ions of therapeutic interest in water [Par04].*

reduced energy loss.

At lower energies the positive charged ion starts to pick up target electrons and its effective charge $Z_{eff}$ is deceasing. This can be taken into account in equation (1.1) by substituting $Z$ with $Z_{eff}$ calculated by the Barkas formula [Bar56]:

$$Z_{eff} = Z(1 - e^{-125\beta Z^{-2/3}}) \tag{1.2}$$

Figure 1.2 shows the relation between the electronic stopping power and the particle energy for different ions of therapeutic interest. The $1/\beta^2 \simeq 1/E$ factor in equation (1.1) leads to an increasing energy loss with decreasing kinetic energy of the particle with a steep rise at low residual energies corresponding to the last few millimeters of the particle track. A the end of the range the stopping power drops due to the lower effective charge according to 1.2. This leads to the characteristic shape of the Bragg curve, i.e. a constant plateau at the entrance region followed by a sharp maximum at the end of the ion range, the so called Bragg Peak (cf. figure 1.1).

**Physical and biological dose**

The absorbed dose $D$ is defined as the energy deposited in the target per unit mass. Its unit is Gray (Gy), 1 Gy = 1 J kg$^{-1}$[ICR70]. The absorbed dose $D$ delivered by a mono-energetic ion beam can be described as:
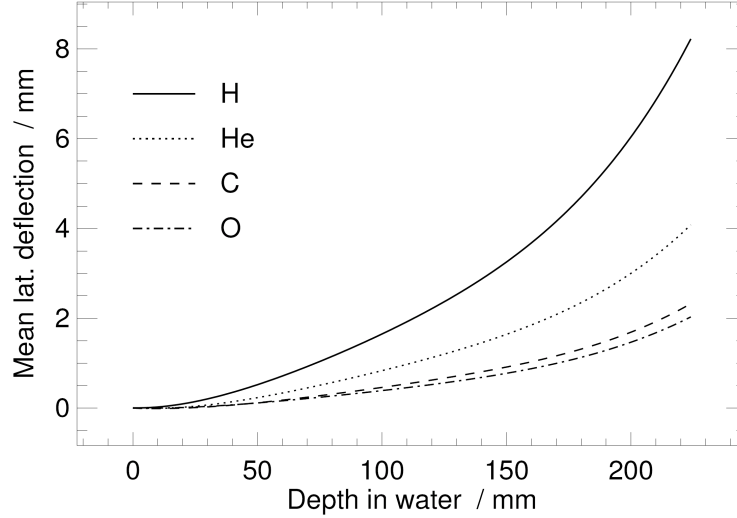
$$D = \frac{\Phi}{\rho} \frac{dE}{dx} \tag{1.3}$$

**Figure 1.3:** *Lateral deflection of proton and ion beams of therapeutic interest.*
*[Par04]*

where $\Phi$ is the fluence of the primary particles, $\rho$ is the density of the material and $\frac{dE}{dx}$ is the average energy loss.

However, in this description fragmentation reactions, induced by the beam particles, are neglected. To obtain a physical dose closer to reality nuclear reactions (see below) have to be taken into account in the fluence $\Phi$.

Two important quantities in this context are the linear energy transfer (LET) and the relative biological effectiveness (RBE). LET is a measure for the local energy deposition in matter defined up to a given maximal energy transfer, normally given in $eV$. A commonly used value is $LET_{100}$ which includes all transfered energy up to 100 eV which corresponds to a electron range in water of about 5 nanometer. If all energy losses are assumed to be local (i.e. $LET_{\infty}$), the LET becomes nominal identical to the stopping power.

The same physical dose, delivered by sparsely ionizing (low-LET) radiation like electrons or photons, leads to different cell damage than the irradiation with ions which are dense ionizing (high-LET radiation). This effect is described by the RBE which is defined as the ratio of a reference dose (normally X-rays) and the ion dose for the same biological effect (e.g. cell survival):

$$RBE_{ion} = \frac{D_{X-ray}}{D_{ion}} \bigg|_{isoeffect} \tag{1.4}$$

For carbon beams, depending on the concerned tumor cells, RBE values up to 5 can be reached in the Bragg peak. Figure 1.4 shows the correlation between physical and biological dose, cell survival and RBE. The picture on top shows the physical and biological dose for a spreadout Bragg Peak (SOBP, i.e. a superposition of several Bragg Peaks of different energies to obtain
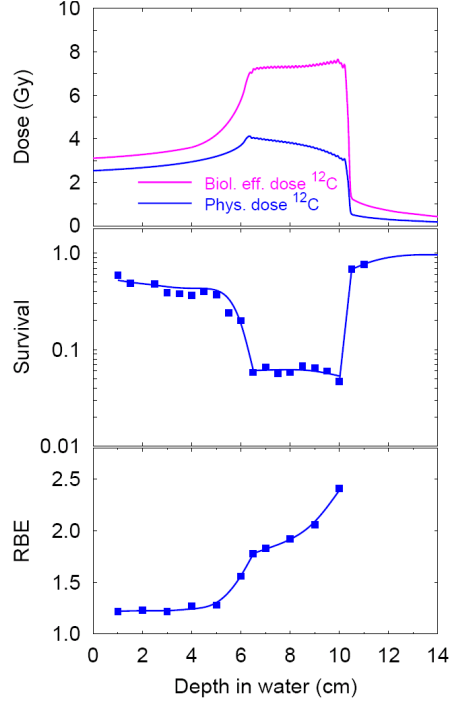
**Figure 1.4:** *Correlation between physical and biological dose, cell survival and RBE. Top picture shows the physical and biological dose for a spreadout Bragg peak ranging from 6 to 10 centimeter. The corresponding cell survival is shown in the middle picture and the RBE in the bottom picture. (after [Wey03], image from [Cre06])*

a uniform load with dose over the whole tumour) ranging from 6 to 10 centimeters. The corresponding cell survival is shown in the middle picture and the RBE in the bottom picture. It is worth to note that the RBE is energy dependent and therefore, the physical dose in the Bragg Peak is not constant in order to reach constant biological dose.

The knowledge of the the spatial dependency of $\rho$, $\Phi$, LET and RBE for all $N_z$ projectiles that can be created by nuclear fragmentation, leads to a realistic description of the biological dose:

$$D_{biol}(\mathbf{r}) = \frac{1}{\rho(\mathbf{r})} \sum_{z=1}^{N_z} \int_0^E \Phi(z, E, \mathbf{r}) \ LET(z, E) \ RBE(z, E) \ dE \qquad (1.5)$$

**Range straggling and lateral scattering**

When a charged particle is traversing a medium it undergoes not only the already mentioned inelastic collisions with the atomic electrons but also elastic Coulomb scattering with the nuclei of the target. This happens frequently and is therefore, called multiple Coulomb scat-

tering (MCS). The result of this scattering is a lateral spread and a divergence of the beam. Mathematically MCS can be described by the theory of Molière [Mol48]. For small deflection angles $\theta$ a Gaussian with a standard deviation $\sigma_\theta$ calculated by the empirical formula [Hig75]:

$$\sigma_\theta = \frac{14.1 MeV}{\beta pc} Z \sqrt{\frac{x}{L_{rad}}} \left(1 + \frac{1}{9} \log_{10} \frac{x}{L_{rad}}\right) \qquad (1.6)$$

gives a good approximation. $p$ is the momentum of the particle, $L_{rad}$ is the radiation length and x is the mass thickness of the medium. It can be seen that MCS increases with decreasing particle energy due to the $1/p$ dependency. Due to the $Z$ dependency the lateral broadening is more pronounced for lighter ions. Figure 1.3 shows the lateral broadening of beams of therapeutic relevance. It can be seen that proton beams show a much bigger lateral deflection than ions. This finding shows one advantage of ion over proton beams when high dose gradients are needed e.g. a tumor in close vicinity of organs at risk. However, even proton beams undergo much less lateral deflection than electron beams because of the higher mass. The gain in lateral broadening of O over C beams beams is only marginal.

The mean range of a monoenergetic beam of charged particles is defined as the penetration depth at which half of the initial partics have already stopped. Assuming continuous energy loss the range $R$ of a beam with an initial energy $E_0$ can be calculated by:

$$R = \int_{E_0}^0 \left(\frac{dE}{dx}\right)^{-1} dE \qquad (1.7)$$

However, statistical fluctuations of the energy loss cause a spread of the beam. This effect is called range straggling. It increases with the penetration depth and produces broader, less pronounced peaks when the initial energy increases (cf. figure 1.1). For different ions the range straggling shows a dependency of $1/\sqrt{A}$ [Kra00]. Therefore, heavier ions produce a narrower peak compared to light ions for corresponding penetration depths.

**Nuclear processes**

So far nuclear reactions were neglected. The most frequent nuclear interactions of ions of therapeutic relevance are peripheral collisions in which only a few nucleons are transferred. Nuclear fragmentation can be described by a two step process. First pre-fragments which are partially excited are produced in the collision ($10^{-22}$ seconds). In the second step lasting up to $10^{-16}$ seconds, the excitation energy is released by evaporation of nucleons. When the energy drops below the nucleon separation threshold $\gamma$-emission further de-excites the nucleus.

Because of the reaction kinematics, projectile fragments travel nearly in forward direction with almost the same velocity than the incident particle while the target fragments remain at the interaction point. Fragmentation reactions tend to add additional longitudinal and lateral spread to the beam. At the target entrance this is of minor importance but it adds a tail to the Bragg Peak. The amount of produced fragments increases with increasing mass of the primary beam. For carbon beams the fragmentation is still in acceptable limits if active beam

delivery systems like the raster scanning system are used.

Peripheral collisions can be classified by charge-changing reactions and non-charge-changing reactions. In charge-changing reactions protons are lost by the nucleus, in non-charge-changing reactions only neutrons are lost. Because the range scales with $A/Z^2$ a projectile that undergoes a charge-changing reaction has a longer range than the primary particle. For non-charge-changing reactions the fragment has a shorter range.
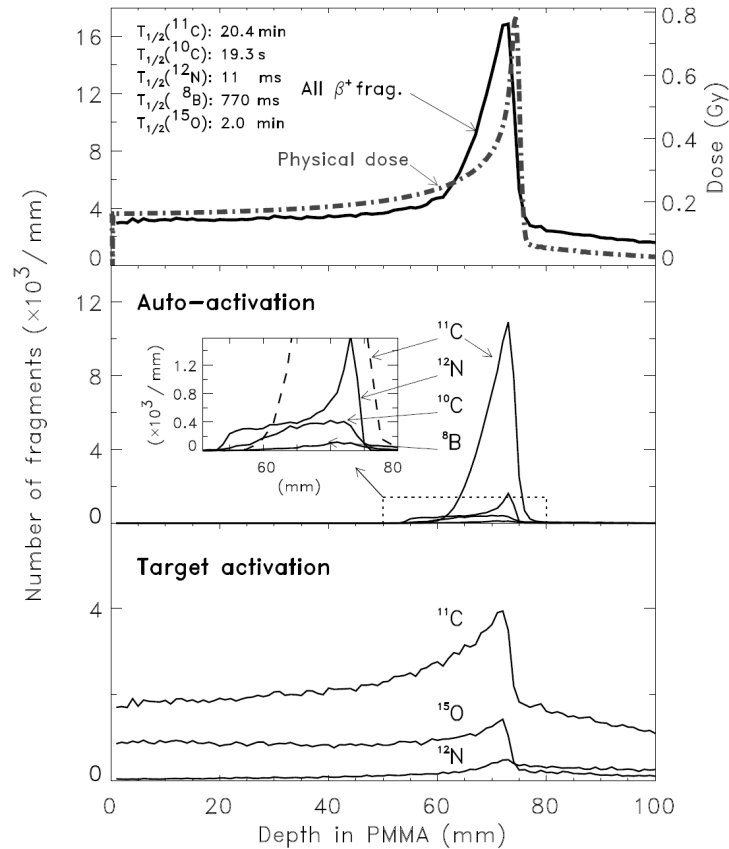


**Figure 1.5:** *Comparison between dose and fragmentation into $\beta^+$-active fragments for $^{12}C$. The top picture shows a comparison between the physical dose and all $\beta^+$-active fragments. The middle picture shows the $\beta^+$-active projectile fragments and the bottom picture the target fragments. The calculation of the $\beta^+$-activity was done by the dedicated Monte Carlo code [Pön04, Has96] used for the calculation of the activity in therapy. [Cre06]*

A part of the nuclei production in nuclear fragmentation reactions is $\beta^+$-active which offers the possibility of a noninvasive monitoring of the treatment by means of Positron Emission Tomography (PET). Figure 1.5 shows a comparison between dose and predicted $\beta^+$-active

fragments for $^{12}$C by means of the dedicated Monte Carlo code [Pön04, Has96] used for the calculation of the activity necessary for PET monitoring at GSI. It can be seen that the maximum of the $\beta^+$-activity lies in front of the Bragg peak. The top picture shows a comparison between the physical dose and all $\beta^+$-active fragments. The middle picture shows the spatial distribution of $\beta^+$-active projectile fragments and the bottom picture shows the distribution of $\beta^+$-active target fragments. It can be seen that projectile fragments contribute only in the peak and not in the entrance region.
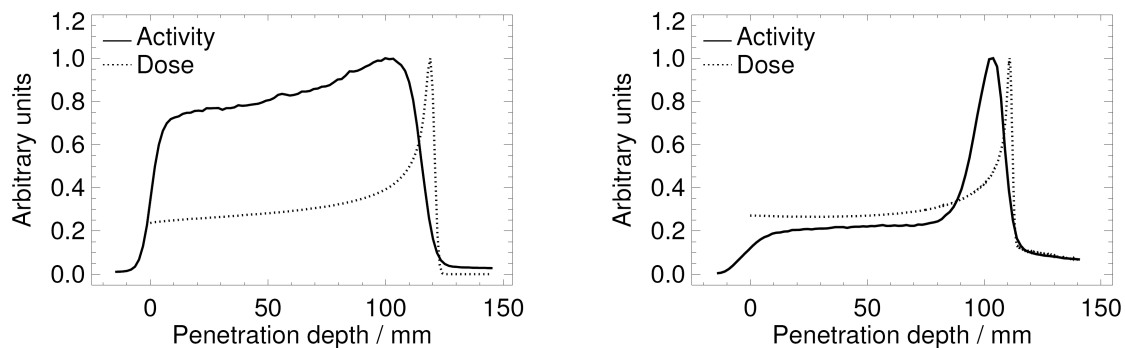


**Figure 1.6:** *graphics/protoncarbon.eps from [Par04]*

The $\beta^+$ active isotopes are produced by peripheral nuclear collisions. In such collisions is almost no momentum transfered therefore, the fragments of the target stay on their place and the fragments of the projectile move on with about the same kinetic energy than before the collision.

In a therapy with light ion beams (i.e. protons and He) no projectile fragmentation into $\beta^+$active nuclei is possible. Figure 1.6 shows a comparison between the dose and $\beta^+$-activity induced by proton beams (left side) and $^{12}$C beams (right side). It can be clearly seen that no pronounced peak is produced in case of the proton beam due to the lack of $\beta^+$-active projectile fragments. Nevertheless, a monitoring of the therapy by means of PET is possible [Par02, Par04, Par07]. A detailed description of the monitoring of an ion beam treatment by means of PET is described in section 1.2.

### 1.1.2 $\beta^+$-decay and Positron Emission Tomography

Positron Emission Tomography (PET) is an imaging technique in nuclear medicine which allows to detect biochemical processes in-vivo. It is applied typically for cardiology, neurology and oncology. It requires the use of $\beta^+$-active radio tracer like $^{18}$F-flouro-deoxy-glucose ($^{18}$F-FDG).

Nuclei with a neutron deficit can undergo $\beta^+$-decay by converting a neutron to a proton under emission of a positron $e^+$ and a neutrino $\nu_e$. The spectrum of the positron is continuous up

**Table 1.1:** *Properties of $\beta^+$-emitters relevant for in-beam PET. Left column gives the nuclide, middle column the half-lives and the right column the endpoint-energies [Nud07]. For $^8B$ no endpoint can be given because it decays to a very broad final state [Win06].*

| Nuclide | half-live | endpoint-energy |
|---|---|---|
| $^{15}O$ | 112.34 s | 1732 keV |
| $^{14}O$ | 70.61 s | 1808 keV |
| $^{13}O$ | 8.58 ms | 16743 keV |
| $^{13}N$ | 9.965 m | 1199 keV |
| $^{12}N$ | 11 ms | 16316 keV |
| $^{11}C$ | 1223.1 s | 960 keV |
| $^{10}C$ | 19.255 s | 1910 keV |
| $^9C$ | 126.5 ms | 15472 keV |
| $^8B$ | 770 ms | – |

to an maximum possible value (endpoint energy). Table 1.1 shows a list of half-lives and endpoint energies of $\beta^+$-active nuclei of special interest for ion therapy monitoring.

The most important nuclides for PET monitoring of ion therapy are $^{10}C$, $^{11}C$ and $^{15}O$ which have endpoint energies corresponding to positron ranges from 4.5 to 10 millimeters. Other isotopes which have shorter half-lives like $^{12}N$, $^9C$ or $^{13}O$ have higher endpoint energies and therefore, higher ranges. When a positron is emitted it undergoes numerous Coulomb interactions with the electrons of the tissue which are slowing it down and are changing its direction. At the end of its path the positron annihilates either directly with one electron or forms a bounded system with an electron. This system is called positronium and can have two atomic states, the ortho-positronium where the spins are parallel or the para-positronium where the spins are antiparallel. The para-positronium annihilates into two anti-parallel 511 keV photons, the ortho-positronium into at least 3 photons. The ortho-positronium has a one order of magnitude higher life-time and therefore, a high propability to undergo a fast para-annihilation into two photons. Therefore, the 3 $\gamma$ decay is suppressed and can be neglected. The emitted photons are not exactly collinear because of their non zero kinetic energy before the annihilation. This leads to an angular distribution of about 0.3° FWHM around 180°.

The photons are usually detected by detectors arranged in one or more rings. Each detector consists of a scintillation crystal for converting the photon to light and a photomultiplier tube (PMT) for converting the light into an electronic signal. When a photon enters the crystal it transfers its energy by Compton or photo effect to electrons. These electrons excite the atoms which emit visible light when going back to the ground state. In an ideal (i.e. an infinite) crystal the whole energy of the photons is absorbed. An important criteria for a scintillator is to have a high density $\rho$ and a high atomic number Z since the absorption probability by photoelectric effect is proportional to $\rho Z_{eff}^{3-4}$.

State of the art materials for crystals used in commercial PET-scanners are Bismuth Germanate ($Bi_4Ge_3O_{12}$, BGO) or cerium-doped $Lu_2SiO_5$ (LSO).

When the two photons hit two detectors within a short time window one can assign a line of response (LOR) by assuming the annihilation happened in the geometrical line between the two detectors. This would be called a true coincidence. Beside true coincidences there are also random, scattered and multiple coincidences which can compromise the image quality. A random coincidence occurs when two photons from different annihilation events are detected within the coincidence time window and contribute as continuous background to the image. To suppress random coincidences the coincidence time has to be chosen as small as possible. The limiting factor is the response time of the scintillator, for BGO a typical coincidence time window is 10 nanoseconds.

Multiple coincidences occur when more than one photon hits one crystal during the coincidence time. This can be corrected by setting a proper upper energy window.

The reason for scattered coincidences is that at least one of the two photons, coming from one annihilation event, is scattered at least once. Since scattered photons propagating in different direction than scattered they do not hit the right crystal which leads to a wrong LOR.

### 1.1.3   The GSI pilot project
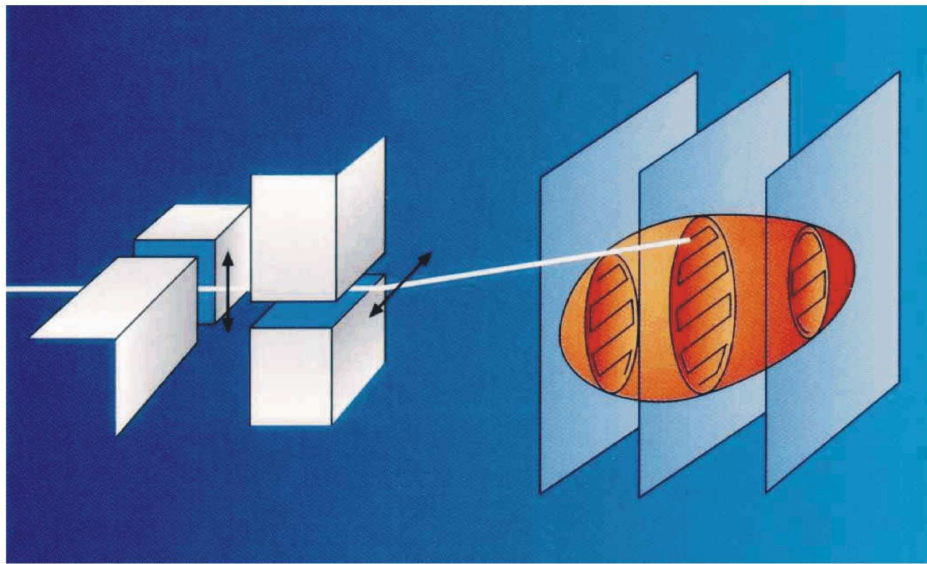


**Figure 1.7:** *The raster scanning technique. On the left side the magnets are shown which are used to deflect the beam in lateral direction. By active energy variation the penetration depth can be changed as indicated for three energies ion the right side of the picture. The combination of lateral deflection and energy variation allows to distribute uniform dose over the whole volume of the tumor. [Gun04]*

The heavy ion tumor therapy pilot project at GSI started in December 1997 and over 350 patients, mainly suffering from tumors in the head and neck region have been treated so far

with promising clinical results [Deb00, Sch02, Sch03]. This project is a cooperation between GSI, German Cancer Research Centre Heidelberg (DKFZ) and Forschungszentrum Dresden-Rossendorf (FZD) with the aim to build a clinic, Heidelberg Ion Therapy (HIT), in Heidelberg. This project has reached its final state now and the first treatment of patients at HIT is scheduled for winter 2007/2008.

The tree main innovations of this project are:

- three-dimensional conformal beam delivery based on a two-dimensional rasterscanning technique coupled to an active energy variation of the beam [Hab93] (cf. figure 1.7 and explanations in the capture)

- inverse treatment planning [Krä00] based on a radiobiological model developed at GSI [Sch96b]

- monitoring of the treatment by means of PET [Eng04]

## 1.2   In-beam PET

A common monitoring technique in conventional radiotherapy is electronic portal imaging [Ant02], which allows only to monitor the lateral position of the beam. The principle of this technique is to monitor the part of the primary beam which is penetrating into the patient. Because of the inverse depth dose profile of ions the primary beam is completely stopped in the tissue therefore, portal imaging is not possible. Monitoring the treatment with ion beams is highly desirable because the penetration depth is a much more crucial quantity compared to conventional radiotherapy. Due to the steep dose gradients, few millimeters shift of the penetration depth can lead to critical high dose at the healthy tissue or to too less dose in the tumor. This affects the treatment planning, the range uncertainties are presently around 1-3 % [Jäk01].

During the several weeks of fractionated treatment, range deviations can occur because of slight misspositioning or anatomical changes. Because the treatment plan is done only once prior to the first treatment, anatomical modifications cannot be discovered and corrected.
In order to discover these problems a three dimensional method is needed. At present the only feasible method is positron emission tomography.

Since 1997 at the experimental treatment facility at Gesellschaft für Schwerionenforschung (GSI), Darmstadt, Germany the treatment of more than 350 patients with $^{12}$C was monitored by means of PET. At the future therapy clinic in HIT in Heidelberg it is planned to monitor the treatment with different types of ions and protons by means of in-beam PET.

### 1.2.1   Background

The most straightforward way to enable PET monitoring is to use $\beta^+$-active beams. This would result in activity distributions with pronounced peaks dominated by the nuclei of the beam at the end of the particle range while $\beta^+$-activity due to fragmentation reactions would play a minor role. At Heavy Ion Medical Accelerator (HIMAC) in Chiba, Japan [Ura01] this was done by using $^{11}$C and $^{10}$C beams. Such beams create an activity of about $10^3$-$10^5$Bq Gy$^{-1}$cm$^{-3}$. The creation of radioactive beams is difficult because only a very small fraction of the primary beam is fragmented into the nuclei of interest and therefore, a huge effort has to be addressed to absorb and shield the primary beam and to clear, focus and re-accelerate the secondary beam.

An other way of using radioactive beams is to perform preliminary range measurements before the treatment with a stable isotope. This was investigated at the Lawrence Berkeley Laboratory [Lla88]. However, apart from the monitoring no other medical benefit can be expected from this technique. This and the higher costs make the use of radioactive beams less interesting.

An other way to enable PET monitoring is to measure the $\beta^+$-activity created by the inelastic nuclear interactions between the beam and the patients tissue. Because this activity is created anyway this method is non invasive and also more cost efficient than a solution with a radioactive beam. The disadvantage is the small amount of activity created: 1.3–1.8 kBq $Gy^{-1}cm^{-3}$ for $^{12}C$ beams and 5.3–7.5 kBq $Gy^{-1}cm^{-3}$ for proton beams [Fie06]. Because of the low activity and the blurring of the activity due to metabolic processes the PET measurement of the activity has to be done during irradiation (in-beam PET).

### 1.2.2   In-beam PET at GSI

At the treatment place at GSI a modified PET camera made of parts from an ECAT EXACT PET scanner (CTI PET Systems Inc., Knoxville TN) is installed to monitor the treatment with $^{12}C$ beams. The scanner is designed in double head geometry to not interfere with the beam and to enable flexible patient positioning. The two heads, each of $42 \times 21$ cm$^2$ size cover only 9 % of the solid angle. Every head has $4 \times 8$ block detectors of bismuth germanate (BGO) each of $54 \times 54 \times 20$ mm$^2$ size divided in $8 \times 8$ crystals per block, resulting in about $4.2 \cdot 10^6$ lines of response. The coincidence detection efficiency is about 2.2 % in the center of the field of view. The data acquisition from the manufacturer was modified to meet the requirements for in-beam PET. Scattered coincidences, i.e. coincidences where one or both photons are below the energy threshold are discarded. The time window for prompt and delayed coincidences is set to 12 ns the delay of the latter is 128 ns. The lower and upper energy thresholds are set to 250 keV and 850 keV respectively.

Figure 1.8 shows a picture of the treatment place. On bottom of the right site is the patient couch and on its end there is a mask which is used to fix the patients head. Above and below the mask there are the two heads of the detector. The arrow labeled *(a)* shows the beam direction. The PET can be moved towards the wall during patient positioning along the path indicated by *(b)*. Further it is possible to rotate the detectors 90° along *(c)* for monitoring treatments where the patient is fixed on a special treatment chair. The devices shown in the top corners are movable x-ray tubes for controlling the patient positioning.

### 1.2.3   Data Processing

The off-line tomographic reconstruction needs to discard all events during beam extraction because they are corrupted by prompt $\gamma$-rays from nuclear reactions between beam particles and target material. Therefore, the information about the beam status (i.e. on/off) is stored in the data sets. To allow reconstruction during different time intervals the data is stored in list mode i.e. a time stamp is inserted every 10 ms. To make an image fusion between the reconstructed 3D activity distribution and the CT the exact position of the camera is read out on-line. The reconstruction is performed on Cluster with 2.0 Intel Xeon processors running under Linux.
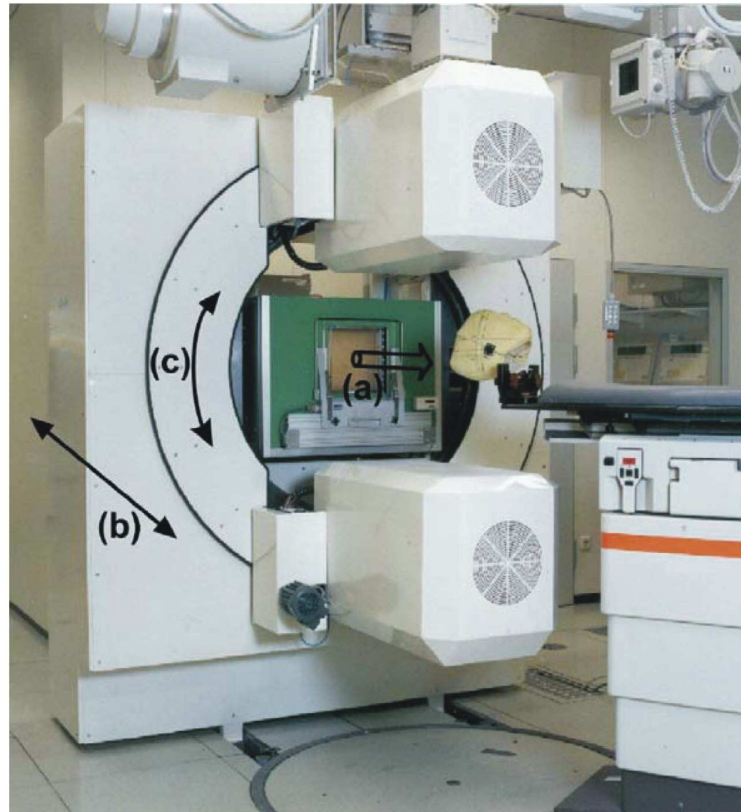
**Figure 1.8:** *The in-beam PET camera at GSI [Eng04]. The arrow (a) indicates the beam path, arrow (b) shows the horizontal moving, and (c) indicates a possible rotation of the detector heads for treatments with a treatment chair.*

The reconstruction of the data is done by a Maximum Likelihood Expectations Maximization algorithm [Pön03] then the contour plots PET images are merged with the CT to enable a comparison with the anatomical information.

The Maximum Likelihood Expectations Maximization algorithm is not the only available image processing algorithm. For special cases like phantom studies also a backprojection algorithm is available [Pön04]. This algorithm has the advantage of being faster and artifact free, if the activity distribution is restricted to the midplane between the two detector heads.

## 1.2.4 Clinical routine

The clinically relevant parameters which can be monitored by means of in-beam PET are: the particle range, the lateral field position and local dose values. Because the spatial activity distribution does not match the dose distributions the reconstructed activity is compared with a simulated one. This simulation depends on the patients CT, the treatment plan and the time course of the irradiation. The code used for simulating the $\beta^+$-activity [Pön04] (in the following called PETSIM code) is dedicated to $^{12}$C ions. It takes into account: the transport
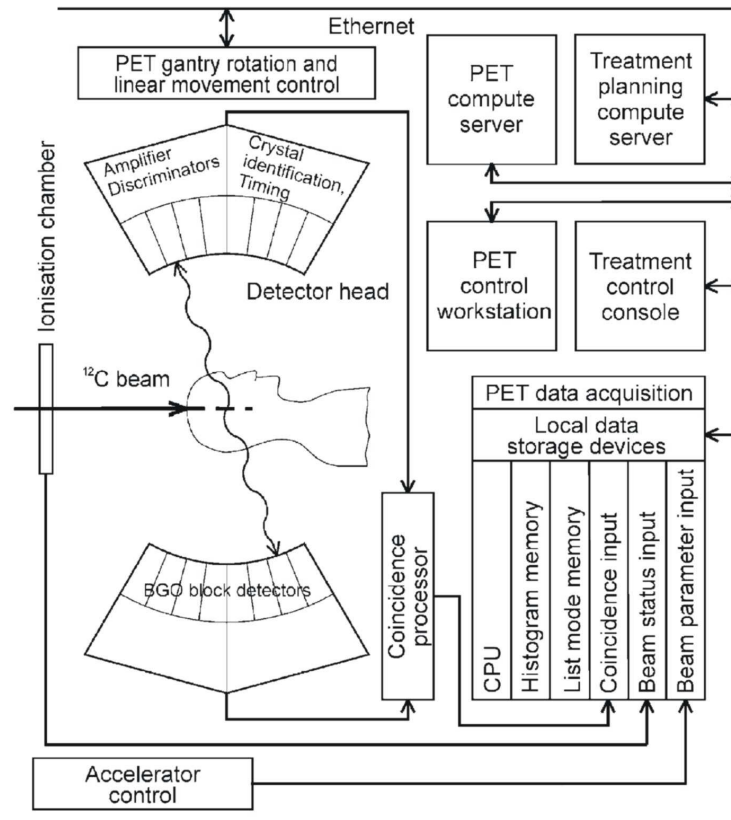
**Figure 1.9:** *Data processing scheme for in-beam PET [Eng04]. The two heads work in coincidence. The coincidence events are stored locally together with the beam status. The data can be read out via a network connection.*

of the beam and secondary particles, fragmentation reactions with the tissue, transport of the annihilation photons and the detection process. It needs as input: the CT for density and stoichiometric composition, the treatment plan for beam properties like energy, position and intensity, and the time course of the irradiation. Because the time course is different at each fraction it is neither possible to perform the simulations prior to the irradiation nor to use the same simulation for all fractions. Therefore, the simulations have to be done after each fraction. A scheme of the clinical routine is shown in figure 1.10.

The output of the PETSIM code is in the same binary data format (i.e. list mode data) than the data from the PET scanner to enable the reconstruction by the same code. Only the first treated field (i.e. treatment position) of each fraction can be monitored because for the following fields the already present $\beta^+$-activity compromises the activity. To enable also the monitoring of the remaining fields, the field sequence is swapped at the next treatment day. One important quantity to monitor is distal part of each field. This is the part which arises from the highest energies. Because of metabolic processes the activity is blurred and reduced
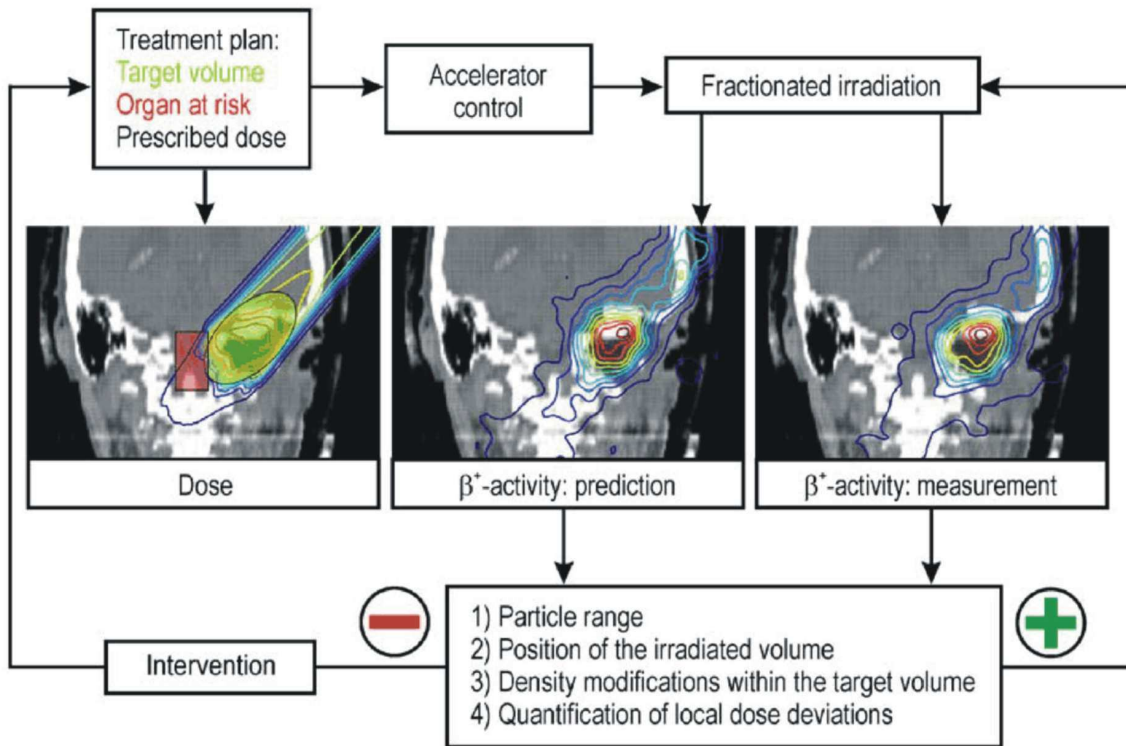
**Figure 1.10:** *Scheme of the clinical routine. The left picture shows the treatment plan with the tumor (green) close to a organ of risk (red) and the prescribed dose (lines). From the treatment plan and the accelerator control a prediction of the $\beta^+$-activity is made (picture in the middle) which is compared with the measured $\beta^+$-activity (right). In case the pictures don't match a the reason is investigated and an intervention, if necessary, is done. [Eng04]*

rapidly (washout) [Fie07, Tom03, Miz03]. This effect is time dependent and stronger for the part of the field which is treated at first. Because the distal part of the beam is an important region to monitor the beams with the highest energies are delivered at last.

Finally fused images of the simulation and the measurement are compared visually to draw a conclusion if the beam delivery was like expected.

**Dose quantification**

Because the $\beta^+$-activity arises from nuclear reactions and the dose from electromagnetic interactions the activity distribution does not match the dose distribution. Dose and $\beta^+$-activity arise from different physical processes therefore, by a comparison between measured and simulated $\beta^+$-activity problems in dose delivery can be only revealed but the difference in delivered dose cannot be quantified.

Mathematically one can describe the calculation of the $\beta^+$-activity from the dose as the matrix multiplication

$$\mathbf{A} = \mathbf{T} \times \mathbf{D} \tag{1.8}$$

where $\mathbf{A}$ and $\mathbf{D}$ are 1-dimensional vectors representing activity and dose and $\mathbf{T}$ is a 2-dimensional transition matrix. To enable dose quantification on basis of $\beta^+$-activity distributions equation 1.8 has to be inverted to be solved (this is often referred to as solving the *inverse problem*). Unfortunately this is not possible because (i) of low counting statistics and the limited angle of the PET scanner, (ii) the not quantitative reconstruction by the MLEM algorithm and (iii) wash out of the activity due to the metabolic processes [Par04].

To still enable dose quantification an interactive approach was developed [Par04]. In case the simulated activity differs from the measured one an assumption about the origin of the problem has to be made, i.e. missalignment or anatomical modifications due to the filling of nasal and paranasal cavities with mucus or tissue modifications after surgery. Then a dedicated computer program is used to modify the CT according to the assumed error by rotations or translations to correct for misalignments or by modifying the local density to correct for anatomical modifications. Then the activity is recalculated on base of the modified CT. If the recalculated activity does not support the modifications made, further modifications on the CT are done and the activity is calculated again. Once a modification leading to a matching activity distribution is found the dose is recalculated by the treatment planning software using the modified CT. The difference between the dose planned on the original CT and on the modified CT gives the difference in delivered dose. If the interactive approach supports the assumption of anatomical modifications a new CT is done and a new treatment plan is created on base of the new CT.

Based on the experience gained after monitoring the treatment of 180 patients at GSI with $^{12}$C ions the following conclusions of the benefit of in-beam PET were drawn [Eng04]: this method can reveal deviations in the maximum particle range due to *(i)* inaccuracies of the physical beam model of the treatment planning, *(ii)* positioning errors and *(iii)* modifications in the patients tissue compared to the CT used for treatment planning *(iv)* setup errors. By tuning the beam models used for treatment planning problem *(i)* can be solved. The problems *(ii)* to *(iv)* demand a permanent monitoring of all fractions. If problems due to *(ii)* to *(iv)* are discovered dose quantification can be done by using the interactive procedure mentioned before.

## 1.3 FLUKA

FLUKA [Fas05, Fas03] is a general purpose particle and heavy ion transport and interaction code which is developed and maintained in the framework of an agreement between the European Laboratory for Particle Physics (CERN) and the Italian National Institute for Nuclear Physics (INFN). It is capable of handling the transport and interactions of hadrons, heavy ions and electromagnetic particles from a few keV (or from thermal energies for neutrons) up to cosmic ray energies in whichever solid, gas or liquid material. FLUKA is used for a vast variety of applications like proton and electron accelerator shielding applications, target design, calorimetry, activation, dosimetry, detector design, Accelerator Driven Systems, space radiation and cosmic ray showers, neutrino physics and radiotherapy. Particles can be transported in arbitrary complex geometries, which can also include magnetic fields. For therapeutic application a module which handles voxel geometries like CT scans, is available. FLUKA is constantly updated and extended. A description of recent developments can be found in [Bal07].

### Electrons and photons

The transport and and interactions of electrons and photons is handled in FLUKA by EMF (ElectroMagneticFluka) including scattering and photon nuclear interactions. Until version 2003 included a preprocessor was necessary to enable EMF, now the initialization is done automatically.

### Neutrons

The transport of neutrons with energies lower than 19.6 MeV is performed in FLUKA by a multigroup algorithm with cross sections obtained from evaluated data files (ENDFB-VI, JEFF 2.2, JENDL 3.2) with standard processing tools. For a few isotopes the transport can be done by using continuous cross-sections.

### Transport of charged particles

The transport of charged particles is performed through an original Multiple Coulomb scattering algorithm, supplemented by an optional single scattering algorithm [Fer92]. The treatment of ionization energy loss is based on a statistical approach alternative to the standard Landau and Vavilov ones that provides a very good reproduction of average ionization and of fluctuations [Fas97]. Multiple scattering with inclusion of nuclear form factors is applied also to heavy ion transport. Up-to-date effective charge parameterizations are employed and straggling of ion energy loss is described in "normal" first Born approximation with inclusion of charge exchange effects.

## Hadronic interactions

A description of hadronic interactions in FLUKA and their most recent developments can be found in [Fer98, Col00, Bat06]. Hadron-nucleon inelastic collisions are described up to a few GeV by resonance production and decay. At higher energies up to several tens of TeV the Dual Parton Model (DPM) is used.

Hadron-nucleus interactions from threshold up to 5 GeV are described by PEANUT (PreEquilibrium-Approch-to-NuclearThermalization)[Fer94, Fas95, Fer98, Bat06]. It describes interactions by an IntraNuclearCascade (INC) model, which is a cascade of two-body interactions, concerning the projectile and the reaction products. The INC goes on in PEANUT until all nucleons are below a smooth threshold around 50 MeV and all particles but nucleons have been emitted or absorbed. Then pre-equilibrium particle emission is done followed by evaporation, fragmentation or fission.

## Nucleus-nucleus interactions

Above 5 GeV/n nucleus-nucleus interactions are treated with an interface to DPMJET-III [Rös01], at lower energies with an interface to a modified version of rQMD-2.4 [Sor89, And04]. For very low energies, i.e. energies down to the Coulomb barrier, a new event generator based on the Boltzmann Master Equation theory (BME) [Cer06] was recently implemented.

## BME

A generalization of the Boltzmann master equation theory in order to evaluate the angular distributions of the ejectiles emitted during the nucleon-nucleon interaction cascade which brings about the thermalization of the composite nucleus formed in the fusion of two heavy ions is discussed in [Cav98]. A computer code that solves the equations is described in [Cav01]. However, the calculations this code performes are too time consuming to be calculated run-time in a Monte Carlo code like FLUKA. To overcome this limitation, pre-equilibrium emission for representative sets of ion pairs at different energies were evaluated and parameterized to create a data base. The BME event generator implemented in FLUKA does a proper interpolation of these parameters and the pre-equilibrium emission can be simulated. BME currently covers [Cer07]:

- Complete fusion with a probability which depends on the energy and projectile-target combination under consideration. Ejectiles up to alpha particles are then emitted with multiplicities, spectra and angular distributions computed according to the BME formalism.

- Three body reactions, where the overlap region between the two nuclei, computed according to geometrical considerations combined with an impact parameter cross section profile and two remnants give rise to three excited objects.

- For large impact parameters no three body reactions is passing into inelastic excitation, where the nuclei are simply excited.

After the particles are created by BME, they are returned to FLUKA and are subsequently de-excited by evaporation, fission or fragmentation. The present implementation of BME covers light ion interactions on material of biological interest from the Coulomb barrier up to 100 MeV/n. The extension to heavier projectiles and targets is in progress and the modell will eventually cover all combinations up to 100 $A$MeV. The model was recently implemented and is still undergoing benchmarks and tests aimed to fine tune its performances.

### Biasing

A possible way of running a Monte Carlo code it to treat all physical processes as closely as possible to their natural way of occurrence. This is called a fully analog run, FLUKA can run in fully analog mode. However, for many applications, for example for deep penetration calculations or rare interactions, this is not very efficient. Instead variance reduction techniques converging to the correct expectation values but reducing the variance or the CPU time or both by sampling from biased contributions can be used. Several variance reduction techniques (biasing) are available in FLUKA. The central concept of the biasing is to attach a numerical value of its importance, a so called "weight" to compensate for the biasing. This weight has to be taken into account when the simulation results are evaluated.

In the following some biasing options of FLUKA are explained.

- *Multiplicity Reduction* was introduced in FLUKA for the first time and was later adopted by other codes. It is used in order to reduce the computing time in hadron cascades of several hundred GeV. Many secondaries in such interactions are of the same kind and have similar angular and energy distributions. The user can decide to follow only a fraction of them to save CPU time.

- *Leading Particle Biasing* is used on electromagnetic showers. Only one of the two secondary particles which are present in the final state of most electromagnetic interactions is sampled. The particle with the higher energy is sampled with higher probability.

- *Inelastic interaction length biasing:* The probability of hadronic interactions can be artificially increased by *LAM-BIAS*. This is especially useful to get a higher probability of hadron interactions in thin targets or material with low density.

- *Decay direction biasing* It can also be used to bias the direction of the secondaries from a decay.

- *Importance biasing* consists in assigning an importance value to each geometry region. The number of particles moving from one region to another will increase or decrease according to the ratio of importances and the statistical weight of the particles will be modified inversely so that the total weight remains unchanged.

- *Weight windows* is biasing technique based on the particles weight. An upper and lower limit for the particle weight, possibly tuned per particle type and particle energy, in each geometrical region is set. Splitting is applied so that the weight of all particles will have a value between the limits.

- *Decay length biasing* can be used to increase the production of decay products e.g. muons or neutrinos.

### Defaults

Fluka has defaults for specific problems to support the user in the choice of the physics options to use. Defaults exist for calorimetry, electromagnetic cascades, low energies neutron experiments, shielding calculations hadrontherapy and for many other kind of problems. For the simulations presented in this work only the hadron therapy default was used. The most important features in the hadron therapy option are: EMF on, low energy neutron transport, particle transport threshold set to 100 keV and delta ray production is switched on with a threshold of 100 keV.

### Scoring

Standard scoring is done in *binnings* which are uniform spatial meshes which are independent from the geometry. In such binnings energy deposition, star density (inelastic hadron reactions) or particle fluence distributions can be scored. Fluka also offers boundary crossing estimators (USRBDX), track length estimators (USRTRK) and estimators to score double-differential quantities (USRYIELD). Event by event scoring is also possible.

### Tools

To work with Fluka , the user has to write an input file and has, for special problems, to write some FORTRAN routines (user routines). A graphical user interface is not part of the standard Fluka distribution.

Recently a front-end interface called *flair* (FLUKA Advanced Interface) aimed to make the creation of input file easier, was developed. It offers features like debugging, compiling, running and monitoring of the status during a run. flair is however, not part of the Fluka distribution but can be separately downloaded from the *flair* website *http://www.fluka.org/flair/*.

## 1.4 Aim and outline of this thesis

The aim of this thesis is to investigate the feasibility of FLUKA to predict the $\beta^+$-activity induced by $^{12}$C and $^{16}$O beams, necessary for in-beam PET. Because in-beam PET experiments with $^{16}$O have never been performed before no data was available. Therefore, experiments with $^{16}$O beams on homogeneous targets of water, polymethyl methacrylate (PMMA) and graphite were performed and the created $\beta^+$-activity was measured by means of in-beam PET. Additionally experiments with $^{12}$C beams similar to the $^{16}$O beam experiments were performed for comparison. The set up and analysis of the experiments is described in chapter 2.

On basis of the experimental data FLUKA and its implemented nuclear reaction modells where benchmarked. Of special interest was the performance of the recently added event generator BME which handels nucleus-nucleus interactions at low energies. Effort was made to improve the performance by means of reducing the computing time by various variance reduction methods. The simulations and comparisons with the experimental data are described in 3.

The conclusions and a outlook are given in chapter 4.

# Chapter 2

# In-beam PET Experiments

## Motivation

There are two motivations for the here presented experimental investigations. The main one is the future use of in-beam PET monitoring in a therapy with $^{16}$O beams but as spin-off this data can also be used for benchmarking FLUKA.

The in-beam PET method was used so far only for monitoring the therapy with $^{12}$C beams in the experimental facility at GSI. In the future therapy clinic HIT for the first years $^{12}$C and proton beams will be available and later $^{3}$He and $^{16}$O beams will follow. It is planned to monitor the treatment of all these beams by means of in-beam PET [Hab04].

A first step towards such monitoring is to investigate qualitatively and quantitatively the $\beta^+$-activity distributions of these beams in homogeneous targets. Carbon ions have favorable properties for in-beam PET monitoring. The $\beta^+$-activity they produce is dominated by a peak of $^{11}$C projectiles in vicinity of the dose peak. Target fragments like $^{15}$O contribute homogeneously. Ions beams with an atomic number lower than 5 cannot produce $\beta^+$-active projectile fragments and the produced $\beta^+$-activity is due to target fragmentation. Such distributions have no pronounced peak, however monitoring the treatment of such beams by means of in-beam PET is still possible [Par02].

The activity produced by $^{16}$O beams is similarly distributed as the one induced by $^{12}$C beams: a pronounced peak due to projectile fragmentation close to the position of the Bragg Peak superimposed onto a background of target fragments. The combination of an $^{16}$O beam on a target which contains significant amounts of carbon and oxygen is a special case because during and short time after irradiation the activity is dominated by $^{15}$O, but some minutes later most of the $^{15}$O is decayed and the activity is dominated by $^{11}$C. That leads to the phenomenon that the shape as well as the position of the activity peak changes with time. The explanation for this phenomenon is the following: $^{15}$O nuclei, produced as projectile fragments, come to rest at a certain position. $^{11}$C nuclei which can be produced also as projectile fragments have a different $A/Z^2$ ratio than $^{15}$O and travel therefore a little bit further, therefore, the shape

and position of the activity distribution looks different at different times. For $^{12}$C beams the peak is dominated by $^{11}$C and does therefore not change its shape or position with the time. The peak to plateau ratio however does change.

Besides the discussed changes of the peak position and shape, also the peak to plateau ratio of the $\beta^+$-activity induced by $^{16}$O beams changes, as already mentioned for $^{12}$Cions.

In addition to the $^{16}$O experiments also $^{12}$C irradiations were performed. The purpose of these experiments was to provide additional data for the benchmarking of FLUKA. Already several $^{12}$C in-beam PET experiments with homogeneous targets especially on PMMA were performed, but predominantly with additional material i.e. ripple filter [Web99] in the beam. To model the ripple filter in FLUKA is possible and was already done, but it complicates a benchmarking. In fact, once deviations between the Monte Carlo simulation and the experiment are discovered, it is difficult to distinguish between effects from the modeling of the geometry and effects of the internal physical models.

## 2.1 Analytical methods

The mathematical methods used for analyzing the experiments are the same already used for evaluating in-beam PET experiments for irradiation of homogeneous phantoms with proton, $^{12}$C and $^{3}$He beams described in [Par02] and [Fie06]. This methods are explained in sections 2.1.1 to 2.1.3. Using the same methods in this work enables a reliable comparison with the previous ones.

### 2.1.1 Relative isotope production rates

Besides the spatial distribution of the $\beta^+$-activity the total amount of $\beta^+$-activity produced per spill is an interesting quantity. Fitting the count rate detected after irradiation can lead to an estimation of the relative total produced $\beta^+$-activity and the contribution of the different nuclides. The term "relative" expresses the fact that a production rate found this way is depending on the detection efficiency of the PET scanner and on the attenuation of the annihilation photons. The latter depends on the material and shape of the target and on all other material in the field of view (i.e. the air and patient couch which holds the target). Production rates which are corrected for attenuation and detection efficiency are called "absolute".

Similar in-beam PET experiments for $^{12}$C and proton beams were done and described in [Par02, Par05] The same mathematical basis for calculating the relative and absolute amount of produced $\beta^+$-emitters is used for this work is are summarized in the following.
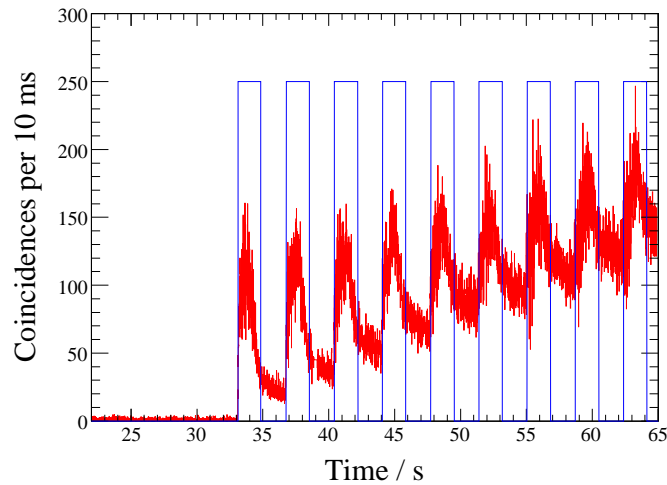
**Figure 2.1:** *Example of experimental coincidence rates at the beginning of an irradiation. The coincidence rate is displayed in red, the first spill starts at about 32 seconds and ends at about 35 seconds. The blue line shows the status of of the beam, its height is chosen for visibility and has no special meaning.*

### Relative isotope abundance

To calculate the relative amount of $\beta^+$-emitters present after the last spill a fit of the decay curve has to be done. The function for fitting is a superposition of the activity curves of the individual isotopes:

$$A(t) = \sum_l \lambda_l N_l e^{-\lambda_l(t-t_0)} \tag{2.1}$$

where $\lambda_l$ is the decay constant of the nucleus $l$, $N_l$ the relative amount of nuclei of type $l$ present at the end of irradiation $t_0$. For each projectile–target combination different nuclei have to be chosen. For instance for an irradiation of graphite with $^{12}$C only $^{11}$C and $^{10}$C will contribute to the $\beta^+$-activity but no $^{15}$O. To control if the choice of isotopes is consistent with the experiment an overplot of the decay curve with equation (2.1) can be done. If the curves do not match the assumption of contributing isotopes is wrong.
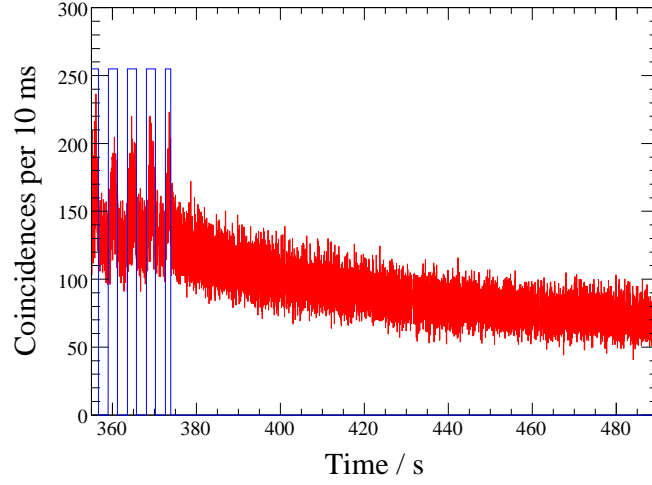
**Figure 2.2:** *As figure 2.1 but at the end of the irradiation. The relative isotope abundance is obtained by fitting the decay curve starting after the last spill.*

### Relative production rates, recursive approach

Once the relative amounts $N_l$ are calculated one can calculate the production rates during the spills. Assuming that the duration of each spill and the duration of the pauses between the spills are constant and additionally the intensity of the beam remains constant during the whole irradiation, it is possible to calculate average relative isotope production rates. Let $P_l$ be the production rate for the nuclei of type $l$, then the number of nuclei of type $l$, present after the first spill $K_{l,1}$ is calculated by:

$$K_{l,1} = \frac{P_l}{\lambda_l}(1 - e^{-\lambda_l t_s}) \tag{2.2}$$

where $t_s$ is the average spill duration in seconds. The number of nuclei of type l present after the j-th spill $K_{l,j}$ follows by the recursion:

$$K_{l,j} = K_{l,j-1}e^{-\lambda_l(t_p+t_s)} + \frac{P_l}{\lambda_l}(1 - e^{-\lambda_l t_s}) \tag{2.3}$$

where $t_p$ is the average duration of the pause between two spills. Knowing the abundance of the isotopes of interest by solving the fit 2.1 and setting it equal to $K_{l,\mathcal{T}}$ where $\mathcal{T}$ indicates the index of the last spill then from equations (2.3) and (2.2):

$$P_l = \frac{\lambda_l K_{l,\tau}}{(1 - e^{-\lambda_l t_s})\sum_{i=1}^{\mathcal{T}} e^{-\lambda_l(i-1)(t_p+t_s)}} \tag{2.4}$$

where $t_p$ is the average duration of the pause between two spills.

**Individual relative production rates**
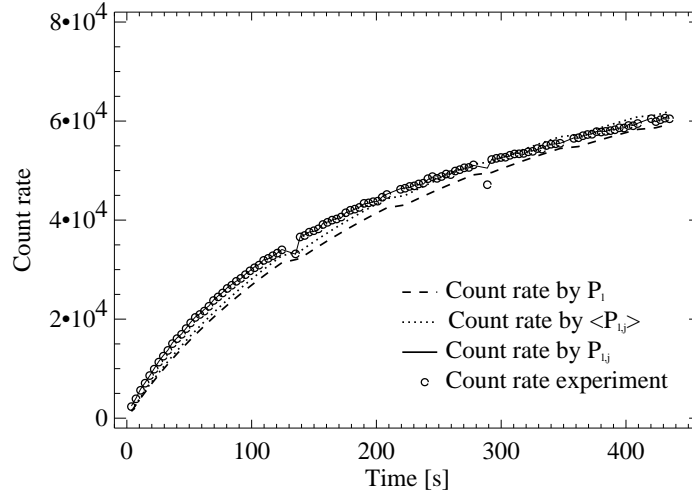


**Figure 2.3:** *Count rates for the irradiation of PMMA with an 250 AMeV $^{16}O$ beam obtained by using different methods for calculating the production rates.*

It is not always possible to assume that the spill duration $t_s$ as well as the pauses between two spills $t_p$ are constant over the whole time course of the irradiation. A frequent problem is short interruptions of the irradiation due to accelerator problems. Because this happens quite often and also because of limited total time for all experiments, it is in general not possible to repeat the irradiation with an other target. Therefore, it is necessary to use also a further calculation method which determines the individual production rates $P_{l,j}$ for each of the $j$ spills. This approach uses the real spill and pause durations as well as the total activity $A_j$ present after each spill. The measured activity after each spill $A_j$ depends on the production from all previous spills as well as on the individual duration of the spills and the pauses. It can be calculated by:

$$\mathcal{A}_j = A_j - \sum_l \sum_{i=1}^{j-1} P_{l,i}(1 - e^{-\lambda_l t_{s,i}})exp^{-\lambda_l \sum_{m=1}^{j-i}(t_{s,m+1}+t_{p,m+i-1})} \tag{2.5}$$

where the $t_{s,i}$ are the individual length of the spills. The individual production rates $P_{l,j}$ can be calculated from $\mathcal{A}_j$ by:

$$P_{l,j} = \frac{\mathcal{A}_j f_l}{1 - e^{-\lambda_l t_{s,j}}} \tag{2.6}$$

where $f_l$ is the relative activity contribution of the isotopes of type $l$. It can be calculated from the production rates $P_l$ calculated by equation (2.4):

$$f_l = \frac{\lambda_l P_l}{\sum_k \lambda_k P_k} \tag{2.7}$$

Because $\beta^+$-active isotopes with a short half-life compared to the pauses between the spills can be fit by equation (2.1) only with huge errors, they cannot be taken further into account in the equations (2.2)–(2.7). This limitation results in a slightly overestimation of the individual production rates by equation (2.6) because all experimentally found activity is addressed only to the $l$ isotopes used for fitting the activity present after the irradiation. But still equation (2.6) gives better results than the recursive calculation (2.4) because for most of the experiments interrupts of the beam delivery occur and therefore, the assumptions of constant spill and pause duration is not true. It is important to notice that equation (2.6) depends on equation (2.4). Therefore, the differences in spill and pause length must not be too big, otherwise equation (2.6) will lead to large errors.

To cross check if recursive and individual method give reasonable production rates the count rate during the pauses $cps_j$ can be calculated by:

$$cps_j = \sum_l \left\{ \sum_{i=1}^{j} \left[ \frac{L_{l,i}(1 - e^{-\lambda_l t_{s,i}})}{\lambda_l} e^{-\lambda_l \sum_{m=1}^{j-i}(t_{s,m+1}+t_{p,m+i-1})} \right] \frac{1 - e^{-\lambda_l t_{p,j}}}{t_{p,j}} \right\} \qquad (2.8)$$

where for $L_{i,j}$ the individual $P_{i,j}$ from equation (2.6) or $P_l$ from (2.4) for all $j$ or an average production rate $\langle P_{i,j} \rangle$ can be used.

## 2.1.2 Absolute production rates

To calculate the absolute production rates the relative ones calculated by (2.4), (2.6) or (2.8) have to be corrected for the attenuation of the annihilation photons and for the spatial varying detection efficiency. To enable also a comparison by activity introduced by different projectiles their different spatial activity distributions have to be taken into account. Therefore, a *local* correction factor $c(\mathbf{r})$ has to be calculated by:

$$c(\mathbf{r}) = \frac{A_u(\mathbf{r})}{A(\mathbf{r})} \qquad (2.9)$$

where $A_u(\mathbf{r})$ is the activity by a backprojection without correction and $A(\mathbf{r})$ is the activity obtained by a backprojection with the two corrections. The total correction factor $\mathcal{C}$ is an average by means of a weighted integral over the corrected spatial activity:

$$\mathcal{C} = \int d\mathbf{r} \; c(\mathbf{r}) \; p(\mathbf{r}) \qquad with \quad p(\mathbf{r}) = \frac{A(\mathbf{r})}{\int d\mathbf{r} \; A(\mathbf{r})} \qquad (2.10)$$

$$\mathcal{C} = \frac{\int d\mathbf{r} A_u(\mathbf{r})}{\int d\mathbf{r} A(\mathbf{r})} = \frac{\sum_i A_{ui}}{\sum_i A_i} \qquad (2.11)$$

In the last equation the integral was substituted by a sum over the i voxels of the activities. To obtain absolute production rates the relative production rates have to be divided by $\mathcal{C}$.
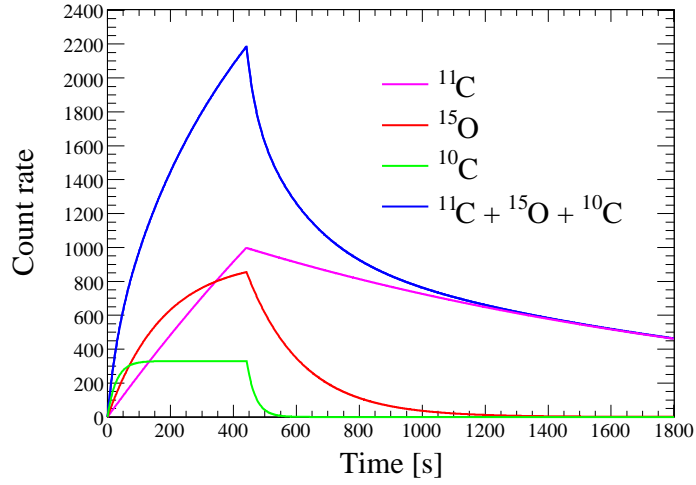
**Figure 2.4:** *Example for the count rates of the individual nuclides. The blue line shows the total count rate, $^{11}C$ is shown in magenta, $^{15}O$ is shown in red and $^{10}C$ in green. During the irradiation the count rate increases. The count rate of $^{10}C$ reaches saturation. After irradiation end (at about 442 seconds) the contribution of $^{10}C$ drops very fast. About ten minutes after irradiation end only $^{11}C$ contributes to the count rate.*

### 2.1.3 Individual activity

$^{11}$C and $^{15}$O are the nuclei of most importance in in-beam PET investigations. Due to their different half-lives their contribution to the total activity changes over time. The amount $\mathcal{D}_{l,j}$ of $\beta^+$-active nuclei of type $l$ decaying in the j-th pause can be calculated by:

$$\mathcal{D}_{l,j} = \frac{P_l(1 - e^{-\lambda_l t_s})}{\lambda_l} \left[ \sum_{i=1}^{j} e^{-\lambda_l(i-1)(t_s+t_p)} \right] (1 - e^{-\lambda_l t_{p,j}}) \tag{2.12}$$

To obtain the amount of nuclei of type $l$ decaying in a specific time interval after irradiation end equation:

$$\mathcal{D}_{l,j} = N_l e^{-\lambda_l(t-\bar{t})}(1 - e^{-\lambda\triangle t}) \tag{2.13}$$

has to be used. $N_l$ is the amount of nuclei of type $l$ at the end of irradiation.

An example for the individual count rates is given in figure 2.4. The duration of the irradiation is about 442 seconds, the total count rate is given by the blue line, $^{11}$C is shown in magenta, $^{15}$O is shown in red and $^{10}$C in green. The build up depends on the half-lives of the nuclides. It can be seen that the count rate of $^{10}$C reaches saturation after about 100 seconds. At the end of the irradiation the count rate of $^{15}$O starts to flatten but has not reached saturation

yet. The irradiation time is too short that the count rate of $^{11}$C can reach saturation.

After irradiation end the contributions of $^{10}$C and $^{15}$O drop fast. About ten minutes after irradiation end the count rate is dominated by $^{11}$C, the other nuclides do not contribute significantly any longer.

## 2.2   Experimental Methods and Setup

All experiments were performed at GSI in Cave M, the medical cave, in February 2007. The decay time (i.e., the additional measuring time after irradiation end) was chosen to be 30 minutes. This is enough to make backprojections at time windows where isotopes with short half-life, especially $^{15}$O do not contribute significantly any more. It is also long enough to get good fits for the decay curves with equation (2.1) for calculating the production rates.

To measure the intensity only the ionization chamber used in therapy was available. This device gives the intensity of each spill an the total particles integrated over all spills. Since it is to complicated to write down 120 intensity values per experiment, it was checked if the intensity is stable and only the total intensity was written down. The total intensity is displayed in so called monitor units (MU) which were converted to the number of particles by taking into account the dependency on the energy of the beam and the dependency on the ion species. Intensity fluctuations, if there are any, cannot be detected by this integrated measurement.

It is known that by the backprojection the activity is shifted slightly towards the center of the field of view. Therefore, the position of the activity peak can be determined with the highest accuracy when it is in the center of the FOV. Hence, the targets were placed in such way that the expected activity peak is in the center of the FOV.

Fluka simulations were performed to determine the exact penetration depth and it was assumed that the peak of the $\beta^+$-activity is just a few millimeter before the Bragg peak. The positioning of the targets was done by using the laser system as reference. It marks the ISO center which coincides with the center of the field of view of the PET camera in measuring position.

The activity produced was high, especially for the irradiations with high energies. This is on the one hand an advantage for backprojections especially for those done after the irradiation but on the other hand the data buffers is filled faster and has to be flushed more often.

A slight horizontal beam position instability was discovered. In therapy this is compensated by the raster scanning system which could not be used for the experimental beams of $^{16}$O. However it was found that the moving has no effect on the activity distributions because those are always evaluated by summing over regions of a few millimeters.

No ripple filter was used to enable simpler simulations, because every material in the beam must be modeled as precise as possible to get the right positions and the right fragmentation reactions.

### 2.2.1   Targets

The experiments were done with the aim to produce data for in-beam PET measurements in a therapeutic situation. Therefore, the choice of targets reflects that issue. The target material

**Table 2.1:** *List of used phantoms. Several identical PMMA and gelatine phantoms were used and are not listed separately.*

| ID | Material | Size [cm] | $\rho$ [g/cm$^3$] |
|---|---|---|---|
| MAT1 | PMMA | $9 \times 9 \times 20$ | 1.18 |
| MAT2 | graphite | $10.3 \times 10.3 \times 30$ | 1.71 |
| MAT3 | graphite | $9 \times 9 \times 15$ | 1.795 |
| MAT4 | water | $9 \times 9 \times 20$ | 1.0 |
| MAT5 | water | $9 \times 9 \times 30$ | 1.0 |

should have similar properties as human tissue, not only in terms of stoichiometric composition but also in terms of density. Furthermore, as the second purpose of the experiments is also to provide data for further simulations the composition of the targets has to be kept as simple as possible.

The following three materials were chosen:

- PMMA, polymethyl methacrylate, also known by the trade name Plexiglas

- graphite

- water, with gelatine added

PMMA is a widely used material for phantoms in medicine because its stoichiometric composition $C_5O_2H_8$ and its density 1.18 g/cm$^3$ is similar to the human body. Furthermore it is easy to machine and handle. Several PMMA blocks with the size of $9 \times 9 \times 20$ cm$^3$ were used.

Graphite was chosen because of its simple composition. While for PMMA the activity contribution is influenced by the different elements it is made of, graphite enables to investigate deeper the contribution of the carbon in the target. Regarding the simulation the main interesting case is the $^{12}$C irradiation. Because only the reaction between two $^{12}$C nuclei is possible, it is the perfect material to investigate the internal models of FLUKA.

The third material used was water with a small amount of gelatine added. The choice of water as target material is obvious because it is the most abundant substance in the human body. Unfortunately liquids cannot be used for in-beam PET experiments because of convection. Over the about 40 minutes of measurement the activity would diffuse over the whole volume making it impossible to determine spatial activity distributions. One way to suppress convection would be to use ice instead but homogeneous ice without dissolved air is very difficult to produce. Instead gelatine was used like in other in-beam PET experiments described in [Fie06]. Agar-Agar (Agartine by RUF) was used which it is made by red algae. It has the advantage that it does not contain as much sulphur and nitrogen like customary gelatine that is made by animals collagen.

Two phantom sizes were used: $9 \times 9 \times 20$ cm$^3$ and $9 \times 9 \times 30$ cm$^3$ for which 50 g and 70 g of Agartine were added, respectively. The stoichiometric composition of these target was found to be $H_{66.6}O_{33.1}C_{0.7}$. It is not expected that the additional carbon has any significant effect on the beam spread or the range of the beam because the amount of gelatine added is is very small. Also the amount of additionally created $\beta^+$-active carbon isotopes is expected to be small. Therefore, in the following these targets will be called water targets.

After putting the gelatine targets out of the mould they tend to deform a little in the first minutes. Therefore, it was waited at least half an hour before irradiating them. Once out of the mould the gelatine looses a little water but no change in shape could be discovered.

A list of the used phantoms is given in table 2.1. For the 350 $A$MeV irradiation with $^{16}$O the length of the PMMA phantoms is not sufficient to create also the activity tail therefore, two phantoms placed one after the other were used.

## 2.2.2   Implementation of the analysis

After the end of the experiments the data files where transferred from GSI to the computing system of Forschungszentrum Dresden-Rossendorf. There software for analyanalyzinglist mode data is available. An implementation of the mathematical models described in section 2.1.1 written in IDL (Interactive Data Language, software for data analysis) by Katia Parodi was also available. However, not all these routines could be used because the visualization over the internet was too slow therefore, the analysis was performed on the EET cluster at CERN where also the FLUKA simulations were performed. Because IDL is not available at CERN the analytical methods were implemented in ROOT (a data analysis framework, written in C++). The new implementation was cross checked with an old data set. The results obtained with the ROOT and the IDL implementation were found in good agreement.

## 2.2.3   Irradiation parameters

**Table 2.2:** *Parameters of the irradiation with $^{12}C$.*

| ID | Target | E [$A$MeV] | R [cm] | Number of spills | Intensity per spill | duration spill [s] | duration pause [s] | Number of events |
|---|---|---|---|---|---|---|---|---|
| C12W260 | water | 260.0 | 13.5 | 120 | $1.50 \cdot 10^8$ | 1.87 | 1.81 | $1.18 \cdot 10^7$ |
| C12P260 | PMMA | 260.0 | 11.7 | 120 | $1.53 \cdot 10^8$ | 1.78 | 1.90 | $7.83 \cdot 10^6$ |
| C12G260 | graphite | 260.0 | 8.8 | 117 | $1.63 \cdot 10^8$ | 1.71 | 2.12 | $5.76 \cdot 10^6$ |

Experiments with $^{16}$O and $^{12}$C beams of various energies on PMMA, water and graphite targets where performed. For the $^{12}$C beam only one energy, 260 $A$MeV, was used. For the $^{16}$O

beam the energies 200, 250, 300 and 350 $A$MeV were used. To make the discussion easier for each experiment an alphanumerical identifier composed by projectile, target and energy was chosen cf. tables 2.2 and 2.3. For instance O16P350 refers to the experiment of an $^{16}$O beam with 350 $A$MeV on PMMA. The characters identifying the targets are P for PMMA, G for graphite and W for water.

120 spills were delivered for each experiment. The length of the spills and the pauses between two spills depends on the accelerator and could not be kept constant for all experiments.

Three types of problems which compromises the analysis occurred during data taking. The first is an interruption of the irradiation due to accelerator problems. This leaded to pauses in the order of 10 seconds before the irradiation started again. This problem cannot be avoided. It affects the calculation of the production rats by the recursive approach because the the assumption that the breaks between the spills are always of the same length is not valid anymore. However, only in one experiment two longer interruptions happend. In the other experiments only one or no interruption took place.

In the experiment O16G300 interruptions happend after the 116-th spill for 12.4 seconds and in the experiment C12G260 after the 114-th for 9.4 seconds and after the 116-th spill for 5.7 seconds. Both experiments are with graphite phantoms. During the interruptions a non negligible part of $^{10}$C decays and cannot be build up to saturation in the remaining 4 spills. The recursively calculated production rates of $^{10}$C can therefore, be underestimated. The individual production rates take the interrupt of the irradiation into account but they depend on the recursively calculated rates cf. 2.7 and the production of $^{10}$C can therefore, be underestimated also by the calculation with the individual time structure. The recursively calculated rates on the other hand tend to overestimate the production in general because annihilations coming from isotopes with a short half-life are addressed to those with a longer half-life (cf. p. 37). No solution was found to correct the production rates, therefore, bigger errors were given.

The second problem is that in the count rates sometimes spikes, i.e. count rates which are significantly higher for a short time than the count rates before and afterwards were discovered. The origin for that spikes could be that for short time the time labeling is corrupted and over some tens of milliseconds events getting the same time labels. To not compromise the fits of the decay after irradiation end or during the spill breaks those events were set to an average of the events before and after. It is assumed the the error introduced by this correction method is negligible because the correction effects only some milliseconds.

The third problem is a full data buffer. The data is saved in list mode. Each data word has 4 Bytes. Every 10 milliseconds a time stamp is inserted which has the same size than a data word but is marked by setting of a special bit. The list mode memory is 32 MB divided into two buffers of 16 MB each. The buffers work in alternating buffer mode, i.e if one buffer is full it is flushed to the hard drive and the other buffer is used to record the arriving events. This happens every 4 194 304 events. Because the generating of the time stamps has lower priority than the data transfer from the buffer to the hard drive, for several seconds no time

stamps are created and the count rate is averaged.

This happend a few times during irradiation and a few times after irradiation. In the irradiation with $^{16}$O and in the irradiations with high energies more activity is produced and therefore, more regions of flat count rates due to flushing the data buffer occurred. The worst case was the irradiation of water with $^{16}$O (experiment O16W350) where such perturbations occurred 12 times during the irradiation and 11 times after the irradiation.

The analysis of the decay curves could still be done without problems because in the 30 minutes of decay up to 80 seconds are disturbed which does not compromise the fitting. Therefore, the recursive calculated isotope production rates which depends only on the fit of the decay after irradiation end could be done. It would be only problematic if the buffer would be flushed just after the end of the irradiation because there the nuclides with short half-lifesliefsribute most and fitting of nuclei with short half-lifesliefs $^{10}$C would be possible only with big errors for the nuclides with short half-lives. That problem did not occur in the here presented experiments.

Fitting the activity during the irradiation needed more effort. The only solution found was to not do any fit during the flushing of the buffer. That means that all activity produced in the spills during the flushing is addressed to the following spill and the number of spills is reduced. This leads to fluctuations in the production rates for the spills after a buffer flushing. However, by averaging over all spills the production rate per spill calculated from the individual production rates showed only a difference of about 10 % compared to the production rates calculated by the recursive formula. This justifies the chosen approach.

In the experiment O16G250 one spill too much was delivered because the beam request was stopped too late by the operator. In the experiment C12G260 the irradiation was interrupted due to accelerator problems after the 117-th spill and it was decided to not deliver the remaining 3 spills. These difference in number of delivered spills does not compromise the comparison with other experiments because the $\beta^+$-activity production rates are calculated per spill and the backprojections do not depend on the number of delivered spills.

**Table 2.3:** *Parameters of the irradiation with $^{16}O$.*

| ID | Target | E [AMeV] | R [cm] | Number of spills | Intensity per spill | duration spill [s] | duration pause [s] | Number of events |
|---|---|---|---|---|---|---|---|---|
| O16W350 | water | 350 | 16.4 | 120 | $8.35 \cdot 10^7$ | 1.83 | 1.97 | $3.81 \cdot 10^7$ |
| O16W300 | water | 300 | 12.7 | 120 | $5.43 \cdot 10^7$ | 1.72 | 2.00 | $3.05 \cdot 10^7$ |
| O16W250 | water | 250 | 9.3 | 120 | $6.20 \cdot 10^7$ | 1.91 | 1.73 | $2.46 \cdot 10^7$ |
| O16W200 | water | 200 | 6.3 | 120 | $7.63 \cdot 10^7$ | 1.98 | 1.67 | $1.78 \cdot 10^7$ |
| O16P350 | PMMA | 350 | 14.3 | 120 | $9.94 \cdot 10^7$ | 1.84 | 1.95 | $2.75 \cdot 10^7$ |
| O16P300 | PMMA | 300 | 11.0 | 120 | $4.23 \cdot 10^7$ | 1.85 | 1.97 | $2.16 \cdot 10^7$ |
| O16P250 | PMMA | 250 | 8.1 | 120 | $5.71 \cdot 10^7$ | 1.83 | 1.81 | $1.67 \cdot 10^7$ |
| O16P200 | PMMA | 200 | 5.5 | 120 | $5.81 \cdot 10^7$ | 2.01 | 1.56 | $1.14 \cdot 10^7$ |
| O16G350 | graphite | 350 | 10.7 | 120 | $8.60 \cdot 10^7$ | 1.94 | 1.94 | $1.72 \cdot 10^7$ |
| O16G300 | graphite | 300 | 8.3 | 120 | $6.34 \cdot 10^7$ | 1.89 | 1.93 | $1.34 \cdot 10^7$ |
| O16G250 | graphite | 250 | 6.0 | 121 | $5.81 \cdot 10^7$ | 1.74 | 2.06 | $1.05 \cdot 10^7$ |
| O16200G | graphite | 200 | 4.0 | 120 | $7.05 \cdot 10^7$ | 2.03 | 1.53 | $7.28 \cdot 10^6$ |

## 2.3   Results and discussion

### 2.3.1   Production rates

**Correction factor**

The detection efficiency was measured by putting a $^{22}$Na source into the center of the FOV of the detector. The actual activity of the source was 2.07 MBq and in 5 minutes 13 270 612 annihilations were detected. This leads to an annihilation detection efficiency of 2.14 %.

In the calculation of the correction factor $\mathcal{C}$ scatter corrections were not performed because only a few lines of response were found outside of the beam path. Therefore, Compton scattering plays a minor role and needs not to be corrected. It can also be assumed that the scattering of annihilation photons produced by the $\beta^+$-activity of $^{12}$C and $^{16}$O beams is similar because the $\beta^+$-active nuclei are of the same type and only their distribution is different. The correction factors $\mathcal{C}$ are shown in table 2.4 and table 2.5.

**$^{12}$C beams**

The production rates of the water and PMMA experiment with the $^{12}$C beam were fitted by using the nuclei $^{11}$C, $^{15}$O and $^{10}$C for the equations (2.2), (2.3) and (2.4). Several other combinations including also $^9$C, $^{14}$O and $^{13}$N were tried but did not fit the activity or gave an activity contribution of less than 3 % with big fitting errors.

For the graphite target only $^{11}$C and $^{10}$C were used for fitting. Fits also including $^{9}$C and $^{8}$B showed no agreement with the experimental decay. Results are shown in table 2.4 where the production rates are converted to number of particles produced per $10^6$ primaries to enable a better comparison with other results.

**Table 2.4:** *Amount of isotopes created by an irradiation with a 260 AMeV $^{12}$C beam of targets of water, PMMA and graphite. IP means incident particles.*

| ID | $\mathcal{C}$ $\times 10^{-3}$ | $N_{^{11}C}$ /$10^6$ IP | $\triangle$ % | $N_{^{15}O}$ /$10^6$ IP | $\triangle$ % | $N_{^{10}C}$ /$10^6$ IP | $\triangle$ % | dA/dt [Bq / s] |
|---|---|---|---|---|---|---|---|---|
| C12W260 | 8.4 | 117907 | 20 | 92659 | 20 | 5465 | 25 | 805 |
| C12P260 | 6.4 | 193337 | 20 | 39695 | 20 | 13449 | 20 | 819 |
| C12G260 | 3.9 | 324265 | 20 | – | – | 21843 | 35 | 970 |

## $^{16}$O beams

The irradiation of the graphite targets with $^{16}$O beams could be fitted best with $^{11}$C, $^{15}$O and $^{10}$C. Using additionally $^{14}$O resulted in about 4 % activity contribution from $^{14}$O right after the irradiation end but calculating the production rates did not work because it was not possible to fit the activity in the spill breaks. Using $^{13}$N instead of $^{14}$O gave negative values for the activity contribution of $^{13}$N.

The best results for fitting the water targets could be obtained by using $^{11}$C, $^{15}$O and $^{13}$N. Using additionally also $^{14}$O gave a curve which matched the decay but the number of $^{13}$N nuclei was negative.

For $^{16}$O on PMMA 3 combinations of nuclei did fit the decay curve well. These combinations are $\{^{10}$C, $^{11}$C, $^{15}$O, $^{13}$N$\}$, $\{^{11}$C, $^{15}$O, $^{13}$N, $^{14}$O$\}$ and $\{^{11}$C, $^{15}$O, $^{13}$N$\}$. In the first combination the number of $^{10}$C nuclei was only 0.12 % of the total number of produced $\beta^+$-emitters, therefore it was rejected. The second set was not further used because the calculation of the production rates failed because it was not possible to fit the activity during spill breaks with this set. This behavior was found for all 4 energies used. Therefore, for the PMMA targets only $^{11}$C, $^{15}$O and $^{13}$N were used. The resulting production rates per spill were converted to number of particles produced per $10^6$ primaries to make comparison with experiments with a different number of delivered spills or different intensities per spill easier. Results are shown in 2.5.

For the experiments with the higher energies the activity at the end of the irradiation was very high. This is good for the backprojections but is not optimal for the fitting of the decay because dead time effects cannot be excluded. In general the calculated production rates show the expected tendency, the decrease with decreasing energy. But for experiment O16G350 the

calculated production of 483430 $^{11}$C , 39730 $^{15}$O and 26355 $^{10}$C nuclei per $10^6$ looks not very reasonable for two reasons. First the total production is too high. These production means that more than half of the incident particles undergo fragmentation reactions leading to $\beta^+$-emitters. Taking into account that also not $\beta^+$-active nuclides produced one can assume that most of the primaries are removed from the beam and cannot create a Bragg peak any more. Such an behavior is not known. The second problem is the ratio between $^{11}$C and $^{15}$O. $^{15}$O arises only from projectile fragmentation and it can be therefore expected that it gives a much higher contribution. However, figure 2.5 shows a plot of the activity build up and the decay afterwards based on the relative production rates from table 2.5 compared with the measured activity. These figure justifies the ratio between $^{11}$C and $^{15}$O. Because this figure shows relative production rates no conclusion about the absolute value can be drawn from it.

The PMMA and water experiment gave more reasonable results. The total amount of produced nuclei is lower than in the graphite case and the contribution of $^{15}$O is reasonable.

Figure 2.5 shows a comparison between and calculated count rates for $^{16}$O beams of 350 $A$MeV (left) and $^{12}$C beams of 260 $A$MeV (right). The experimental count rates are shown in black calculated values in colour. First row shows PMMA targets, second water and the third graphite. Best results were obtained for $^{12}$C on PMMA and water (figure 2.5 right column, first and second picture). Build up and decay are matching. This justifies the choice of nuclides for fitting and proofs that the obtained relative production rates are reasonable. For $^{12}$C on graphite the black line which shows the experimental count rate indicates that the experimental conditions were not good. After about 100 seconds a longer interruption of the irradiation took place an the count rates dropped immediately. At the end of the irradiation further interruptions took place.

The left column in figure 2.5 shows the $^{16}$O irradiation. For the graphite and the PMMA target also interrupts can be seen. Looking only at the decay after irradiation end a good agreement between experiment (black) and calculation (blue) is shown. This justifies the isotopes used for fitting. However, the build up is not reproduced well. A reason for that is surely the contribution of isotopes with a short half-life like $^{14}$O or $^9$C which are neglected. An other reason could be the dead time of the detector towards irradiation end. Dead time of the detector would lead to a flattening of the count rates towards irradiation end and short time after the irradiation. Then the fit done after irradiation end would lead to a lower contribution of isotopes with a short half-life especially the abundant $^{15}$O or $^{10}$C. This could be the reason why $^{10}$C could not be found in the experiments of $^{16}$O on PMMA.

**Table 2.5:** *Isotopes created by a $^{16}O$ beam.*

| ID | $\mathcal{C}$ $\times 10^{-3}$ | $N_{^{11}C}$ /$10^6$ IP | $\triangle$ % | $N_{^{15}O}$ /$10^6$ IP | $\triangle$ % | $N_{^{10}C}$ /$10^6$ IP | $\triangle$ % | $N_{^{13}N}$ /$10^6$ IP | $\triangle$ % | dA/dt [Bq / s] |
|---|---|---|---|---|---|---|---|---|---|---|
| O16W350 | 7.1 | 93479 | 20 | 198204 | 20 | – | – | 52433 | 35 | 1238 |
| O16W300 | 8.9 | 65889 | 15 | 143116 | 20 | – | – | 30223 | 25 | 884 |
| O16W250 | 8.9 | 53688 | 15 | 120079 | 20 | – | – | 21120 | 25 | 736 |
| O16W200 | 9.2 | 37254 | 15 | 84576 | 20 | – | – | 12039 | 30 | 514 |
| O16P350 | 6.7 | 255728 | 20 | 112443 | 20 | – | – | 16575 | 35 | 804 |
| O16P300 | 6.7 | 196441 | 15 | 101981 | 20 | – | – | 11489 | 30 | 703 |
| O16P250 | 6.8 | 135985 | 20 | 84084 | 25 | – | – | 9613 | 30 | 565 |
| O16P200 | 7.0 | 85119 | 15 | 61898 | 20 | – | – | 6448 | 25 | 407 |
| O16G350 | 3.9 | 483430 | 25 | 39730 | 25 | 26335 | 35 | – | – | 1448 |
| O16G300 | 4.0 | 357671 | 25 | 40403 | 30 | 20165 | 40 | – | – | 1158 |
| O16G250 | 4.9 | 227436 | 25 | 36046 | 25 | 10756 | 35 | – | – | 721 |
| O16G200 | 5.0 | 132790 | 20 | 27814 | 30 | 7559 | 40 | – | – | 505 |
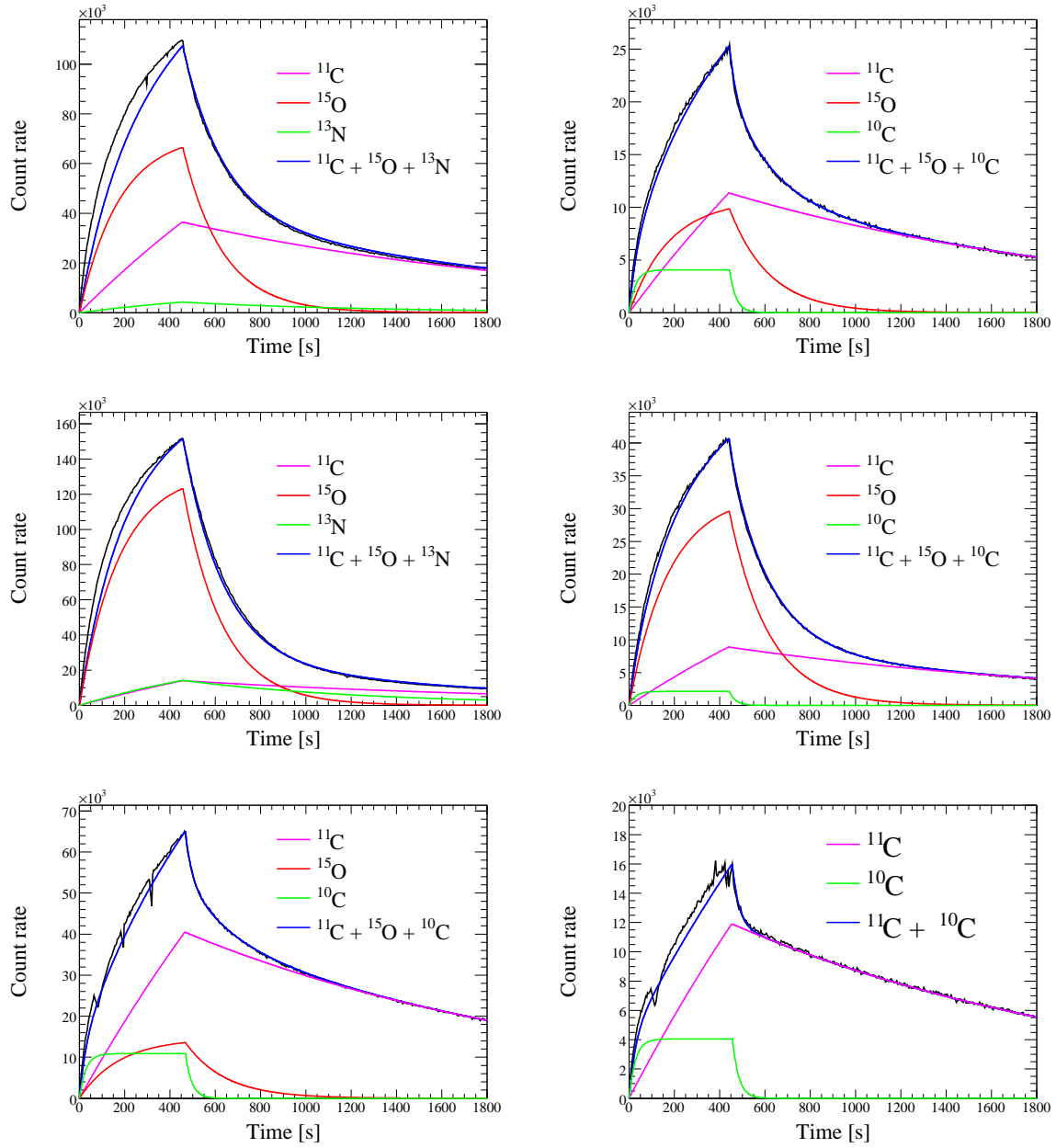
**Figure 2.5:** *Comparison between experimental and calculated count rates for $^{16}O$ beams of 350 AMeV (left) and $^{12}C$ beams of 260 AMeV (right). The experimental count rates are shown in black calculated values in colour. The sum of all individual count rates is given in blue. First row shows PMMA targets, second water and the third graphite.*
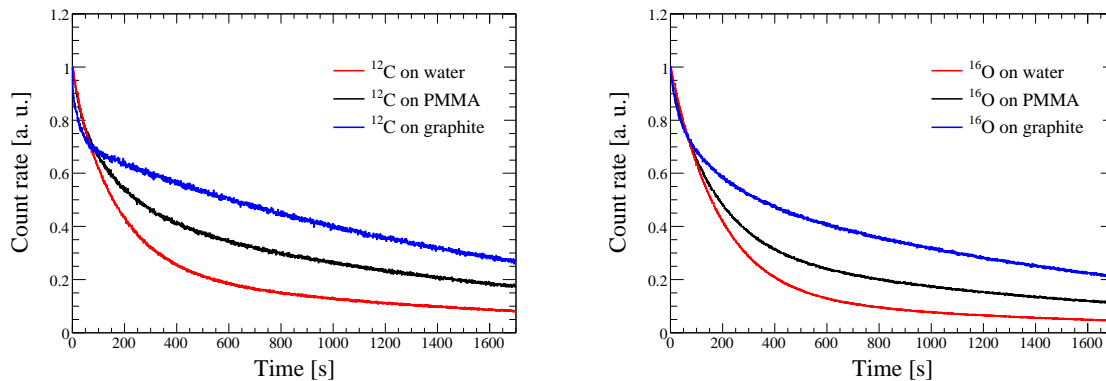
## 2.3.2 Decay curves



**Figure 2.6:** *Comparison between count rates in PMMA, water and graphite measured after irradiation end. The left picture shows the activity produced by 260 AMeV $^{12}$C beams, the right picture shows the activity produced by 300 AMeV $^{16}$O beams. The energies correspond to about the same particle range.*

In figure 2.6 a comparison between decay curves i.e. count rates obtained after irradiation end are shown. The left picture shows the activity produced by 260 $A$MeV $^{12}$C beams on PMMA, water and graphite. The the right picture shows the decay curves by 300 $A$MeV $^{16}$O beams on the same target materials. The energies of the two beams correspond to the same particle range. The curves are normalized to the count rate at the begin of the decay measurement.

Comparing the decay curves of both beams it can be seen that the count rates at the first 100 seconds show about the same slope for all targets and both beams. Afterwards the countrates for PMMA and water drop faster for the oxygen irradiation. This can be explained by the fact that at the beginning the activity is dominated $^{15}$O and at the end by $^{11}$C (only for $^{16}$O irradiation). Obviously there is much more $^{15}$O in the experiments with $^{16}$O beam due to projectile fragmentation.

For $^{12}$C on graphite the decay curve first falls fast and then, after about 100 seconds, not as steep any more. This behavior is due to the contribution of $^{10}$C (half-life 19 seconds) at the beginning which becomes negligible compared to the $^{11}$C activity after about 100 seconds. For $^{16}$O on graphite this cannot be seen because apart $^{10}$C and $^{11}$C also $^{15}$O contributes.

In [Fie06] decay curves of $^{12}$C induced activity for the same targets measured by in-beam PET at GSI are shown. The energy of the beam was 337.5 $A$MeV, a little bit higher than the 260 $A$MeV $^{12}$C beams shown in figure 2.6 but the decay curves look the same for both energies.

**Activity ratio**

The ratio $r$ of the absolute production rates between $^{12}$C and $^{16}$O irradiations can be calculated by [Par02]:

$$r = 0.56 \frac{A_{^{16}O}}{A_{^{12}C}} \tag{2.14}$$

where the factor 0.56 accounts for the different stopping power of $^{12}$C and $^{16}$O ions given in [ICR05]. This factor is almost the same for all used targets (i.e. water, PMMA and graphite). The activity created per second is given in tables 2.4 and 2.5.

The activity ratio $r$ calculated by equation (2.14) is 0.61 $\pm$ 0.2 for water, 0.48 $\pm$ 0.1 for PMMA, and 0.66 $\pm$ 0.2 for graphite. Assuming that the $\beta^+$-activity produced in human tissue is similar than the $\beta^+$-activity produced in PMMA or water one can expect to have about a 50 to 60 % less activity in a $^{16}$O patient treatment with the same dose with respect to a $^{12}$C beam.
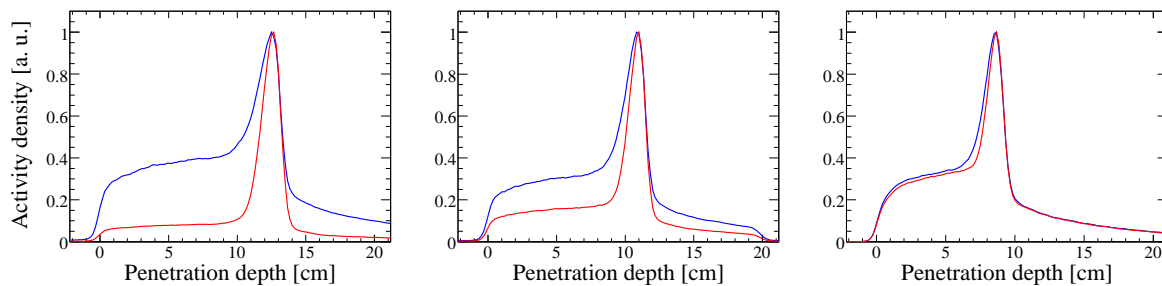
### 2.3.3   Backprojections



**Figure 2.7:** *Activity profiles of $^{12}$C beams of 260 AMeV on different targets. Left side shows water, in the middle is PMMA and on the right graphite. The blue lines are the backprojection during the spill breaks, the red line is from 10 to 20 minutes after irradiation end. The activities are normalized to the maximum.*

Two backprojections were performed for each experiment, one during the spill pauses and one from 10 to 20 minutes after irradiation end.
The average activity during spill pauses is an average from a low activity at the first breaks up to a high activity towards the end of the irradiation. Therefore, no proper normalization to the activity for the two backprojections at different times could be found and a normalization to the maximum was chosen. The advantage of this normalization is that changes in shape and position of the peak are clearly visible. The disadvantage is that the activity during and after irradiation could be confused because the activity after irradiation covers a bigger area

for the experiments with the $^{16}$O beams.

The backprojections for the 260 $A$MeV $^{12}$C beam experiments are shown in figure 2.7. The left figure shows water, middle figure shows PMMA a the right side shows graphite. The blue lines are the activity during spill breaks, the red lines are the activity after the irradiation. The profiles show a sum over the central $\pm$ 5 voxels (a cube with edge length of 1.6875 millimeter). Interesting is the case of $^{12}$C on graphite because projectile and target are the same nuclei and only $^{11}$C and $^{10}$C can be produced in significant amounts. $^{10}$C is produced the same way as $^{11}$C therefore, the only difference in the distribution is the $^{10}$C produced as projectile fragments due to a different range because of its different A/$Z^2$ ratio compared to $^{11}$C. This explains the small difference in the two backprojections in figure 2.7, left. The position of the peak changes only marginally over time, values are given in (cf. table 2.6).

The $\beta^+$-activity profiles of $^{16}$O beams of various energies on different targets are shown in figure 2.8. Left column shows water targets, middle column PMMA and the right one graphite. Each row shows an other energy, from top to bottom: 350, 300, 250 and 200 $A$MeV.

For the activity backprojected during the spill breaks, apart from the irradiation with 200 $A$MeV, a more or less flat part is produced. In the 200 $A$MeV experiment the penetration depth is too short to produce a plateau. For the backprojections done from 10 to 20 minutes after irradiation end (cf. red lines in figure 2.8) for the PMMA phantoms the activity shows a small slope. For graphite the slope is even stronger and for the lowest energy no plateau is produced anymore.

The position of the peak is not constant over time. The reason is that during the irradiation the peak is dominated by $^{15}$O but for the second backprojection $^{15}$O does not contribute anymore. Therefore, the peak is dominated by $^{11}$C and $^{13}$N. The obtained peak positions at different times and their differences are shown in 2.6. Up to 0.53 centimeter were found.

**Table 2.6:** *Shift of the $\beta^+$-activity peak between a backprojection during spill breaks and 10 to 20 minutes after irradiation end.*

| ID | Peak position during [cm] | Peak position after [cm] | difference [cm] |
|---|---|---|---|
| O16P350 | 13.61 | 14.05 | 0.43 |
| O16P300 | 10.54 | 10.92 | 0.38 |
| O16P250 | 7.60 | 7.88 | 0.28 |
| O16P200 | 5.10 | 5.29 | 0.19 |
| O16W350 | 15.82 | 16.35 | 0.53 |
| O16W300 | 12.07 | 12.52 | 0.45 |
| O16W250 | 8.74 | 9.10 | 0.36 |
| O16W200 | 5.80 | 6.07 | 0.27 |
| O16G350 | 10.82 | 11.17 | 0.35 |
| O16G300 | 8.02 | 8.26 | 0.25 |
| O16G250 | 5.44 | 5.61 | 0.17 |
| O16G200 | 3.57 | 3.65 | 0.08 |
| C12P260 | 10.89 | 10.95 | 0.09 |
| C12W260 | 12.54 | 12.60 | 0.09 |
| C12G260 | 8.58 | 8.65 | 0.08 |
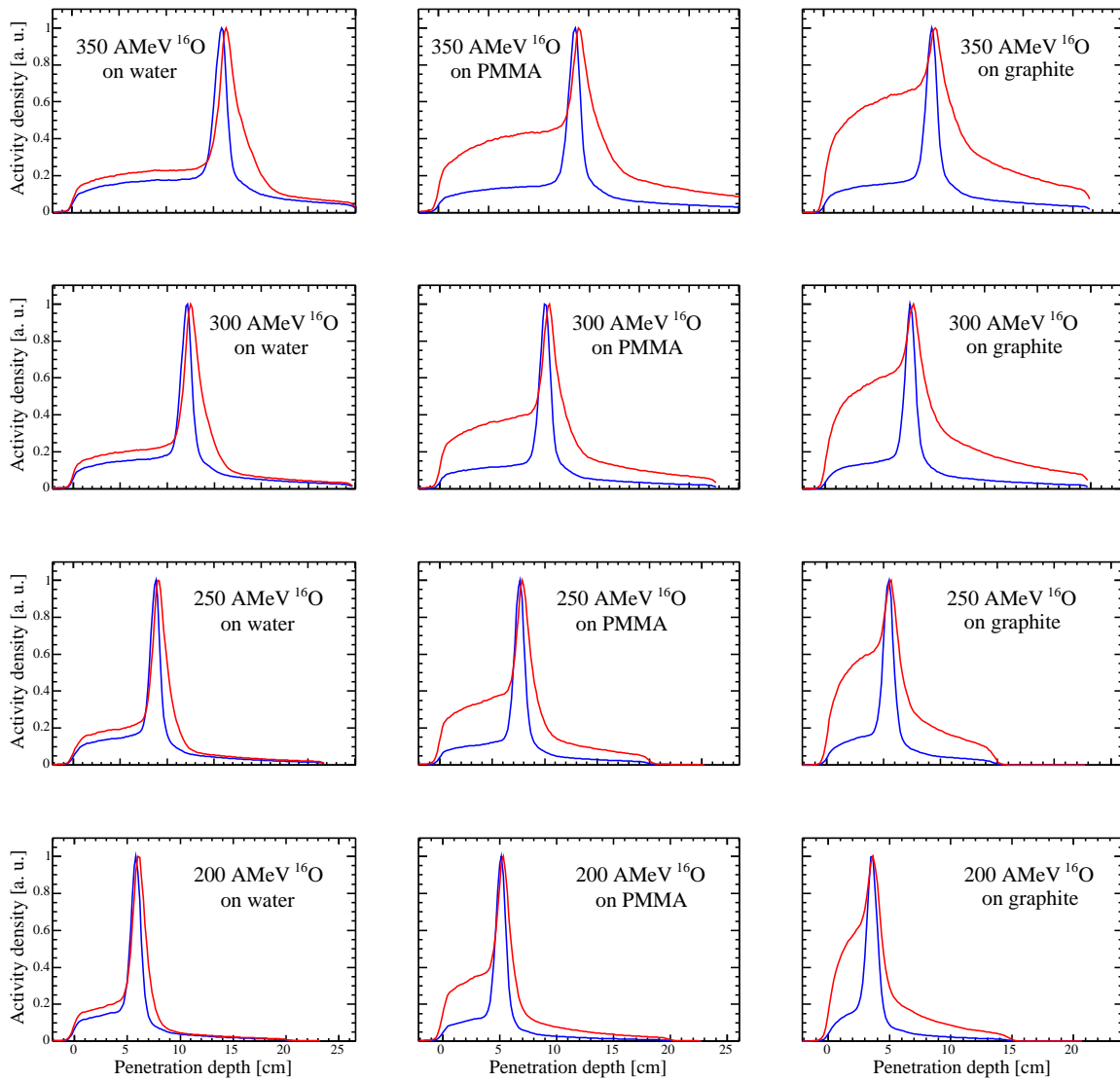
**Figure 2.8:** *Activity profiles of $^{16}O$ beams of various energies on different targets. Left column shows water targets, middle column PMMA and the right one graphite. Each row shows an other energy, from top to bottom: 350, 300, 250 and 200 AMeV. The activity during the spill breaks, normalized to the maximum, is depicted in blue. The red line shows the activity from 10 to 20 minutes after irradiation end, also normalized to the maximum.*

### 2.3.4 Time dependency of peak to plateau ratios

The most remarkable difference between the backprojections of $^{12}$C and $^{16}$O experiments is the change of the peak plateau ratio. It shows the opposite time dependence between $^{12}$C and $^{16}$O beams. For the carbon irradiation it increases after irradiation end, for the $^{16}$O beam it decreases. The origin of that behavior lies in the domination of peak by $^{15}$O and $^{11}$C in the irradiation with $^{16}$O and $^{11}$C and their different half-lives of 20 and 2 minutes respectively.

An exception is the irradiation of graphite with a $^{12}$C beam because the dominant $^{11}$C is produced as projectile and target fragment. Therefore, the activity distribution look almost identical at every time. The small discrepancy between the backprojection (cf. figure 2.7, left) is due to $^{10}$C. As target fragment it contributes additional activity to the plateau to the backprojection done in the spill breaks. $^{10}$C produced via projectile fragmentation contributes to the peak but at lower penetration depth as $^{11}$C because of its lower $A/Z^2$ ratio.
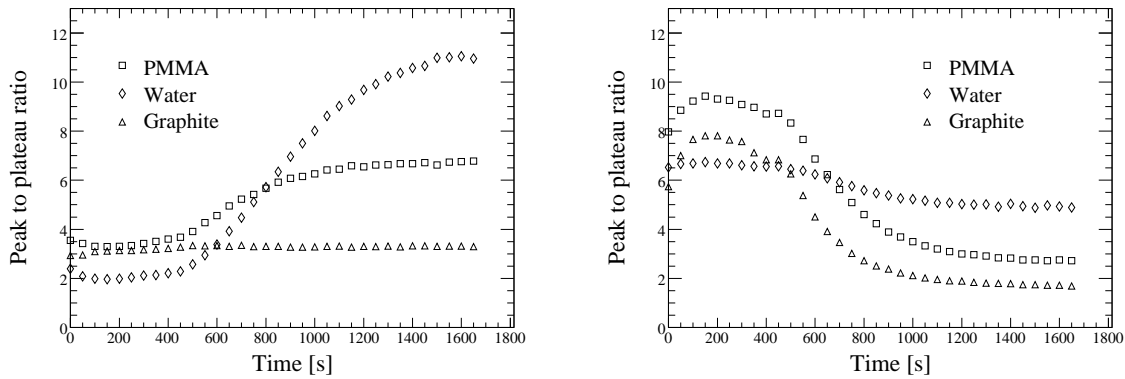


**Figure 2.9:** *Left: Time dependency of the peak to plateau ratio of $\beta^+$-activity produced by a $^{12}C$ beam of 260 AMeV on water, PMMA and graphite. Right: As the left picture but with an $^{16}O$ beam of 300 AMeV.*

The time dependence of the peak to plateau ratio is shown in figure 2.9. The picture on the left side shows the ratio between the height of the peak and the plateau of the $\beta^+$-activity produced by 260 $A$MeV $^{12}$C beams on PMMA, water and graphite targets. The right picture shows the $^{16}$O beams of 300 $A$MeV on the same target materials. The curves were produced by making a backprojection every 50 seconds. The length of the $^{12}$C irradiations were about 440 seconds for PMMA and water and about 454 seconds for graphite. The length of the $^{16}$O irradiations were 458 seconds for PMMA and graphite and 446 for water.

The ratio found in the $^{12}$C irradiation of graphite is almost constant during the irradiation and afterwards. That can be explained by the assumption that in the peak and in the plateau the same nuclides. $^{10}$C and $^{11}$C) are produced in the same amount. For PMMA and water this is different. The ratio rises after irradiation end (cf. figure 2.7). That can be explained

by the $^{11}$C contribution in the peak which drops much slower than the $^{15}$O which gives the main contribution to the plateau. In the case of the $^{16}$O beam irradiation the activity drops after the irradiation. This effect is stronger for PMMA and graphite. An explanation for that is the peak is dominated by the short-lived $^{15}$O and the plateau by the projectile fragments $^{11}$C and $^{13}$N (in the case of PMMA). After irradiation end the $^{15}$O decays faster and therefore, the peak to plateau ratio drops. The ratio for water drops just a little bit. This is because the projectiles and the relevant target nuclei are both $^{16}$O. Therefore, projectile and target fragments are produced the same way and with the same distribution and therefore, the peak to plateau ratio should not change very much over time. The explanation of the observed small drop is the contribution of $^{11}$C target fragments produced in a reaction of two $^{16}$O nuclei.

An other difference between the $^{12}$C and the $^{16}$O irradiations is the ratio during the irradiation. For the $^{12}$C irradiation it is constant but for PMMA and graphite irradiated with $^{16}$O it is not. This is probably because some interruptions of the irradiation occurred and therefore, the $^{15}$O dominated peak dropped in this pauses and could not be built up before the next interruption.

In [Fie06] also time dependend curves of the peak to plateau ratios for $^{12}$C beam induced activity are shown. The experiments were done also with the in-beam PET camera at GSI and the targets are the same as the here presented ones. The only difference compared to the here presented experiments is the energy of the beam, 337.5 $A$MeV and the time structure of the irradiation. During the irradiation a peak to plateau ratio between 2 and 3 was found. Which corresponds to the values found in this work. The ratio of the graphite irradiation was also found constant during and after irradiation. For PMMA after irradiation a value of about 6 was found which is a little bit lower than in the experiments for this thesis. For water the value found in [Fie06] was about 15 compared to the value of 11 found in this work. A reason for this small difference may be the different energy of the $^{12}$C beam used.

### 2.3.5 Range separation

An important quantity monitored by in-beam PET is the particle range. This can only be done when the activity distribution produced by beams of close energies is separable. To investigate the feasibility of activity separation for the activity produced by $^{16}$O beams, 4 PMMA phantoms of type MAT1 (cf. table 2.1) were irradiated with 298.5, 300.0, 301.5, and 303.0 $A$MeV. These energies were chosen according to FLUKA simulations of depth dose distributions (cf. figure 2.10) predicting range differences of roughly 1 millimeter for beams of adjacent energies. This 1 millimeter corresponds to the finest range difference (in water) presently used at GSI for the treatment with $^{12}$C beams.

The experiments were performed at identical conditions like the other experiments with $^{16}$O beams presented in this thesis (i.e. 120 spills, 30 minutes decay time). However, the positioning along the beam is a critical point for this investigation. Because one millimeter of range difference must be resolved, the positioning of the targets has do be done with much higher accuracy compared to the other experiments. It is important to determine the exact relative
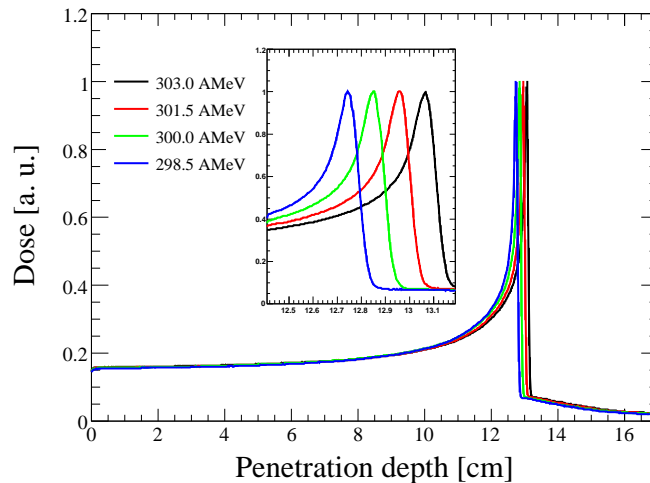
**Figure 2.10:** *Dose of $^{16}O$ beams of 298.5, 300.0, 301.5, and 303.0 AMeV on PMMA simulated by FLUKA, the pad in the middle shows a zoom of the peaks.*

position between the upstream edge of the target and the activity peak. Therefore, on the upstream site of each phantom a $^{22}$Na point source was fixed and measured by PET for 2 minutes. Afterwards the source was removed with care to not move the target anymore and the irradiation was started. A backprojection of the annihilation events occurring only in the time window when the source was present was done. The activity found that way appears not as a point but is bluerred because of the backprojection and was therefore, further fitted by a gauss function to find the maximum which is used as reference point for the activity distribution created by the beam.

The activity distributions found for the four energies are shown in figure 2.11. The profiles show a sum over the central $\pm$ 5 voxels in horizontal and vertical direction. The left figure shows a backprojection during spill breaks and the right figure a backprojection done between 10 and 20 minutes after irradiation end. The figures confirm that it is possible to resolve the different positions of the activity peaks created by two beams having energy differences corresponding to less than 1 millimeter difference in particle range at both time windows.

The position of the peaks are calculated as the mean of a Gauss fit. The results are shown in table 2.7. Also the differences of the position of the activity peaks was found to be about 0.8 to 1 millimeter in both cases during and after irradiation (1 millimeter in water corresponds about 0.85 millimeter in PMMA). It was also found that the change in peak position over time is the same for all energies. The peak shift over time was found to be 3.7 millimeter for all 4 energies. This is more than the difference due to the different energies between a 298.5 and a 303 $A$MeV beam which is about 2.7 millimeter. An illustration of the time dependency is shown in figure 2.12 where different backprojections of a $^{16}$O beam with 300 $A$MeV on PMMA

are shown. All curves are normalized to their maximum. The backprojections are done each for 5 minutes starting 0, 5, 10, 15, and 20 minutes after irradiation end. The change of the peak to plateau ratio is also clearly visible. Figure 2.12 shows also a zoom of the peak which illustrates the moving.

**Table 2.7:** *Position of activity peaks created by $^{16}O$ beams of close energies during the pauses between the spills and 20 minutes after irradiation. The reason for the shift is the domination of different isotopes at different times.*

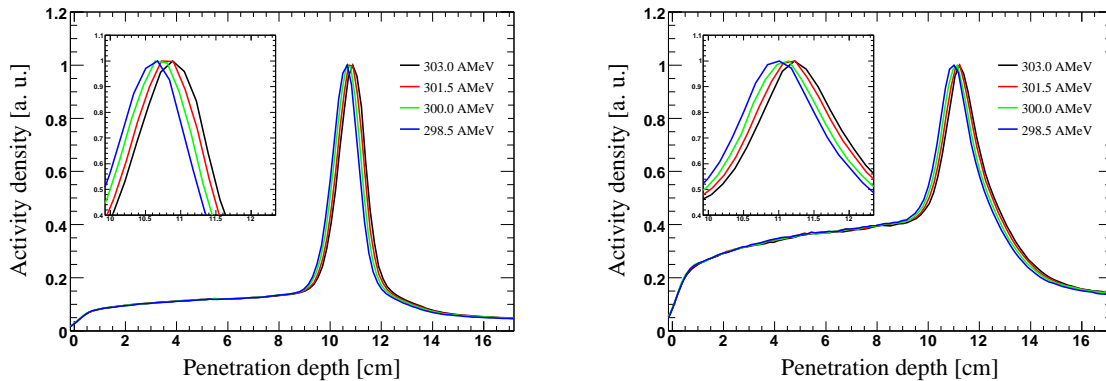| Energy [$A$MeV] | Peak position during irrad. [cm] | Peak position after irrad. [cm] | Difference during–after [cm] |
|---|---|---|---|
| 298.5 | 10.61 | 10.98 | 0.37 |
| 300.0 | 10.70 | 11.07 | 0.37 |
| 301.5 | 10.80 | 11.17 | 0.37 |
| 303.0 | 10.88 | 11.25 | 0.37 |



**Figure 2.11:** *Superposition of $\beta^+$-activity profiles by $^{16}O$ beams of close energy. Left: The back projection was done only in the pauses between the spills. The pad shows a zoom of the peaks. Right: back projection was done for the time window starting 10 minutes after irradiation end and ending 20 minutes after irradiation end.*
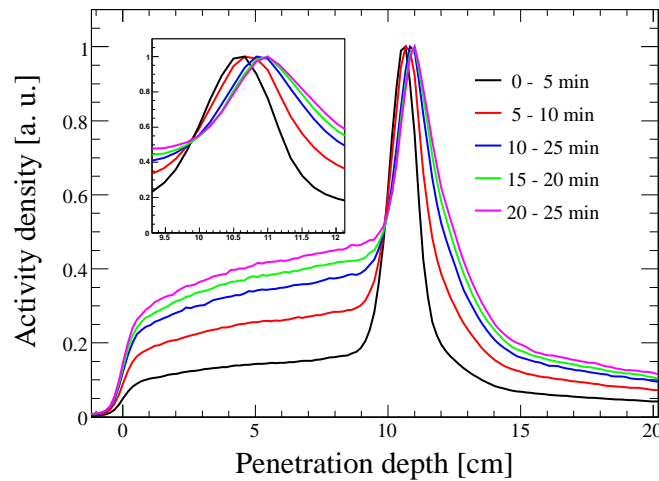
**Figure 2.12:** *Activity created by a 300 AMeV $^{16}O$ beam on PMMA. The back-projections are done each for 5 minutes starting 0, 5, 10, 15, and 20 minutes after irradiation end. The peak to plateau ratio changes over time. The pad shows the change of the peak position over time.*

## 2.3.6 Broadening

### Comparison between beam and $\beta^+$-activity broadening

The purpose of this experiment is a comparison between the broadening of the beam and the broadening of the $\beta^+$-activity. It is not possible to measure both simultaneously therefore, first the beam broadening was measured by a water column of varable thickness and afterwards the $\beta^+$-activity in water was measured. Like in the other experiments gelatine was added to the water to avoid convection (cf. section 2.2.1) The energy used was 350 $A$MeV .
To measure the beam broadening at different petration depth a water column of variable size was used. The length could be changed remotely from outside the cave. This is very comfortable because no time for entering the cave is needed. The whole series of beam broadening measurements was done in about 30 minutes. One multi wire proportional chamber is placed right behind the beam window to measure the broadening before the target. Two other chambers are placed after the water column to measure the broadening in horizontal and vertical direction. The data acquisition software automatically gave a gauss fit of the beam for each spill.

For each thickness 3 spills were used and the average of the three gauss fits was used. The broadening was measured first without the water column and than starting with 4 cm water up to 25 in steps of 1 cm.
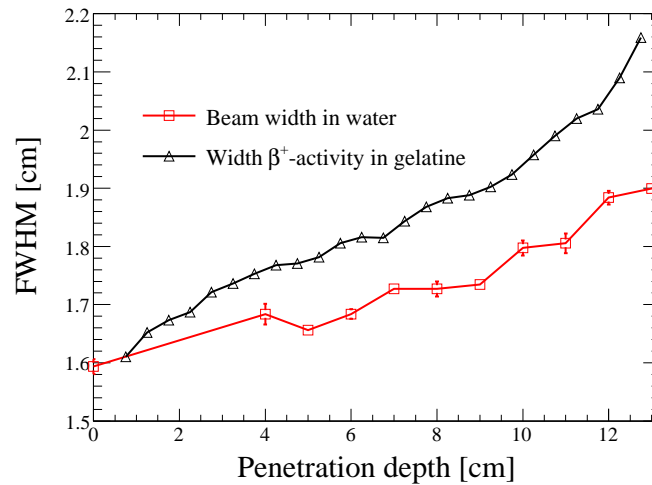
**Figure 2.13:** *Comparison of irradiations with $^{16}O$ beams of 350 AMeV. In red the width of the $\beta^+$-activity in a water target is shown, black is the measured spread of the beam in water. Beacause of convection it is not possible to measure the spread of the $\beta^+$-activity in water.*

The water with gelatine was activated by only 30 spills. It was not necessary to deliver 120 spills like in the other experiments because no fit of the decay after irradiation is needed.

To fit of the activity first a backprojection was done. Then the activity was fitted with a gauss function every 0.5 centimeters. At the entrance of the beam no fit could be performed because of the artifacts of the backprojection. The obtained FWHM is shown in figure 2.13. It was found that the activity has a bigger spread than then beam.

### Activity broadening

From the backprojections already shown in 2.7 and 2.8 broadening information could be obtained by fitting with a Gauss function every 5 centimeters.

Figure 2.14 shows the spread of the activity produced by $^{12}C$ beams in various targets. The left side shows the broadening during the spill breaks and the right side the broadening from 10 to 20 minutes after irradiation end. The experiments were performed in succession therefore, it can be assumed that the beam width was almost the same. It can be seen that the width of the activity is almost the same in the entrance for all three targets measured during the spill breaks. The width obtained in the water and PMMA case are very similar up to 6 cm penetration depth, graphite shows a stronger spread.
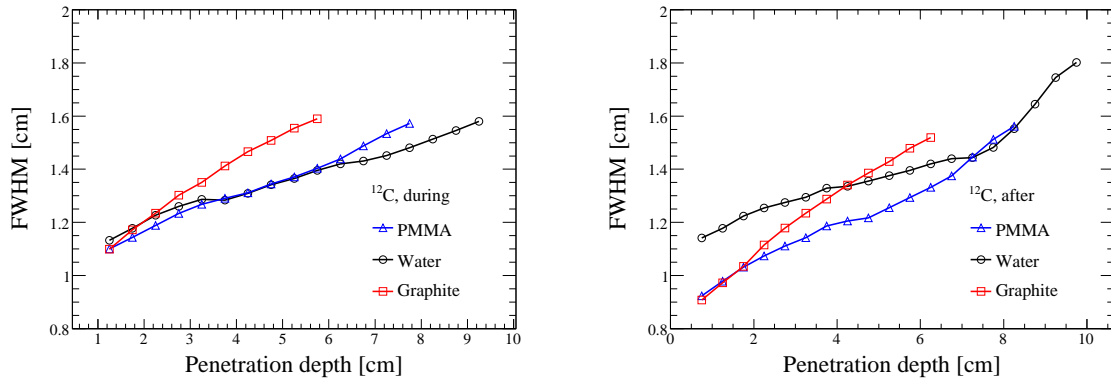
**Figure 2.14:** *Spread of $\beta^+$-activity in targets of PMMA, water and graphite obtained by irradiation with $^{12}C$ beams of 260 AMeV obtained during the beam pauses (left) and 10 minutes after irradiation end for ten minutes (right).*

After irradiation end the initial width of the activity of water and graphite goes down the width of water remains the same. At deeper penetration depths it increases stronger than during irradiation.

The spread of the activity induced by $^{16}$O beams is shown in 2.15. The pictures show the following targets from top to bottom: water, PMMA and graphite. The left side gives the broadening obtained by a backprojection during the spill breaks and the right side shows the broadening from a backprojection done from 10 to 20 minutes after irradiation end. It is remarkable that during the irradiation the increasing of the width obtained for the low energies is much higher than for higher energies. This can be explained simply by the fact that beams with lower energies undergo more lateral scattering and broden therefore more. The steepness of the slope goes down after irradiation end. An explanation for that behavior is that the for deeper penetration the projectile fragments contribute more. For $^{16}$O beams the projectile fragments are $^{15}$O and are not contributing any more for the backprojections performed after irradiation end.

It can be seen that the initial with (i.e. the width at the entrance of the beam) stays the same during and after irradiation for the water target. This is the expected behavior because at the entrance the $\beta^+$-activity is produced only by target fragments and therefore, the width is strongly related to the initial beam with. Because any type of target fragment is produced with the same spatial distribution the width at the entrance should not change over time.

For PMMA and graphite targets the initial width goes down after irradiation end. An explanation for that behavior could not be found.
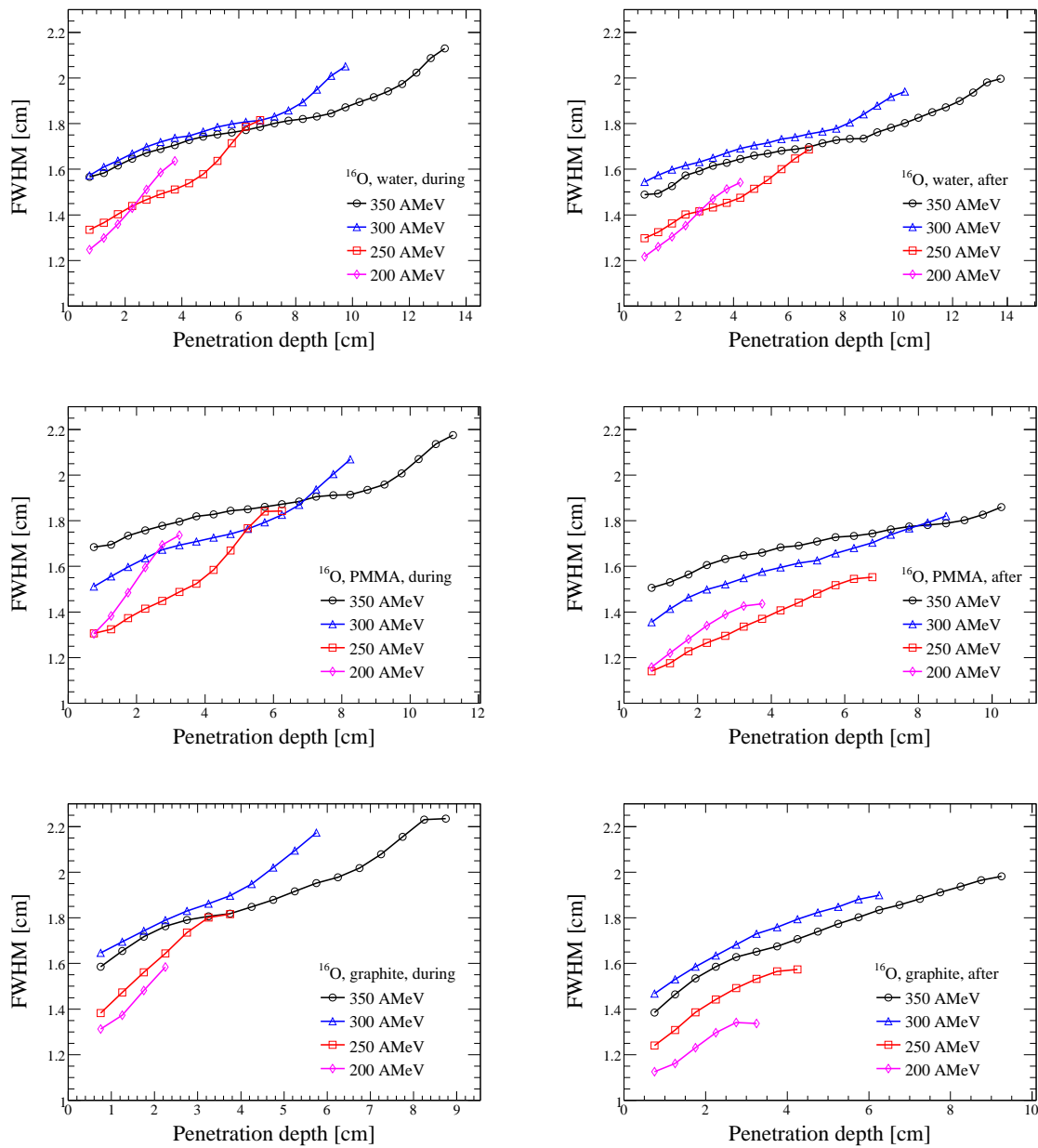
**Figure 2.15:** *Spread of $\beta^+$-activity in various targets obtained by irradiation with $^{16}O$ beams of various energies obtained during the beam pauses (left) and 10 minutes after irradiation end for ten minutes (right). First row shows water, second row is PMMA and graphite is shown in the last row.*

# Chapter 3

# Simulations

## 3.1   Purpose of the simulations

Purpose of the simulations is to investigate the feasibility of FLUKA to predict the $\beta^+$-activity distributions in ion therapy monitoring by means of in-beam PET. Of special interest are $^{12}$C and $^{16}$O beams. $^{12}$C beams because $^{12}$C is presently used at GSI for treatment and will be used in future at HIT. Data of in-beam PET experiments performed with $^{12}$C is available and benchmarking against the code presently used at GSI to simulate the $\beta^+$-activity is possible. $^{16}$O beams are of interest because they will be also available at HIT and up to now no solution for the simulations necessary for in-beam PET has been found. In-beam PET experiments on homogeneous targets were performed (cf. chapter 2) and can be used for benchmarking FLUKA. Also proton and $^3$He beams will be used for treatment at HIT. The feasibility of FLUKA for predicting the $\beta^+$-activity by proton beams on homogeneous and inhomogeneous phantoms was already investigated in [Par02, Par04]. This led to clinical investigations at Massachusetts General Hospital of post irradiation measurements for verifying the treatment with proton beams based on FLUKA simulations [Par07].

For $^3$He beams in-beam PET experiments were performed but up to now FLUKA simulations of these experiments were done only without the BME model. $^3$He ions of 100 $A$MeV have a range of several centimeters. Therefore, without the BME model at the last centimeters no activity can be simulated with FLUKA, resulting in an absence of activity in the most important part i.e. the distal end. However, the simulation of $^3$He beams is behind the purpose of this work.

The 100 $A$MeV nuclear interaction threshold exists also for heavier ions like $^{12}$C and $^{16}$O but it is not such a big problem as for light ions. The lightest $\beta^+$-active nucleus it $^8$B, therefore beams of ions with a mass number lower than 8 cannot produce $\beta^+$-active projectile fragmentation. The projectiles keep almost their momentum and travel further to about the range of the primaries where they form the activity peak. That means that the activity in the peak is created by reactions which take place at all energies. Target fragments are produced everywhere along the path of the particles. Therefore a 100 $A$MeV threshold of nuclear interactions for heavier ions results in missing activity in the peak but still a peak is

present. Depending on the residual range also activity from target fragments is missing before the peak. For light ions which cannot lead to $\beta^+$-active projectile fragments the activity at the last centimeters is missing.

## 3.2   Simulation Methods

The simulations were done in 3 consecutive approaches each more advanced than the one before. The initial step was to perform relative simple, straightforward simulations to get an insight into the abilities of FLUKA. Only the points where $\beta^+$-active nuclei come to rest were scored. The target was modelled as surrounded by vacuum, material in the beam path was neglected. A time dependency was not taken into account.

In the second approach the positron propagation was included and the material in the beam path was modelled. The points of the electron-positron annihilation were scored. The production and decay of the $\beta^+$-emitters was simulated time dependently and a first primitive implementation of smearing effects due to the backprojection was done.

The last improvements were done to simulate the experiments which took place in February 2007. The individual beam profile of each experiment was simulated. To reduce the CPU time full advantage of the biasing abilities of FLUKA was taken and decay direction biasing for annihilation photons was included in FLUKA especially for these simulations. The FLUKA output was given in a special format to enable the conversion to the list mode data format by a modified version of the Pönisch code. This enables to do the backprojections with the same programs that are used for backprojecting the experimental data.

### 3.2.1   Simulations of residual nuclei

First simulations were done in early 2005. These simulations were very simple and were aimed to be compared against the positron emitter data base and recent experimental data. The positron emitter database used for calculating the $\beta^+$-emitter distribution for the in-beam PET simulations at GSI has stored the distribution of $\beta^+$-activity in PMMA created by $^{12}$C beams at all energies used for therapy at GSI. The latest experimental data available was obtained by $^{12}$C beams on gelatine, PMMA and graphite targets by courtesy of Fine Fiedler. The data was in form of preliminary evaluated backprojections and production rates. This data was published in its final form in [Fie06].

The simulation method was to score the $\beta^+$-active residual nuclei (i.e. ions that come to rest) as a function of the penetration depth. The defaults for hadron therapy were used. No biasing was used and time dependency was not taken into account. The simulations were done with the production version of FLUKA on a standard personal computer with an Intel Pentium 4 Processor with 1.8 GHz and 500 MB memory running the operating system Linux Red Hat. Because the computer was used during the day for office work the simulations were done at night or during the week ends or with lower priority in background during the day.

A simulation of a 337.5 $A$MeV $^{12}$C beam on PMMA was performed and compared with the experimental data and the database. The position of the simulated peak of residuals was

within a few millimeter agreement with the database. The shape of the simulated peak of residuals showed very a steep fall of at the distal end. The peak of the residual nuclei in the data base is less steep and less high. The shape of the plateau region was not well reproduced because the database gives a constant plateau and in the simulation an ascending slope was found.

To compare the simulated residual nuclei with the experiment is not straightforward. The shape of the peak of the residuals can be different from the activity peak because the propagation of the positrons and the image processing are blurring the distribution. The simulation does not take into account the time dependency of the activity build up and decay therefore only the backprojection obtained from 10 to 20 minutes after irradiation end was useful. In this time window the activity-distribution is dominated by $^{11}$C which enables a comparison with the simulated $^{11}$C residuals. It is not possible to compare a backprojection obtained during the spill pauses with the residual $\beta^+$-active nuclei because short-lived isotopes contribute more to the activity than isotopes with a long half-life. Therefore the activity distribution looks different at different times. In the comparison between $\beta^+$-activity and the backprojection obtained after irradiation end for the PMMA experiment a missmatch of the peak position was found, similar as in the comparisons of the simulations with the database.

To evaluate the difference between water and gelatine, two simulations of the experiment with the gelatine target were performed. The former was modelling the gelatine as pure water with the standard material properties obtained from [Ste82]. The ionization potential was changed from 75 eV to 80 eV because in dose investigations of $^{12}$C beams on water, performed at GSI, it was found that this value is necessary to reproduce the position of dose peaks [Som06]. The target was modelled with the real stoichiometric composition (i.e. including 0.7% carbon) and also an ionization potential of 80 eV.

**Table 3.1:** *Total amount of $\beta^+$-active isotopes produced by irradiating a gelatine target with $10^6$ $^{12}$C ions at 337.5 MeV/n. To discover the difference between water and gelatine one simulation was done by modelling the target as water, the other simulation was done by modelling the target as gelatine. For both targets an ionization potential of 80 eV was used. The experimental values are taken from [Fie06].*

|  | $^{11}$C | $^{10}$C | $^{9}$C | $^{15}$O | $^{14}$O | $^{13}$N | $^{12}$N | $^{8}$B |
|---|---|---|---|---|---|---|---|---|
| Gelatine | 94936 | 10868 | 1206 | 159686 | 8302 | 12592 | 1096 | 5986 |
| Water | 92443 | 10926 | 1164 | 160131 | 8538 | 12501 | 1122 | 6077 |
| Experiment | 126220 | 7820 | – | 145604 | – | 24036 | – | – |

**Outcome of the simulations of residual nuclei**

The simulation with this residual nuclei approach could be performed in between 6 to 48 hours depending on the energy and target material combination on a standard PC.

The number of residual positron emitter per $10^6$ incident $^{12}$C ions found in the simulations with gelatine and water are shown in table 3.1. In the same table the experimentally obtained residuals are shown for comparison.

The difference in the resulting amounts of $\beta^+$-emitters between the simulation of water and the one of gelatine is small. This confirms the assumption that the use of gelatine instead of water does not influence the results very much. The statistical error for $^{11}$C is about 5 %, for $^{10}$C, $^{14}$O, $^{13}$N, and $^8$B about 10 % and for the rest about 20 %.

However, slightly higher amount of $^{11}$C was found in the simulations with gelatine compared to the simulations of water. This can be well explained by the additional carbon. A slightly higher amount of $^{10}$C in the simulation with water is observed compared to the simulation with gelatine while one could expect the opposite because of the additional carbon in the gelatine target. This discrepancy can be explained by the statistical errors of the simulation. Comparing the simulation with the experiment one observes an about 25 % too low amount of $^{11}$C in the simulation. The amount of $^{15}$O was about 10 % too high and the amount of $^{10}$C about 40 % too high compared to the experiment. $^{13}$N was underestimated by a factor of 2.

For the PMMA targets experimental data of experiments with $^{12}$C beams with 6 different energies from 204 to 343.46 $A$MeV on PMMA were available [Fie05]. All targets had a density of $\rho = 1.18$ g cm$^{-3}$. The other target properties were given by the standard values as described in [Ste82].

**Table 3.2:** *Absolute values of $\beta^+$-emitters produced by irradiating a PMMA target with $10^6$ $^{12}$C ions at different energies. Experimental data is taken from [Fie05] except the values for 337.50 AMeV which are taken from [Fie06]. $^{13}$N and $^{14}$O could not be investigated in the experiment.*

| Energy [$A$MeV] | $^{11}$C Exp | $^{11}$C Sim | $^{15}$O Exp | $^{15}$O Sim | $^{10}$C Exp | $^{10}$C Sim | $^{13}$N Sim | $^{14}$O Sim |
|---|---|---|---|---|---|---|---|---|
| 204.00 | 98927 | 98785 | 19143 | 25188 | 7453 | 5624 | 2544 | 1256 |
| 212.12 | 105052 | 105326 | 21167 | 27315 | 7932 | 6163 | 2677 | 1330 |
| 259.50 | 146461 | 146219 | 30798 | 42487 | 11470 | 8630 | 3727 | 2062 |
| 306.00 | 183421 | 184991 | 40847 | 58269 | 14630 | 11324 | 4548 | 2964 |
| 337.50 | 219600 | 209420 | 51371 | 68212 | 16420 | 12876 | 5256 | 3542 |
| 343.46 | 198681 | 213012 | 50318 | 70148 | 15231 | 13341 | 5193 | 3727 |

The amount of $\beta^+$-active residual nuclei for the simulations of $^{12}$C beams of various energies on PMMA are compared with the experimental values in the tables 3.2 and 3.3.

Good agreement within a few % was obtained. It can be observed that with higher energies the difference between simulation and experiment becomes larger.

Backprojections of the six PMMA experiments were not available therefore, the shape of the activity distributions could not be compared.

**Table 3.3:** *Total amounts of $\beta^+$-emitters of the simulations and experimental data described in table 1.  "All $\beta^+$-emitters" means that additionally to the isotopes $^{11}C$, $^{15}O$ and $^{10}C$ also $^{13}N$, $^{12}N$, $^{9}C$, $^{14}O$, $^{13}O$ and $^{8}B$ have been added to the sum of the simulated nuclei.  "Exp" and "Sim" mean experiment and simulation respectively.*

| Energy [$A$MeV] | $^{11}C+^{15}O+^{10}C$ Exp | $^{11}C+^{15}O+^{10}C$ Sim | all $\beta^+$-emitters Sim |
|---|---|---|---|
| 204.00 | 125523 | 129597 | 137428 |
| 212.12 | 134151 | 138804 | 147148 |
| 259.50 | 188729 | 197336 | 209025 |
| 306.00 | 238898 | 254584 | 269414 |
| 337.50 | 287391 | 290508 | 307547 |
| 343.46 | 264230 | 296501 | 313722 |

Experimental data of $^{12}$C ions on a $9\times9\times15$ cm $\rho = 1.795$ g cm$^{-3}$ graphite target were available.  This experiment was simulated with $10^6$ primaries.  The total amount of $^{11}$C and $^{10}$C for both the simulation and the experiment is given in 3.4 In the simulation also small amounts of other $\beta^+$-active nuclei could be found but their amount can be neglected.

**Table 3.4:** *Absolute values of $\beta^+$-emitters produced by irradiating a graphite target with $10^6$ $^{12}C$ ions at 337.5 $A$MeV.  Experimental data is taken from [Fie06]*

|  | $^{11}C$ | $^{10}C$ |
|---|---|---|
| Exp | 248640 | 18794 |
| Sim | 260264 | 11846 |

The total amount of $^{11}$C and $^{10}$C together is 267434 in the experiment and 272110 in the simulation.  The difference is about 2 %.  In the simulation also low amounts of other $\beta^+$-active nuclei could be found.  For $10^6$ incident particles 388 $^9$C, 51 $^{13}$N, 1128 $^{12}$N, 5822 $^8$B and 1 $^{13}$O could be found.  Adding these particles to $^{11}$C and $^{10}$C leads to a total amount of 279500 $\beta^+$-emitters.  This differs about 5% from the total amount found in the experiment.  Some conclusions could be drawn after this first series of simulations:

- The simulations could be done within reasonable time on an standard PC.

- The results found by this first primitive simulations were encouraging in terms of produced residual nuclei.

- The simulations showed that it is necessary to model with more accuracy the material in the beam to obtain the right peak position in case of the 337.5 $A$MeV $^{12}$C beam on PMMA. For the other experiments activity distributions were not available.

- The comparison of the backprojected activity of the 337.5 $A$MeV experiment showed also the necessity to model the propagation of the positrons because the position of the annihilation is not identical with the position of the decay.

- Artefacts arising from the backprojection especially at the begin of the target should be also be modelled to enable more reliable comparisons.

- It is also necessary to simulate the time dependency of the irradiation to get the right activity distributions during the irradiation.

### 3.2.2 Simulations of annihilation points

While the first simulations were focusing on the production of $\beta^+$-emitters, the second series was aimed to investigate deeper the distribution of the $\beta^+$-activity. With the production version of FLUKA it is only possible to simulate nuclear interactions down to 100 $A$MeV by using the RQMD model. For investigating the activity distributions it is necessary to cover also interactions that lead to $\beta^+$-emitter at lower energies otherwise the production at the end of the particle range would be underestimated (cf. discussion on page 63). At the time when the work on this improved simulations begun BME was recently included into the development version of FLUKA. To take advantage of BME the development version was installed on the same computer where the simulations of the residual nuclei were performed.

Because the simulations should be compared with experimental $\beta^+$-activity distributions the material in the beam was modelled. The material in the beam is the air, beam diagnostic devices like ionization chambers, the beam window and the ripple filter. A ripple filter is a passive device to broaden the Bragg peak of beams with low energies [Web99]. It is made of a 3 millimeter thick plate of PMMA with periodical grooves. Because this device is aimed to changes the beam width and the momentum spread it has to be modelled in detail. This was done by using the LATTIC option in FLUKA, which enables the simulation of periodical geometrical structures. The other material in the beam was only known in terms of density and thickness but not in chemical composition, therefore a detailed simulation was not possible. However it is not necessary to model this material exactly on the right place because it has equal thickness over the with of the beam. For the fragmentation it is also not too important of which material it consits hence it was modelled as water. The targets were modelled the same way as in the previous simulations.

The default option for hadron therapy was used again. The decay was simulated to enable the investigation of the time dependency of the activity distribution. The time and position of the electron-positron annihilation was scored. The scoring was done event by even by writing formatted to a file the position of an annihilation event, A and Z of the residual and the time when the decay happens.

In the experiment 120 spills were used. The duration of the whole irradiation inclusive pauses was 556 seconds. For simplicity a constant irradiation of 556 seconds was simulated. For the evaluation after irradiation end this should have no compromising effect. The experimental backprojection during the irradiation is done only during the pauses of the spills. Therefore, in the experimental backprojection the activity of nuclides with a very short half live is suppressed a little bit. However, it is not estimated that these nuclides give a big contribution to the total activity. Additionally the scoring during the whole irradiation enables to score more annihilations. The activity after the irradiation was evaluated at the same time window as used for the backprojection of the measured activity i.e. from 10 minutes to 20 minutes after irradiation end. This leads to the problem in the simulation that residuals which are decaying outside of the before mentioned time windows do not contribute to the activity distribution. Therefore CPU time is wasted for creating residual nuclei which are not scored. To overcome

this problem the RADDECAY option was used which allowes to replicate the decay of each residual several times. It was chosen to use 5 replicas of each created radioactive nucleus.

It is known that by the PET detection and the backprojection the activity is smoothed by a Gaussian of about 7 millimeter FWHM. To include this effect also in the simulation the obtained activity distributions were folded with a Gaussian kernel of 7 millimeter FWHM.

Because the development version was used some bugs in the code were discovered. All the bugs could be fixed and at the end the simulations could be performed without any problems.

**Outcome of the simulations of annihilation points**

For the water and PMMA targets $3 \cdot 10^5$ primary $^{12}$C ions and for the graphite target $2 \cdot 10^5$ primaries were simulated. The duration of the simulations was about 50 hours of CPU time for PMMA and water targets and about 28 hours for the graphite target.

The resulting activity distributions are shown in figure 3.1. The experimental distributions are obtained by summing the activity over the central $\pm 10$ voxels with respect to the central beam position in the two central longitudinal planes. The voxel dimension is 1.6875 mm$^3$. The blue lines show the experimental backprojections, the red lines the simulation results and the black lines show the experimental results smoothed with a 7 millimeter FWHM Gaussian to take into account the smoothing by detection and backprojection processes. The necessity of the smoothing can be seen in the experimental distributions. The upstream end of the targets is always at 0 centimeters but due to the backprojection activity was found already in front of the target. An additional effect which could not be corrected in the simulations is that for the backprojection obtained during the irradiation the activity before and behind the targets does not drop to zero but stays constant at about 0.05% of the activity maximum. In the backprojection obtained from 10 to 20 minutes after irradiation end no such effect was found.

All simulated activity distributions show a more or less pronounced slope in the activity plateau. For the simulated activity distributions on PMMA and water obtained after the irradiation this slope is not very dramatic but visable. During irradiation all simulations show a very pronounced slope. It was carefully investigated if the origin of this effect lies in the summation over a narrow region. For the simulation it was found that by using different width for the summation the steepness of the slope can change a little bit but it did not come close to the experimental plateau. For the experimental distribution such an investigation was not possible because the original data was not available. Constant irradiation was assumed in the simulation and all annihilations during the irradiation are taken into account. Compared to the experimental evaluation nuclides with a short half-live give an additional contribution. The contribution of this nuclids could not be investigated because only the point of the electron-positron annihilation was scored but not the corresponding nuclid which undergoes the $\beta^+$-decay. For future simulations the time structure of the beam and the information from which nuclide an annihilation event is arising should be scored. An other reason for the slope could be an effect due to the imaging which is present in the experimental distributions but are missing in the simulation.

For the simulations of water during the irradiation the tail is too high but after irradiation it matches quite good. For the other targets the tail is not reproduced well either but no conclusion can be drawn if it is an effect of the imaging of the simulation. The target sizes used in the experiment with PMMA and graphite are too short to get information about the tail.

The shape of the peaks is well reproduced for all targets at all times. The downstream fall for the PMMA and the graphite target are also well reproduced in both position and shape. For the same targets the upstream rise of peaks starts a little bit too early. The reason for that finding could be the neglection of a momentum spread in the simulation.

The peak to plateau ratio was quite well reproduced in particular for the contribution after irradiation end. At this time the activity is dominated by $^{11}$C. The irradiation of graphite is the only one which shows also a pronounced slope after irradiation end. This experiment is specific because target and projectile are the same nuclide. If all other reasons for the slope (too narrow interval, or imaging effects) can be excluded than the reason for this effect lies maybe in modelling of the reaction of $^{12}$C on $^{12}$C leading to $^{11}$C.

For water a comparison between two ionization potentials was done. In [Som06] a ionization potential of 80 eV was found to reproduce Bragg peakpositions to simulate water in FLUKA for $^{12}$C beams. The results of figure 3.1 show that for the activity distribution 80 eV is not the optimal ionization potential of water to reproduce the activity distribution in FLUKA. The commonly used value of 75 eV [Ste82] gives a much better agreement. An explanation why a different ionization potential is needed for dose and $\beta^+$-activity could not be found. A comparison between a depth dose curve obtained under the same conditions as the activity would be interesting.

The simulation of the annihilation points offered a more detailed view into the abilities of FLUKA. The conclusion that can be drawn after this series of simulations are:

- The CPU time needed was reasonable but much more time is needed to get distribution with less statistical fluctuations.

- The position and shapes of the $\beta^+$-activity peaks are well reproduced.

- For water the best reproduction of the peak position is obtained by using the ionization potential of 75 eV.

- The target sizes were too short to give conclusions about the tail.

- In the plateau region the simulated activity shows a tail which does not match the experimental finding. The origin of this effect is not clear. It could be the wrong modelling of the time structure of the irradiation or an effect due to the imaging.
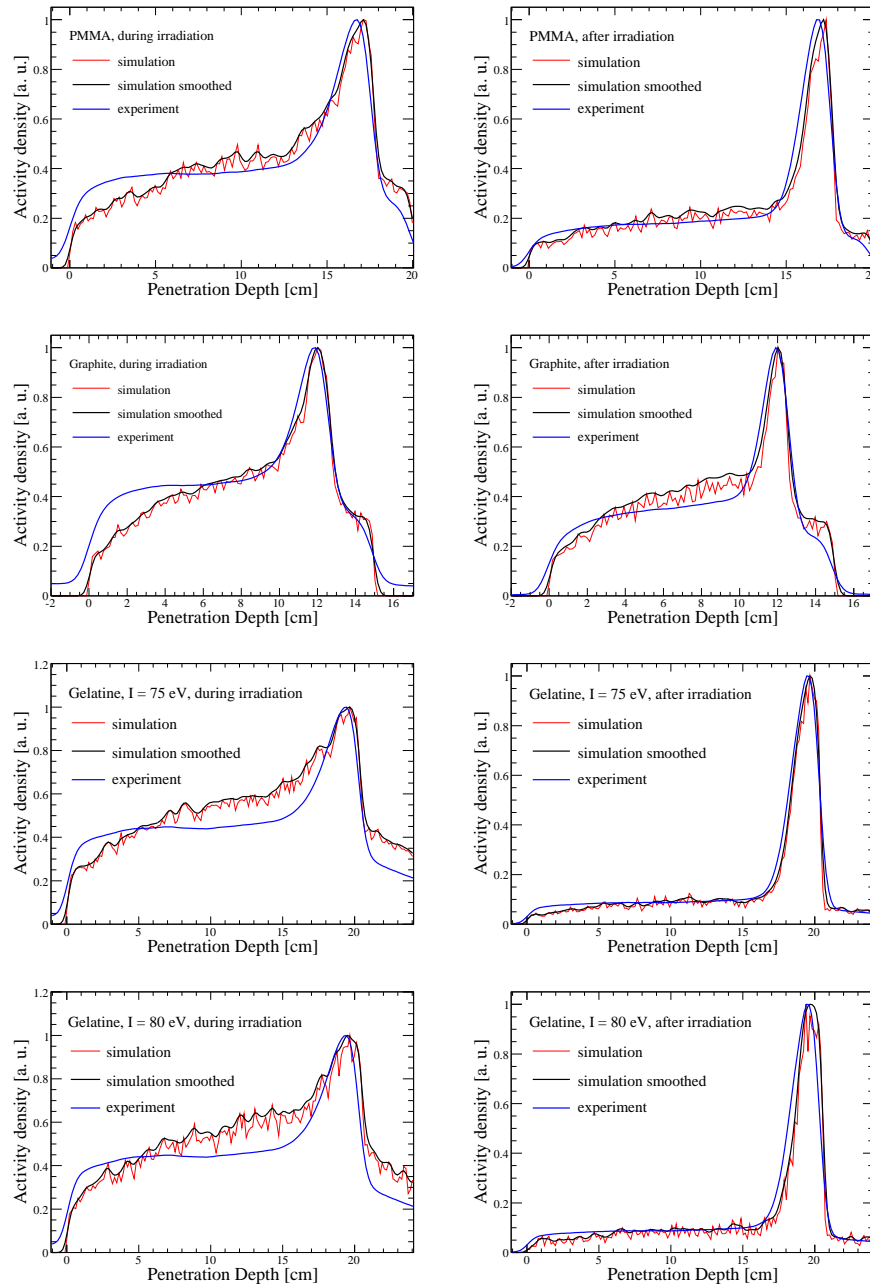
**Figure 3.1:** *Simulation of annihilation points in an irradiation with $^{12}C$ beams of 337.5 AMeV on various targets. The targets are from to to bottom PMMA, graphite and 2 times water. The difference between the 2 water targets is the ionization potential. The blue line are the experimental backprojections during the irradiation pauses (left) and from 10 to 20 minutes after irradiation end (right). The red lines are the simulation results, the black lines are additionally smoothed to take into account a smoothing by the detection ad backprojection processes. All curves are normalized to the maximum.*

### 3.2.3 Final simulation approach

In the final simulations the creation and propagation of the annihilation photons is simulated. The work on this approach started end of 2006, first the same experimental data as in the previous approaches was used but after the experiments in 2007 the new data was used exclusively.

To be as close as possible to the experimental case it was decided to convert the FLUKA output into the list mode data format. The code used to predict the $\beta^+$-activity for the in-beam PET monitoring at GSI is the PETSIM code [Pön04]. This code, written in C, works in a two step approach. The first step is to simulate on base of the treatment plan and the patient CT the creation of the $\beta^+$-active nuclides, their decay, the positron transport, the annihilation and the transport of the photons. The second step is the interaction of the photons with the detector and the signal creation resulting in a list mode data output file in the same format as the output of the PET.

From the PETSIM code the part which simulates the creation of the photons was eliminated and the remaining part was rewritten to read the FLUKA output. The outcoming list mode data can be backprojected with exactly the same routines than the experimental data. By this approach it is possible to eliminate all differences between simulation and experiment due to detection or backprojection.

In FLUKA the modelling of the time structure of the beam was done by using the option IRRPROFI. In 2006 this option had a limit of 20 irradiation intervals that could be simulated in one run. For the here presented simulations 120 spills and 119 breaks have to be modelled therefore, 239 intervals were needed. For the development version the limit of irradiation times was increased to 100. Then the simulations could be done by splitting one simulation into three simulations. The first modeled the first 40 spills and breaks, the second simulation modelled the spills and breaks number 41 to 80 and the last simulation modelled the remaining spills. Each simulation was done with the same amount of primaries because the intensity per spill is constant. The output of the three simulations was merged. After some weeks of using this approach the limit of the number of possible irradiation intervals was further increased by the FLUKA authors in the development version. From this time one all spills could be simulated in the same run. From the version FLUKA2006.3b the increased number of irradiation intervals is also available in the production version.

The annihilation photons were scored on an event by event basis every time an pair of annihilation photons leaves the target. The main information written to the output file is the position of the two photons, the direction cosins, the energies, the time and the A and Z of the decaying nuclide. In an first approach this was done in ASCII format but the size of the files became too big and numbers could not be stored in double precision therefore, the format was changed to binary. Because the FORTRAN output of FLUKA cannot be read by a C program without conversion, a special function[1] allowing to read and interpret FORTRAN output directly was included in the PETSIM code.

---

[1]by courtesy of Vasilis Vlachoudis

Because of the limited solid angle of the detector only about each 50-th pair of annihilation photons is scored, hence at least 50 times more CPU time, compared to the previous approach, is needed to score one annihilation event. These simulations cannot be done any more within reasonable time on a single PC. Therefore, instead of performing the simulations on the computer used for the previous investigations, the simulations were done on the EET cluster at CERN. This cluster consists of 48 computers (nodes), each equipped with a Bi-Processor leading to a total number of 96 available CPUs. 16 nodes have a clock rate of 2.66 GHz, further 16 nodes have 3.0 GHz and the last 16 have 3.2 GHz. Each node has at least 1 GB of memory. The master node is equipped with a Bi-Processor and has 4 GB memory and RAID hard drives of 1 TB. The batch system used is openPBS.

The nodes are not acessable directly. A simulation (job) has to be submitted via the batch system and the system which decides on which node the job is executed. In principle it is possible to specify on which node a job should be performed but this can lead to long waiting if a node is performing calculations for other users. Therefore the nodes were never chosen for the here presented work. Because of the different clock rates the execution time of a job depends the node on which it is performed. It depends further on other processes running on the same node. Therefore, the execution times of the simulations are only an average value.

The power of a computing cluster is due to the possibility to perform parallel calculations. In FLUKA this can be done easily by using input files which differ only in the random seed given.

First simulations were done to simulate the same experiments as with the annihilation points approach. Depending on the target material up to about 100 days of CPU time (30 parallel runs of about 80 hours each) were used to get results with reasonable statistics. Therefore before doing any further refinements in the simulation, ways to improve the execution time where searched.

The first improvement done was the elimination of the delta rays. The simulation of deltarays is a very time consuming process. Delta ray production is switched on with the hadron therapy default because such simulations are normally performed to simulate dose. For a simulation of activity they are not needed. Without delta ray production the simulations were 2 to 5 times faster.

Because of the huge output produced it was checked if the CPU time is slowed down by the permanent I/O. Such a problem could be solved by buffering the output. However, it was found that the I/O is not slowing down the simulations and it was not necessary to add buffered output.

Two main reason for the long execution time needed to get results with reasonable statistics could be identified:

1. $\beta^+$-active residual nuclei which do not decay during the measuring time do not contribute to the activity distribution and are lost.

2. Because of the limited solid angle of the double head detector most annihilation photons do not reach the detector and do not contribute either.

To overcome this problems the option RADDECAY was used again and the number of replicas per residual nuclei was increased to 500. This had a positive effect on both before mentioned problems because each of the 500 replicas is decaying at different times and the annihilation photons have different directions. Therefore the probability that a created $\beta^+$-active nucleus contributes to the detected activity is very high. However, the number of replicas was so high that sometimes crashes of the simulation because of a overflow of the stack of secondary particles were observed.

To further improve the computing time the use of nuclear interaction length biasing was investigated. This biasing increases the number of inelastic interactions. The investigations showed that more $\beta^+$-active nuclei were created but also more computing time was needed. The balance was that about the same time is used to create one residual nucleus with nuclear interaction length biasing. From this behavior one can conclude that the computing time is dominated by simulating nuclear processes and not by simulating the transport. Therefore, nuclear interaction length biasing was not further used.

The remaining possibility to get faster runs was to force the annihilation photons in a wanted direction. FLUKA is able to do decay direction biasing which means the direction of a decay product is forced in a wanted direction. For a $\beta^+$-decay this can only be used to force the emitted positron in a wanted direction but it cannot be used to force the direction of the annihilation photons. Therefore the decay direction biasing was extended by Alfredo Ferrari to offer also the possibility to bias the direction of the annihilation photons. The principle of this new biasing is the following: when annihilation photons are created their directions are isotropically distributed. The biasing forces one photon in the direction to given point. To compensate for the unphysical direction change the photon gets a different weight according to the angle between the original direction and the forced direction. The other photon is emitted in the opposite direction with the same weight. After the assigning of the weight and the direction the photons are transported normally. The position on the upper detector head to which the first photon of the pair of annihilation photons is forced to point, was chosen randomly.

By using this biasing reasonable computing times were obtained. The number of replicas used in the RADDECAY option was reduced to 250 to avoid the stack overflows. The disadvantage of the decay direction biasing is that every photon has a different weight and cannot be put directly in the detection routine of the modified PETSIM code any more because only a integer number of pairs of annihilation photons can be put.

Also in the simulations performed to simulate the annihilation points the weights of the annihilation photons were changed by the use of the RADDECAY option to produce 500 replicas. Each residual nucleus got the weight 1/500 and also each of its decay products. Therefore, each annihilation photon had the same weight and could be treated by the conversion into listmod data the same way. The distribution of the weights by using the decay direction biasing is shown in figure 3.2. The distribution starts with weights of $4 \cdot 10^{-4}$ and the number af annihilation photons decreases with higher weights.
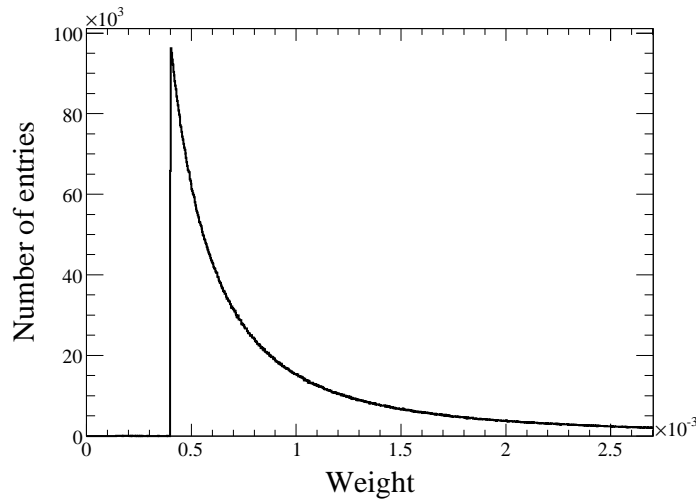
**Figure 3.2:** *Distribution of the weights.*

It was chosen to put the pairs of photons which have the lowest possible weight of $4 \cdot 10^{-4}$ one time and pairs with higher weights according to their weight value. How often a pair is put into the routine is calculated by taking the integer part of a division of its weight and the minimum weight $4 \cdot 10^{-4}$. The reminder of the division is further used to determine if the pair is put an additional time. This is done by a random choice where the probability of being chosen is the value of the reminder. For illustration an example is given: lets assume the weight of a given pair of annihilation photons is $9 \cdot 10^{-4}$ and the minimum weight $4 \cdot 10^{-4}$. The result of the division is 2.25, the integer part is 2 and the reminder is 0.25. A random number between 0 and 1 is calculated and if it is smaller than 0.25 the annihilation pair is put 3 times else 2 times.

By using this way list mode data can be created with the modified PETSIM code and the backprojection can be done by the same routines as in the experiment. Because only the distribution of the backprojection is compared and not the absolute value the use of annihilation pairs with different weights does not compromise the results.

The way the FLUKA output is stored was found to be not very practical for further data analysis therefore, a program was written which converts the data into a TTree and saves it in a file. A TTree is an C++ class, used in the data analysis framework ROOT, which is aimed to store large quantities of same class data sets. I is optimized to reduce disc space and enhance data access and it offers methods for evaluating and plotting subsets of the stored data [Bru00, ROO07] .

Compared to reading the FLUKA output directly big savings in time were obtained when analyzing residual nuclei distributions or when evaluating events occurring only in a given time interval. Additionally the the file sizes were smaller without loosing any information or

precision. In principle smaller file sizes could be obtained also by zipping the files but this has the disadvantage that before every further use the files have to be unzipped which is very time consuming for these big files. The PETSIM code was rewritten to read the data directly from the saved TTree.

## 3.3   Results and conclusions

Because of limitations in terms of computing time and disk space for the $^{16}$O experiments only the highest and lowest energies were simulated. Additionally the three carbon experiments were simulated. The water targets were modelled with 0.7 % carbon to be close to the experiment. Two additional simulations of $^{16}$O with 200 and 350 $A$MeV were done where the target was modelled as pure water without any carbon to investigate the contribution of the additional carbon. All water and gelatine targets were modelled with the standard ionization potential of 75 eV because in the previous simulations of the annihilation points it was found that 75 eV gives better results in terms of position of the activity peak. In the final simulations no crashes due to stack overflows or bugs were observed anymore.

**Resources**

Tables 3.5, 3.6 and 3.7 give an overview of the resources used in the final simulations. The same alphanumeric identifiers as in chapter 2 are used to identify the experiment. The first three characters and numbers and digits give the nuclide of the beam, the fourth character identifies the target (PMMA, water or graphite) and the last three numbers give the energy of the beam in $A$MeV. For each simulation $3 \cdot 10^6$ to $4 \cdot 10^6$ primaries were simulated. Usually 10 parallel runs of 30 to 40 cycles with $10^4$ primaries each were performed. In some cases not all cycles could be finished. This was either due to limits in disk space (quota) or because the simulations exceeded the time limit of the queue. Because the disk space was needed for the next simulations the remaining jobs were not submitted again.

**Table 3.5:** *Overview of the resources used for the simulations without BME.*

| ID | number of primaries | size output [GB] | size ROOT files [GB] | average time [h] /$10^6$ IP | annihilation events /$10^6$ IP |
|---|---|---|---|---|---|
| O16P350 | $3.00 \cdot 10^6$ | 8.5 | 5.7 | 27 | 168907 |
| O16W350 | $3.00 \cdot 10^6$ | 6.6 | 4.4 | 20 | 103694 |
| O16G350 | $3.00 \cdot 10^6$ | 9.9 | 6.7 | 28 | 157283 |
| O16P200 | $4.00 \cdot 10^6$ | 3.0 | 2.0 | 8 | 34397 |
| O16G200 | $4.00 \cdot 10^6$ | 3.1 | 2.1 | 13 | 36008 |
| O16W200 | $4.00 \cdot 10^6$ | 2.7 | 1.8 | 8 | 31329 |
| C12P260 | $2.94 \cdot 10^6$ | 3.8 | 2.6 | 12 | 61114 |
| C12W260 | $3.00 \cdot 10^6$ | 3.8 | 2.6 | 13 | 60011 |
| C12G260 | $3.00 \cdot 10^6$ | 5.8 | 3.3 | – | 77232 |

The size of the binary output of FLUKA varies from 2.7 to 13.0 GB. By converting this output into ROOT files which hold the data as TTree, the size could be reduced by about one third. The size of the output files is directly connected to the number of produced annihilation events. The simulation of experiment O16G350 produced the most annihilation events O16W350 the

fewest. A comparison between the simulations with and without BME show that in general more events are produced when BME is used. The only exception is the experiment O16G350. Because this numbers do not take into account the weights one cannot conclude if the simulation predicts more annihilations.

The simulations aimed to investigate the contribution of the additional carbon by adding gelatine to the water show no significant difference in the number of annihilation events. The computing time used for the simulations of $10^6$ primaries is varying from 7 to 27 hours. The simulations of the experiments with higher energies needed much more computing time than those with lower energies. For some simulations the average computing time cannot be given because the original files were deleted by mistake after the conversion into the ROOT files, before the duration of the simulation was checked.

The CPU time of a simulation depends, as already mentioned before, on the nodes where it is performed. This explains that for example in the simulation without BME the simulation of the experiment O16P350 needed 27 hours and the simulation of O16W350 only 20 but in the simulations using BME the O16P350 was finished after 25 hours and O16W350 needed 27.5 hours. Therefore, the average CPU time per $10^6$ incident particles gives only a rough idea about the time needed.
However, these values show the success of the introduced biasing. The simulation with the longest duration was O16W350 with BME which needed a total time for all $4 \cdot 10^6$ primaries of about 110 hours. Compared to the first tries of simulating annihilation photons which needed about 100 days of CPU time, this is a huge gain.

**Table 3.6:** *As table 3.5 but BME was used.*

| ID | number of primaries | size output [GB] | size ROOT files [GB] | average time [h] /$10^6$ IP | annihilation events /$10^6$ IP |
|---|---|---|---|---|---|
| O16P350 | $3.78 \cdot 10^6$ | 11.0 | 7.3 | 25 | 167542 |
| O16W350 | $4.00 \cdot 10^6$ | 9.0 | 6.0 | 27.5 | 106618 |
| O16G350 | $3.65 \cdot 10^6$ | 13.0 | 8.3 | – | 171970 |
| O16P200 | $4.00 \cdot 10^6$ | 3.5 | 2.4 | 12 | 41010 |
| O16G200 | $4.00 \cdot 10^6$ | 3.5 | 2.4 | 10 | 40713 |
| O16W200 | $4.00 \cdot 10^6$ | 3.2 | 2.2 | 7 | 37320 |
| C12P260 | $4.00 \cdot 10^6$ | 5.5 | 3.7 | 18 | 64140 |
| C12W260 | $4.00 \cdot 10^6$ | 5.4 | 3.6 | 18 | 64339 |
| C12G260 | $3.67 \cdot 10^6$ | 6.2 | 4.2 | – | 79664 |

**Table 3.7:** *Simulations of a $^{16}O$ beam of 350 AMeV and a $^{12}C$ beam of 260 AMeV on water targets. The targets material was modelled one time as pure water and one time with 0.7 % carbon added. BME was used.*

| ID | number of primaries | size output [GB] | size ROOT files [GB] | average time [h] /$10^6$ IP | annihilation events /$10^6$ IP |
|---|---|---|---|---|---|
| O16W350 | $3.00 \cdot 10^6$ | 6.8 | 4.5 | 23 | 106195 |
| C12W260 | $3.00 \cdot 10^6$ | 4.1 | 2.8 | 15 | 63779 |

### 3.3.1 Backprojections

The backprojections of the simulations of the $^{12}C$ beams with 260 AMeV are shown in figure 3.3. The targets are, from top to bottom, PMMA, water and graphite. The pictures on the left show the backprojection during spill breaks and the pictures on the right show the backprojection from 10 to 20 minutes after irradiation end. The experimental backprojections are shown in black, the simulations with BME in blue and the simulations without BME are shown in red. The experimental distribution is normalized to its maximum, the simulations are normalized to the area of the experimental distribution.

For all distributions shown in figure 3.3 a good agreement between the shape of the entrance part i.e. about the first centimeter is obtained. Like in the backprojection obtained in the experiments also in the backprojection of the simulation activity was found outside of the target due to an artifact of the backprojection. The plateau region of the backprojections obtained during the spill pauses shows a similar slope as already found in the investigations of the annihilation points. For the two other targets this was not found. Different than in the previous simulations of the annihilation points it is clear now that the slope can arise only from the simulation itself because the processing of the data was done the same way for experiment and simulation.

The tails are well reproduced in all the simulation in both backprojections. The position and shape of the peaks is well reproduced, the highest difference is found for carbon but the reason for that finding can be simply due to small uncertainties in the density of the target. It can be seen that the use of BME reproduces the position of the peak better. This effect is best visable for the backprojections obtained during the spill pauses. The reason for the better agreement is that in the simulations performed with BME additional activity is produced at depths corresponding to primary energies below 100 AMeV as can be seen in figure 3.3 for water target for the backprojection performed during irradiation.

From the backprojections obtains after irradiation end it can be seen that the simulated peaks are too high but the peaks from the simulation including BME are better reproduced. In front of the peak a small decrease of the activity can be seen. The reason for this finding was identified as the transition between RQMD and BME. BME, as presently implemented, is

known to underestimate the production of nuclei close in charge and mass to the interacting ions [Cer07]. This means for instance that in case of water the predicted yield of $^{15}$O as a target fragment is significantly less than the real one. Since the activity during the irradiation at the considered depth is mainly due to $^{15}$O target fragments, one can understand the pronounced gap shown in figure 3.3 for the case of the water target backprojected during the spill pauses. On the other hand looking at the activity profile after the irradiation (figure 3.3, water target, backprojected after irradiation end), substantially due to $^{11}$C fragments, the gap dissappears.

Figures 3.4 and 3.5 show the simulations of the $^{16}$O beams with 350 and 200 $A$MeV, respectively. The same colors as in figure 3.3 are used. For the simulations of the 350 $A$MeV beam a good agreement in the entrance region was obtained. Different from the simulations of the carbon beams, the plateau region is well produced during the spill breaks but not as good after irradiation end. An overestimation of the activity is found in the plateau region of backprojections obtained from 10 minutes to 20 minutes after irradiation end. This finding can be due to a too low peak which pushes up the plateau when a normalization to the same area as in the experiment is applied. Like in the simulations of the activity created by $^{12}$C beams too few activity is found just before the peak because of the underestimation of the production of $\beta^+$-emitters by BME. For the backprojections during the spill breaks the activity peak obtained by the use of BME is slightly smaller than without BME but in both cases much too high compared to the experiment. After irradiation end the simulation with BME shows better agreement in the peak for the PMMA and graphite target but for the water target the agreement is worse by using BME.

The simulations of the 200 $A$MeV $^{16}$O beams are shown in figure 3.5. For this low energy BME has the biggest effect because less primaries can interact before they reach 100 $A$MeV and therefore, the relative number of particles treated by BME is higher than in the simulations with the 350 $A$MeV beam. Apart from the backprojection of the simulation with the graphite target after irradiation end, a good agreement in the entrance region is found. During the spill pauses the plateau region, the position and width of the peak and the tail are good reproduced. As in the previous discussed simulations in front of the peak a underestimation of the activity was found due to the underestimated production of $\beta^+$-active nuclei by BME. The peak is too pronounced. For the backprojections obtained after irradiation end the agreement is not very good because the $^{15}$O projectile fragments which were dominating the activity during irradiation, are already decayed and the peak to plateau ratio is lower. Therefore also the gap between the two simulation modells is more pronounced. For the graphite target one can see two peaks of the same height in the simulation without BME (cf. 3.5 bottom, right). It can also be seen that the use of BME improves the simulations by pushing the peak up and the plateau down. Also the position of the peak improves because due to the additional activity produced by BME the beak moves in upstream direction.

**Figure 3.3:** *Backprojections of simulations of $^{12}C$ beams with 260 AMeV on PMMA, water and graphite. The black lines give the experimental activity distributions, the red lines* FLUKA *and the blue ones* FLUKA *with BME included. On the left side backprojections of the annihilations during the pauses of the spills are shown, the right side shows backprojections from 10 to 20 minutes after irradiation end.*
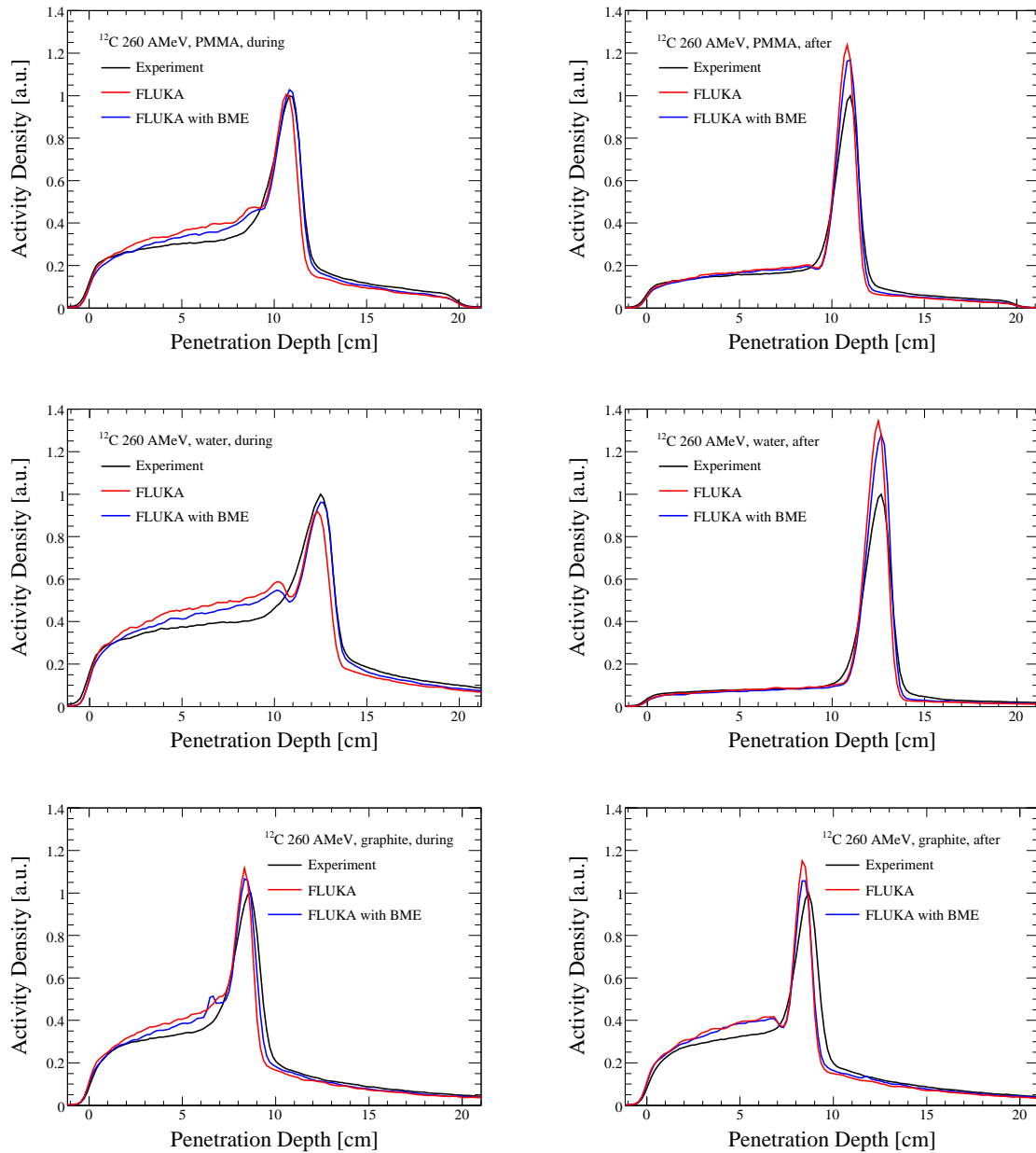
**Figure 3.4:** *Backprojections of simulations of $^{16}O$ beams with 350 AMeV on PMMA, water and graphite. The black lines give the experimental activity distributions, the red lines FLUKA and the blue ones FLUKA with BME included. On the left side backprojections of the annihilations during the pauses of the spills are shown, the right side shows backprojections from 10 to 20 minutes after irradiation end.*
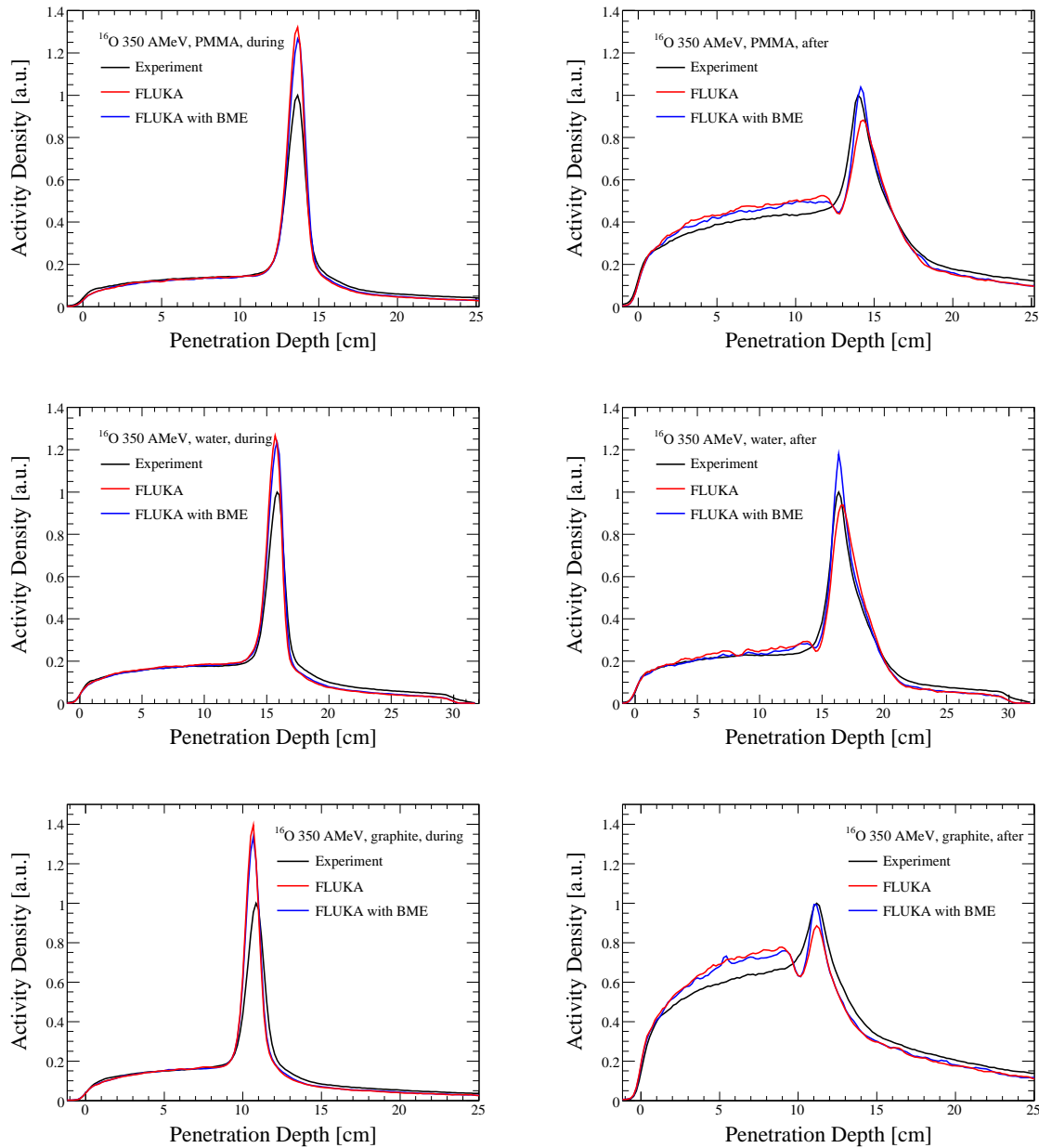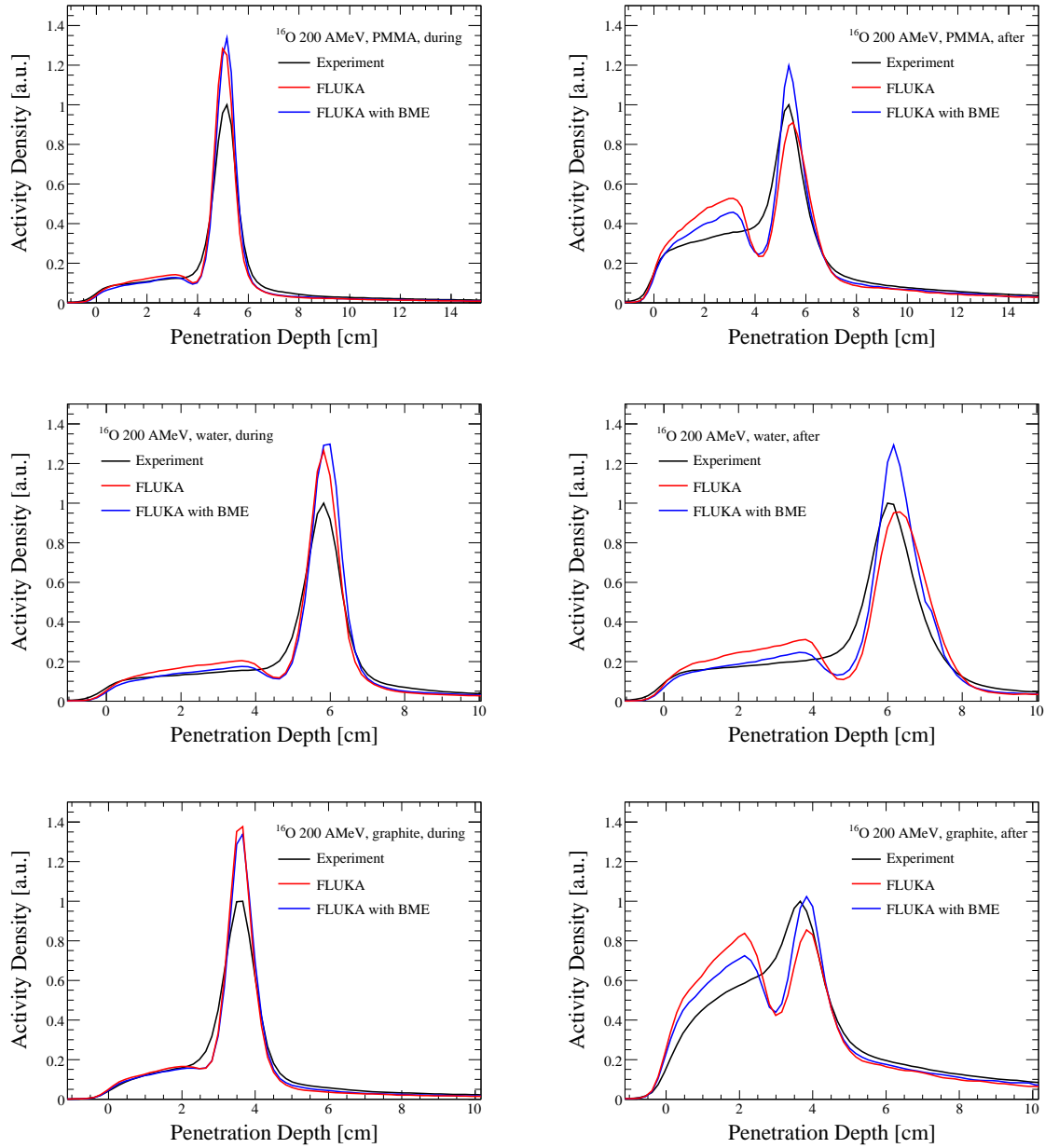
**Figure 3.5:** *As figure 3.4 but with a $^{16}O$ beam of 200 AMeV.*

### 3.3.2 Peak plateau and peak shift

**Table 3.8:** *Shift of the position of the $\beta^+$-activity peak between backprojections made during the spill breaks and from 10 to 20 minutes after irradiation end. Only the simulations with BME were used. The position of the peak was obtained by a Gauss fit.*

| ID | Peak position during [cm] | Peak position after [cm] | difference [cm] |
|----|---------------------------|--------------------------|-----------------|
| O16P350 | 13.64 | 14.19 | 0.55 |
| O16W350 | 15.76 | 16.37 | 0.61 |
| O16G350 | 10.63 | 11.13 | 0.50 |
| O16P200 | 5.11 | 5.36 | 0.25 |
| O16G200 | 3.60 | 3.84 | 0.24 |
| O16W200 | 5.89 | 6.19 | 0.30 |
| C12P260 | 10.82 | 10.88 | 0.06 |
| C12W260 | 12.57 | 12.62 | 0.05 |
| C12G260 | 8.42 | 8.42 | 0.00 |

Like in the experiments a shift of the peak between the backprojection done during the spill breaks and from 10 to 20 minutes after irradiation end could be found. Only the simulations with BME were used because they reproduce the peak position better (cf. discussion in section 3.3.1).

The experimental values are given in table 2.6, the positions found in the simulations are shown in table 3.8. About 10 to 20 % larger shifts are found in the simulations compared to the experiment. The only exception is the experiment C12G260 where the simulation predicts no shift of the peak.

### 3.3.3 Distribution of $\beta^+$-active residual nuclei

In the same simulations performed for the backprojections the residual $\beta^+$-active nuclei were scored. While the backprojections give the distribution of the activity of all $\beta^+$-active nuclides decaying in a certain time window, the distribution of the residual nuclei can give a deeper insight in the spatial contribution of each nucleus.

However, the distribution of the residuals is obtained in a different way than the backprojected activity and looks therefore slightly different. Because the depth in the target where the annihilation takes place is not known, the backprojection projects the whole activity into the central plane and due to the double head geometry it is also stretched along the detector heads. The backprojections shown in the previous chapter were obtained by summing over the central $\pm$ 5 voxels with respect to the beam.

For the residual nuclei distributions shown in figures 3.6, 3.7 and 3.8 the sum of the activity over the whole width of the target was taken into account.

Figures 3.6, 3.7 and 3.8 show the distribution of $\beta^+$-active nuclei for the simulations of the $^{12}$C beams with 260 $A$MeV, $^{16}$O with 350 $A$MeV and $^{16}$O with 200 $A$MeV, respectively. In each figure the pictures on the left show FLUKA simulations without BME, the pictures on the right show the simulations with BME. The green lines shows $^{13}$N, $^{15}$O is shown in magenta, $^{10}$C is shown in blue, and $^{11}$C in red. The black line is the sum over all $\beta^+$-active residual nuclei including also $^9$C, $^8$B, $^{12}$N, $^{14}$O and $^{13}$O. The distributions are normalized to $10^6$ incident particles.

For the simulation of the 260 $A$MeV $^{12}$C beam shown in figure 3.6, it can be seen that the amount of $^{13}$N is almost negligible for all targets. Only for the water target a small amount is found. In the simulation of the water target, done with BME, compared to the simulation without BME an additional amount of $^{13}$N is found at the distal end of the peak. A little bit more $^{10}$C than $^{13}$N is produced in all targets, mainly in the peak. Also for this nuclide the simulation including BME predicts a slightly higher amount than the simulations without BME.
$^{15}$O is not found in the irradiation of graphite which can be explained by the absence of $^{16}$O in the target. For the other two targets it is produced increasingly with increasing depth until the energy of the primaries drops below 100 $A$MeV. From there on it decreases apart from a small rise at the distal end of the peak in the BME simulations.
$^{11}$C is the most abundant nucleus for all targets due to projectile fragmentation. It is also the main responsible nucleus for the peak. For the simulations of the PMMA and graphite targets the distribution shows a small gap just before the peak. The reason for that finding is the transition between the RQMD and BME model, as already discussed for the backprojections.

Figure 3.7 shows the residual nuclei for the simulations with the 350 $A$MeV $^{16}$O beams. $^{13}$N contributes mainly as projectile fragments which are created at higher energies and therefore, no difference between the simulations with and without BME is visible. The distribution of $^{10}$C is similar as the distribution of $^{13}$N. It contributes only to the peak due to projectile fragmentation, except for the graphite target where $^{10}$C target fragments are created because of the high amount of $^{12}$C in the target.
The contribution of $^{15}$O in case of the graphite target is exclusively in the peak because of the absence of $^{16}$O in the target. For the other targets $^{15}$O contributes also as target fragment. Lower peaks are found for the simulations performed with BME compared to the simulations done without BME. The reason for that finding is that by using the BME modell $^{15}$O nuclides, which are produced by RQMD at higher energies can undergo a further inelastic nuclear interaction treated by BME and do not contribute to the $^{15}$O distribution any more. A similar decrease in the height of the peak was found for the PMMA and water target for the same reason.
A low contribution of $^{11}$C target fragments was found for the water targets. $^{11}$C projectile fragments are found after the $^{15}$O peak. The reason is the following: when a $^{15}$O projectile fragment is created from $^{16}$O, the remaining path of $^{15}$O is about $\frac{15}{16}$ of the range of the primary $^{16}$O due to the difference in the $A/Z^2$ ratio between $^{16}$O and $^{15}$O. If the primary $^{16}$O particle fragments into $^{11}$C, the path of this nuclei is about $\frac{11}{9}$ of the remaining path of the $^{16}$O. Therefore $^{11}$C projectile fragments travels further than $^{15}$O fragments in case of an $^{16}$O

beam. An additional contribution of $^{11}$C is found for all targets for the simulations done with
BME compared to the simulations done without BME.

Figure 3.8 shows the residual nuclei distributions for the simulations of $^{16}$O beams with 200
$A$MeV. Like in the simulation with the 350 $A$MeV $^{16}$O beam the contribution of $^{13}$N and
$^{10}$C is small and the use of BME increases the abundance a little bit. In the simulation of
the graphite target the use of BME decreases the $^{15}$O peak like it was already found for the
simulations of the 350 $A$MeV $^{16}$O beam. For the other targets the use of BME leads to more
$^{15}$O in the peak because BME produces additional $^{15}$O. In the 350 $A$MeV experiment this
could not be seen because the amount of additional $^{15}$O produced by BME is relatively low
compared to the amount of $^{15}$O produced by RQMD. The most visible influence of BME in
these simulations is the production of $^{11}$C projectile fragments. For PMMA and water targets
a significant increase of the peak due to $^{11}$C was found.

Looking at the $^{11}$C distribution obtained with the simulation without BME of the graphite
target (cf. figure 3.8, bottom left panel) at about 2.7 centimeters depth, one can see a sharp
fall off which is due to the fact that below 100 $A$MeV nucleus-nucleus interactions are not per-
formed and so the production of $^{11}$C target fragments goes to zero. The corresponding plot
including the BME event generator does not show a reduction of the discontinuity. This indi-
cates once more that the yield of $^{11}$C from $^{12}$C target fragmentation is heavily underestimated.

As in the simulation of the $^{11}$C beam with 260 $A$MeV a gap in the residual nuclei distribution
just before the peak was found due to the transition between RQMD and BME. Because of
the low energy of 200 $A$MeV of the primary beam the gap is very pronounced. It can be seen
that the nuclei responsible for the gap are $^{11}$C and $^{16}$O originating from target fragmentation.
The depth of the gap indicates that BME produces much too few of these nuclei.
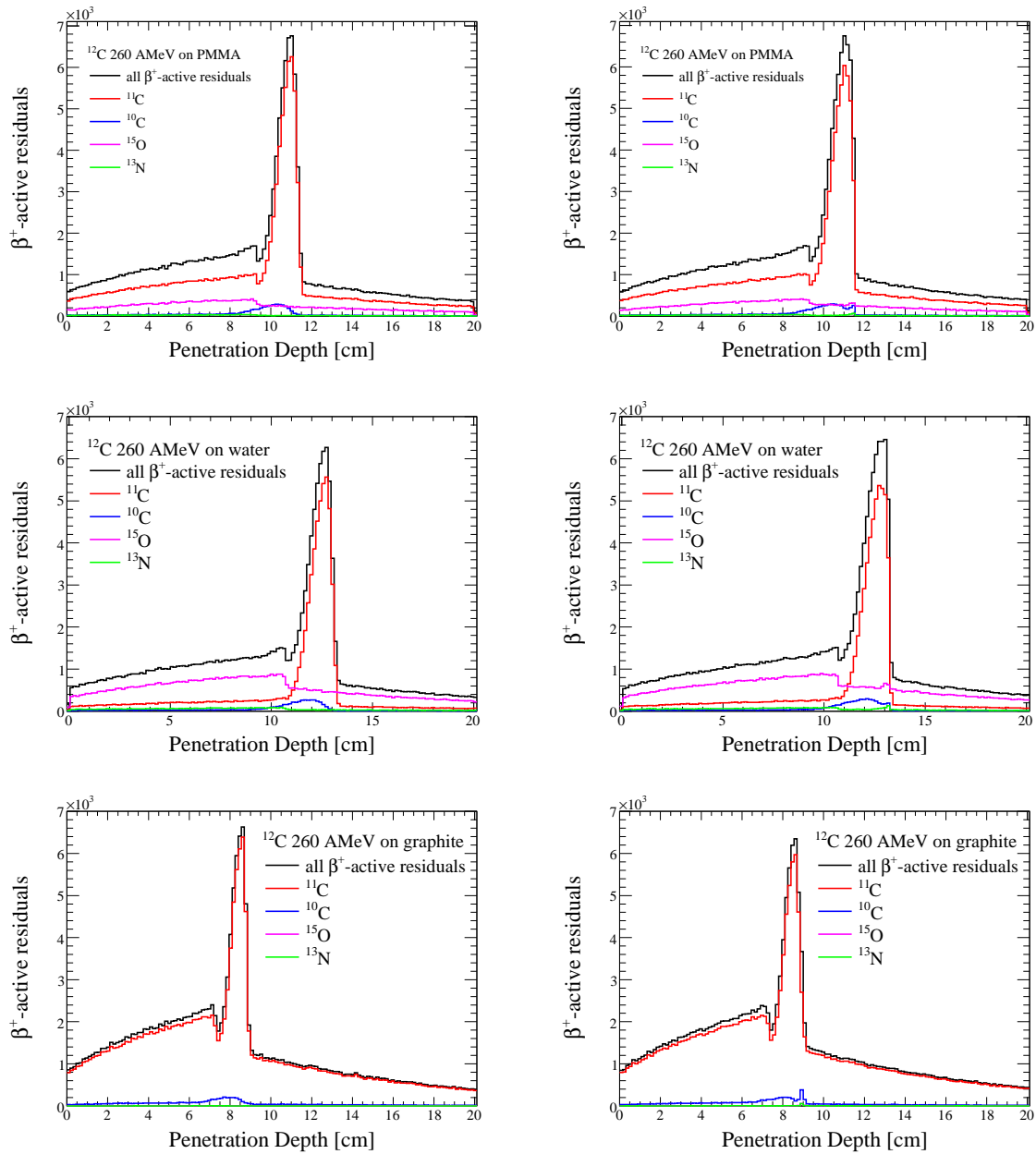
**Figure 3.6:** *Distribution of $\beta^+$-active residual nuclei produced by a $^{12}C$ beam of 260 AMeV on targets of PMMA, water and graphite. The pictures on the left side show* FLUKA *simulations without BME, the pictures on the right show simulations with BME. The distributions are normalized to $10^6$ incident particles. The green lines shows $^{13}N$, $^{15}O$ is shown in magenta, $^{10}C$ is shown in blue, and $^{11}C$ in red. The black line is the sum over all $\beta^+$-active residual nuclei including also $^9C$, $^8B$, $^{12}N$, $^{14}O$ and $^{13}O$.*
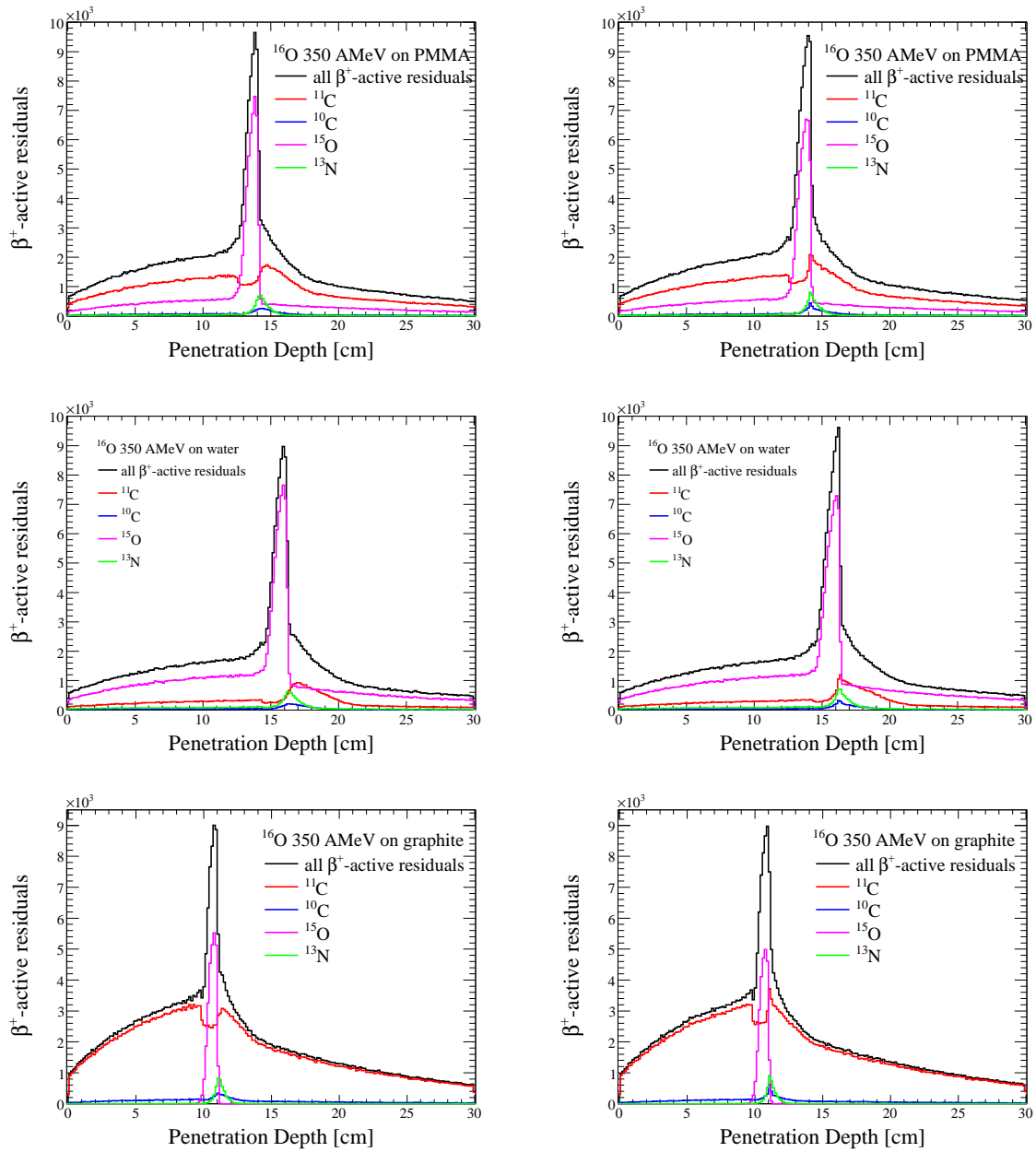
**Figure 3.7:** *As figure 3.6 but with a $^{16}O$ beam of 350 AMeV.*
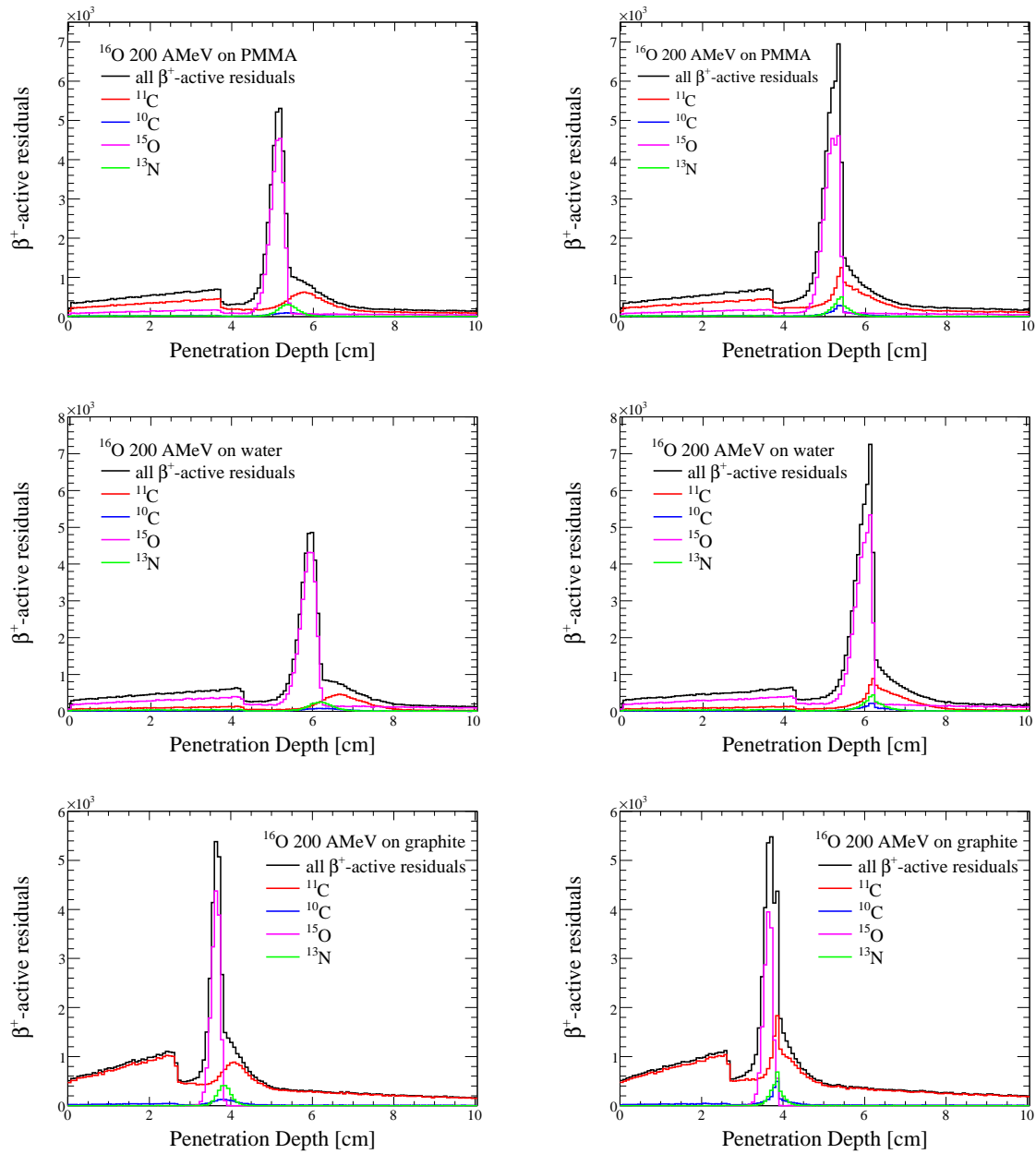
**Figure 3.8:** *As figure 3.6 but with a $^{16}O$ beam of 200 AMeV.*

### 3.3.4   Total amount of $\beta^+$-active residual nuclei

The total amount of different residual nuclei produced in simulations without BME is shown in table 3.9. Table 3.10 shows the total amount of residual nuclei produced in simulations with BME. The production of residuals is normalized to $10^6$ incident particles. The last column gives the total of all residual nuclei found in the simulation, including also $^{12}$N and $^{13}$O which are not shown in the tables 3.9 and 3.10. In the simulations also $^{14}$O, $^9$C and $^8$B were found which are not accessible in the experimental investigations. $^{13}$N was found for all simulations, in the experiment it could be only found for $^{16}$O beams.

**Table 3.9:** *Simulated production of $\beta^+$-active nuclei by $10^6$ incident particles. The total value includes also other $\beta^+$-active nuclei like $^{13}$O and $^{12}$N. The simulation was done without BME. The origin of the $^{13}$N in experiment C12G260 are (p,n) reactions on $^{13}$C.*

| ID | $^{11}$C | $^{10}$C | $^9$C | $^{15}$O | $^{14}$O | $^{13}$N | $^8$B | total |
|---|---|---|---|---|---|---|---|---|
| O16P350 | 187958 | 11603 | 1162 | 117715 | 8480 | 10298 | 6871 | 346058 |
| O16W350 | 53071 | 7742 | 1303 | 195410 | 13165 | 16124 | 5782 | 294303 |
| O16G350 | 342332 | 16108 | 1084 | 27874 | 1942 | 4458 | 8237 | 404300 |
| O16P200 | 41151 | 2794 | 382 | 38506 | 2446 | 3640 | 2092 | 91553 |
| O16W200 | 16516 | 2320 | 448 | 59452 | 3464 | 5174 | 1923 | 89774 |
| O16G200 | 67323 | 3276 | 332 | 15878 | 931 | 2369 | 2403 | 93097 |
| C12P260 | 113426 | 6536 | 443 | 30864 | 1413 | 2462 | 3454 | 159400 |
| C12W260 | 66296 | 6253 | 657 | 81180 | 3757 | 6718 | 3579 | 169254 |
| C12G260 | 186350 | 7266 | 287 | 0 | 0 | 46 | 4026 | 198890 |

**Table 3.10:** *As table 3.9 but the simulations were done with BME. The small amounts of nuclei $^{15}$O, $^{14}$O and $^{13}$N found in the C12G260 experiment are due to fusion processes implemented in BME.*

| ID | $^{11}$C | $^{10}$C | $^9$C | $^{15}$O | $^{14}$O | $^{13}$N | $^8$B | total |
|---|---|---|---|---|---|---|---|---|
| O16P350 | 193648 | 12131 | 1372 | 118510 | 8556 | 10466 | 7864 | 354825 |
| O16W350 | 55831 | 8216 | 1570 | 198791 | 13436 | 16469 | 6701 | 303122 |
| O16G350 | 350262 | 16496 | 1328 | 25760 | 1902 | 4250 | 9356 | 411844 |
| O16P200 | 48445 | 3657 | 731 | 43836 | 2725 | 4149 | 3393 | 107960 |
| O16W200 | 21077 | 3200 | 797 | 69073 | 4031 | 6053 | 3139 | 108551 |
| O16G200 | 76967 | 4190 | 760 | 14954 | 1099 | 2544 | 3885 | 105403 |
| C12P260 | 117686 | 7219 | 713 | 32270 | 1498 | 2686 | 4515 | 167638 |
| C12W260 | 70218 | 7111 | 987 | 85969 | 3930 | 7212 | 4753 | 181428 |
| C12G260 | 192191 | 7966 | 597 | 89 | 29 | 137 | 5134 | 207203 |

In general more residual nuclei of each isotope are produced when BME is used. This is obvious because BME produces additional $\beta^+$-active nuclei in interactions of particles which have energies below the RQMD threshold. However, for the simulations of the irradiation of graphite with the $^{16}$O beam of 200 $A$MeV a lower amount of $^{15}$O is predicted when BME is used. Because the target contains only carbon $^{15}$O arises only from projectile fragmentation and are therefore, produced at higher energies with RQMD. If BME is used these fragments can undergo an additional inelastic nuclear interaction and therefore, their total amount is lowered.

In the following the experimental production of $\beta^+$-active nuclei (cf. tables 2.4 and 2.5) is compared only with the simulations using BME.

For the $^{16}$O beams only the production of $^{15}$O in the experiment with 350 $A$MeV on PMMA and water agrees with the experimental production within a few percent. $^{16}$O is produced mainly at higher energies therefore, this agreement is due to the RQMD model. I case of the $^{12}$C beams the production of $^{15}$O in simulations with the PMMA and water targets is reasonable produced. BME contributes significantly to the production in this case as can be seen by a comparison of the $^{12}$C of simulation C12P260 and C12W260 in tables 3.9 and 3.10. The only nuclide which is produced with a too high amount is $^{10}$C in the simulation of $^{12}$C on water, all other productions are too low compared to the experiment. The simulated production rates are up to a factor of two too low.

### 3.3.5 Influence of the gelatine added

Two further simulations were performed to investigate the influence of the gelatine added to the water. Figures 3.9 and 3.10 show backprojected $\beta^+$-activity distributions of simulations of an $^{16}$O beam of 350 $A$MeV and a $^{12}$C beam of 260 $A$MeV on water, respectively. In the simulations which are shown by the red circles the target is modelled as gelatine ($H_{66.2}O_{33.1}C_{0.7}$), in the simulations shown by blue triangles the target is modelled as $H_2O$. The figure on the left shows a backprojection during the pauses between the spills, the figure on the right shows a backprojection from 10 to 20 minutes after irradiation end. Within the statistical fluctuations no difference in the shape of the curves due to the additional water was found.
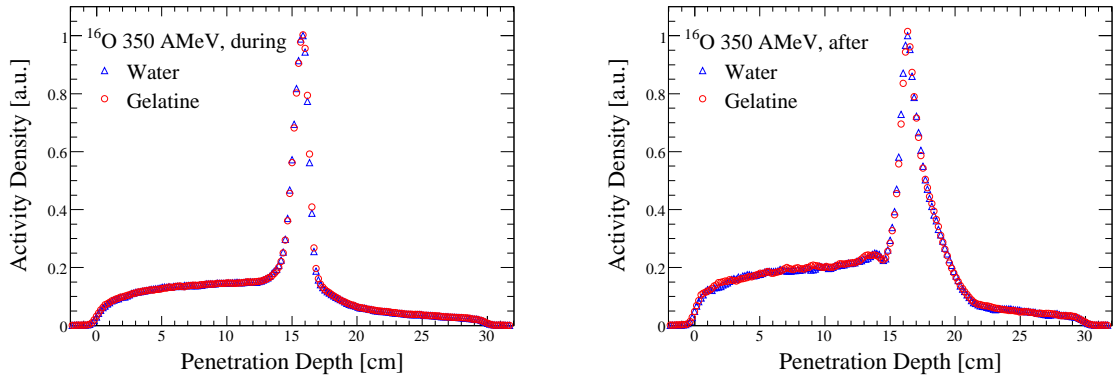


**Figure 3.9:** *Comparison between backprojections of two two simulations where in one the target is modelled as pure water in the other the target contains additionally 0.7 % carbon. The beam is $^{16}$O with 350 $A$MeV. The left figure shows a backprojection of the simulation during irradiation, the right figure a backprojection from 10 to 20 minutes after irradiation end. Both figures are normalized to the same area.*

**Table 3.11:** *Comparison between the total amount of different $\beta^+$-active residual nuclei produced for simulations which model the target as pure water or as gelatine. The total amounts are normalized to $10^6$ incident particles.*

| ID | material | $^{11}$C | $^{10}$C | $^9$C | $^{15}$O | $^{14}$O | $^{13}$N | $^8$B | total |
|---|---|---|---|---|---|---|---|---|---|
| O16W350 | gelatine | 55926 | 8230 | 1571 | 198901 | 13454 | 16709 | 6708 | 303763 |
| O16W350 | water | 53806 | 8184 | 1590 | 201084 | 13392 | 16824 | 6705 | 303857 |
| C12W260 | gelatine | 70262 | 7117 | 988 | 86014 | 3938 | 7336 | 4756 | 181738 |
| C12W260 | water | 69224 | 7200 | 1026 | 87269 | 4023 | 7440 | 4731 | 182297 |

Table 3.11 shows the total number of $\beta^+$-active nuclei obtained in the before mentioned simulations. The production is normalized to $10^6$ incident particles. For the 350 $A$MeV $^{16}$O beam
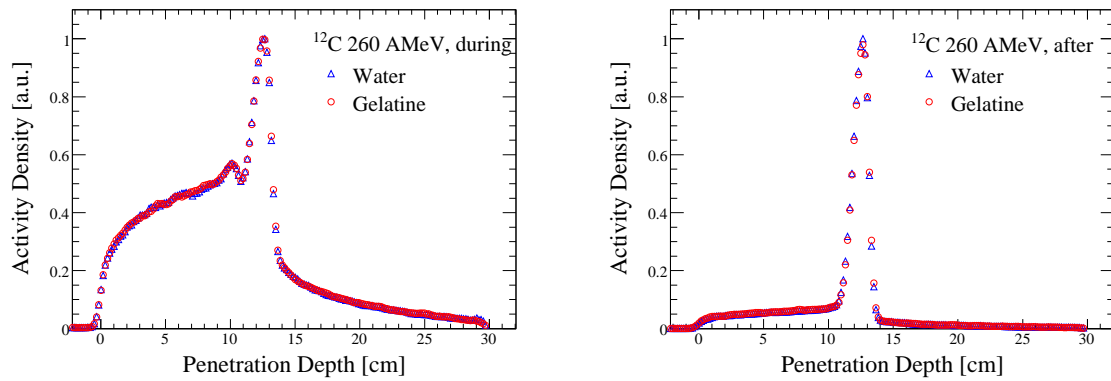
**Figure 3.10:** *As figure 3.9 but the beam is $^{12}C$ with 260 AMeV.*

all nuclides were found within 1 % difference in both simulations, except $^{11}$C which was found to be about 4 % higher in the simulation were the target contains also $^{12}$C. For the 260 $A$MeV $^{12}$C beam about 1.5 % more $^{11}$C was found. The amount of $^{8}$B is almost the same. The other nuclei showed an up to 4 % lower amount compared to the simulation where the target was modeled as pure water.

From the backprojections and the amount of the $\beta^+$-active residual nuclei one can conclude that the influence of the added carbon due to the gelatine is negligible.

### 3.3.6   $\beta^+$-activity build up and decay

From the simulations described before it is possible to obtain count rates showing the activity increase during the irradiation and the decay after the irradiation, like it was done in for the experiment (cf. figure 2.5). For the experiment the build up could be given only by the average production rates which could be obtained only for the three most abundant $\beta^+$-active nuclei (two in case of $^{12}$C on graphite). In the simulation it is possible to identify the build up and decay of all $\beta^+$active nuclei independent of their abundance. Therefore also the interruption of the build up due to interruptions of the irradiation can be shown.
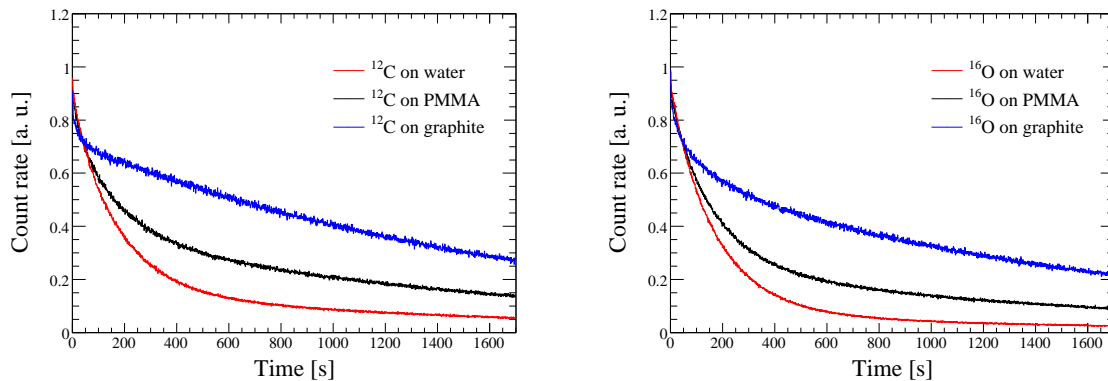


**Figure 3.11:**  *Comparison between simulated count rates in PMMA, water and graphite after irradiation end. The left picture shows the activity produced by 260 AMeV $^{12}$C beams, the right picture shows the activity produced by 350 AMeV $^{16}$O beams. The simulations were done with BME.*

Figure 3.12 shows the build up and decay of the count rates by the individual $\beta^+$-active nuclei. The most abundant $\beta^+$-active residual nuclei are shown in various colors explained in the legend of each picture. The total count rate is shown in black. It includes also other $\beta^+$-active nuclei like $^8$B, $^9$C and $^{12}$N. The simulations were done by using BME and the count rates are normalized to $10^6$ incident particles. The time structure of the irradiation is modelled as in the experiment including also the interruptions of the irradiation. This can be seen best in the irradiation of the two graphite phantoms where interruptions in the first 100 seconds occurred.

In the experimental investigations a comparison between the count rates of the decay curves in various targets was done (cf. figure 2.6). The same could be done with the simulations. In the experiment the decay curves of $^{16}$O with 300 AMeV and $^{12}$C with 260 AMeV were used to compare experiments of about the same particle range. Simulations with $^{16}$O beams of 300 AMeV were not performed therefore, the the decay curves in 3.11 show a comparison between 350 AMeV $^{16}$O beams and 260 AMeV $^{12}$C beams.
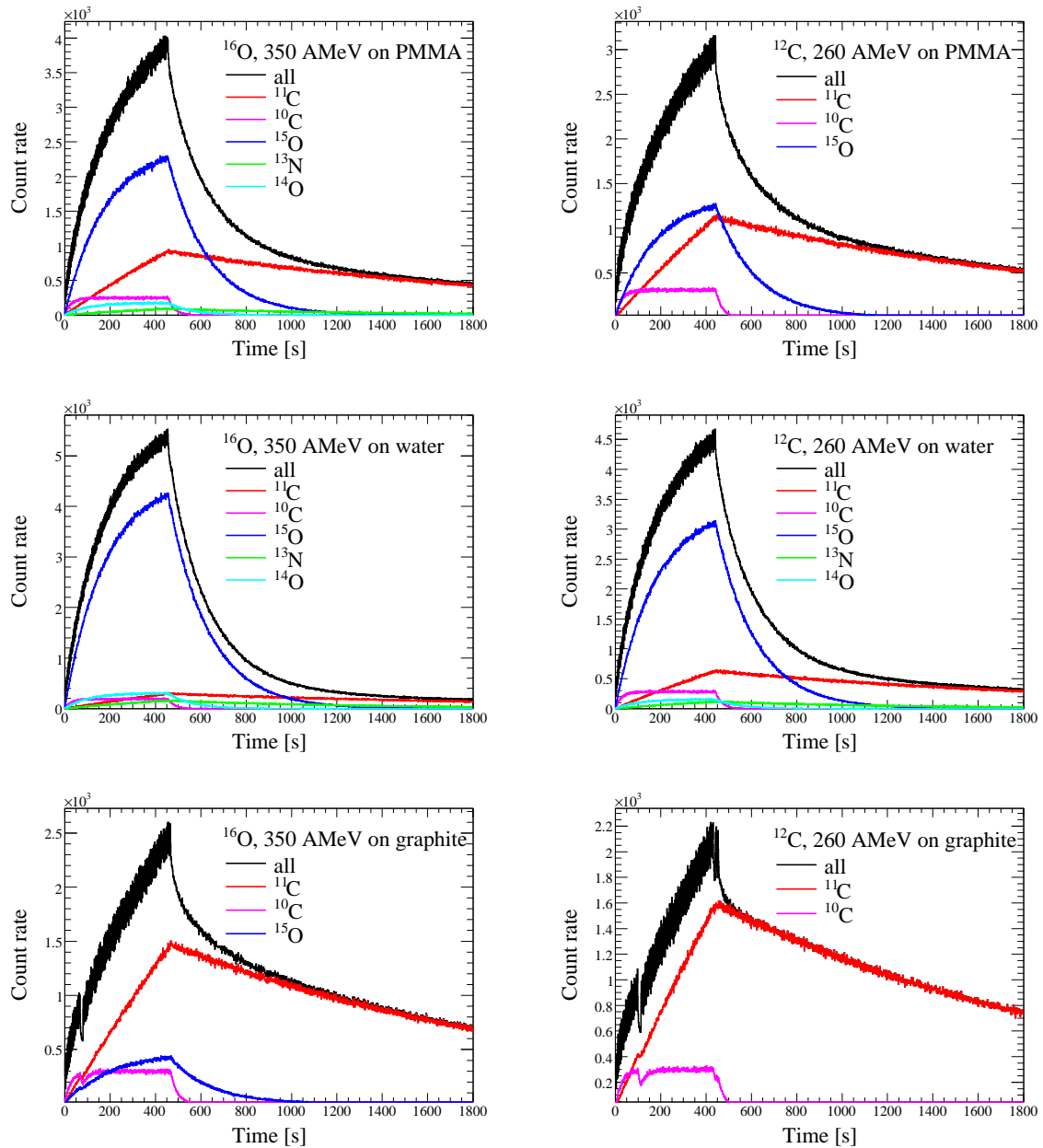
**Figure 3.12:** *Comparison between simulated and calculated count rates for $^{16}O$ beams of 350 AMeV (left) and $^{12}C$ beams of 260 AMeV (right). All figures are normalized to $10^6$ incident particles. The simulations were done with BME. The total count rates, indicated with "all", include also other $\beta^+$-active nuclei like $^8B$, $^9C$ and $^{12}N$. The irradiation stops between 400 and 500 seconds. The build up is shown during the spills and also during the breaks between the spills. The interruptions of the simulations were also simulated.*

A comparison between the decay curves of the simulation of the $^{12}$C beams and the experimental decay curve of the $^{12}$C beams (cf. figure 2.6) show a fair good agreement for the graphite target. This could not be expected because the ratio between the amounts of the $\beta^+$-active residual nuclei found in the simulation is different than in the experiment (cf. tables 3.9 and 2.4). For the other targets the simulated decay curves are too low. A disagreement could be expected because the ratio of the amount of $\beta^+$-active residual nuclei found in the simulation does not match the experimental finding.

The simulations with the $^{16}$O beams also no good agreement was found due to the same reasons. Additionally there simulations were done for the 350 $A$MeV beam while the experimental decay curves are shown for 300 $A$MeV which introduces a further error.

# Chapter 4

# Summary and Conclusions

The objective of this work was to investigate the feasibility of the FLUKA particle transport and interaction code to be used for in-beam PET monitoring of a therapy with $^{12}$C and $^{16}$O beams. In-beam PET measurements of the $\beta^+$-activity created by $^{16}$O beams on homogeneous targets were performed for the first time. The experimental data was used to benchmark FLUKA and its recently added model for low energy inelastic nuclear interactions, BME. The presented work consists of two main parts, the first dedicated to perform and analyze the experiments and the second to simulate the experiments.

## Experiments

The experiments were performed with the in-beam PET installed at the treatment place in the experimental $^{12}$C therapy facility at Gesellschaft für Schwerionenforschung (GSI), Darmstadt, Germany. Targets of PMMA, water and graphite were irradiated with $^{16}$O beams of 200, 250, 300 and 350 $A$MeV. The production of $\beta^+$-active nuclei in the targets was investigated quantitatively and the build up of the $\beta^+$-activity during irradiation and the decay after irradiation end were investigated. Backprojections of the produced activity were done at different time windows to investigate the shape and time dependency of the activity distributions. Experiments with $^{16}$O beams of 298.5, 300, 301.5 and 303 $A$MeV beams on PMMA targets were performed and it could be shown that the backprojected activity produced by these contiguous energies is resolvable. The broadening of the backprojected $\beta^+$-activity was investigated. The broadening of a 350 $A$MeV $^{16}$O beam was measured using as target a variable water column and further an in-beam PET experiment with the same beam on a water target was performed to compare the broadening of the beam and the broadening of the created $\beta^+$-activity.

Additionally PMMA, water and graphite targets were irradiated with $^{12}$C beams of 260 $A$MeV and measured by means of in-beam PET. The production of $\beta^+$-active nuclei, the backprojected activity and the broadening of the activity were investigated.

## Simulations

The simulations were done in 3 consecutive approaches. Because these investigations started already before the experiments were performed, in the first two approaches, only experiments with $^{12}$C beams performed previously with the in-beam PET at GSI, could be simulated.

In the first approach only the points where $\beta^+$-active nuclei come to rest were scored. This approach showed the need of a more detailed and also time dependent simulation, therefore in the second approach the time structure of the beam was introduced and the position and time of the electron-positron annihilations were scored. Imaging effects due to detection and backprojection were added. Biasing methods were used to reduce the CPU time. These simulations showed the need of modelling also the propagation and detection of the photons.

For the final simulations the data of the experiments was already available. The exact time structure of the beam, the exact positions of the targets and all material in the beam was modelled. The position and time where the annihilation photons leave the target were scored and stored in a file. The PETSIM code, which is used at GSI for predicting the $\beta^+$-activity in therapy, is capable to simulate the response of the in-beam PET and it is also able to store the detected events in the same list mode data format as it is produced in the experiment. PETSIM was modified to read the FLUKA output and to convert it to list mode data files. This way the whole detection process was taken into account. Because the output is stored in the same data format as in the experiments the same backprojection programs could be used for the simulation.

Because of the small solid angle of the double head PET and the limited time for measuring only a few of the simulated annihilation photons contribute to the final backprojection and therefore, CPU time is wasted. Full advantage of the available biasing options in FLUKA was taken and additionally decay direction biasing of annihilation photons was introduced by the FLUKA authors. This leaded to a dramatic decrease of computing time from 100 days down to 100 hours.

For the final simulations a new interaction model, which recently introduced in the development version of FLUKA, was used. This model, based on the Boltzmann Master Equation theory (BME), is aimed to extend FLUKA below 100 $A$MeV which is the present energy threshold of the RQMD model which is responsible for predicting the inelastic nuclear interactions above 100 $A$MeV .

The experiments of the $^{12}$C beams of 260 $A$MeV and of $^{16}$O beams of 200 and 350 $A$MeV were simulated. The influence of the BME model was investigated by doing all simulations twice one time with BME and one time without BME. The total production of $\beta^+$-active nuclei was investigated and spatial distributions of the $\beta^+$-active nuclei were generated. The total productions were compared with the simulations and the distributions of the $\beta^+$-active nuclei were compared between each of the two simulations. Backprojections of the simulated activity were produced at different time windows. The build up and decay of the individual $\beta^+$active

nuclei was investigated.

Good agreement in the shape of the backprojected activity distributions and in the position of the peaks could be observed. It was found that the use of BME improves the distributions but still underestimates the total amount of $\beta^+$-active nuclei produced, especially of $^{15}$O and $^{11}$C. This leads to a gap in the distribution of the created $\beta^+$-active nuclei at the penetration depth corresponding to the transition energy from RQMD to BME. The total production of $\beta^+$-active nuclei is underestimated without BME and is improved by the use of BME.
Further simulations of an $^{16}$O beam with 350 $A$MeV and of a $^{12}$C beam with 260 $A$MeV on water were done where one time the target material was modelled as pure water and the other time with a small amount of gelatine added, like it was done in the experiment. Between these simulations the total amount of $\beta^+$-active nuclei and backprojections were compared. The result of this investigation is that the difference between water and gelatine is negligible.


## Conclusions and outlook

The simulations showed the necessity of using biasing methods because of the limited solid angle of the double head detector. Without the new decay direction biasing for annihilation photons it is not possible to perform the simulations in reasonable computing times.

A problem in the BME model could be identified: Peripheral nuclear collisions where one nucleon is transferred (e.g. $^{16}$O to $^{15}$O or $^{12}$C to $^{11}$C) are underestimated. Therefore, the total produced activity by BME is too low and the distribution of the $\beta^+$-active nuclei shows a gap at the transition from the RQMD model to the BME model.
Work to overcome this problem is on the way.
The not optimal reproduction of the total amounts of $\beta^+$-active nuclei is not a big problem because the in-beam PET method is not used for absolute comparisons.

The backprojection of the simulated activity produced by $^{16}$O beams on PMMA and water targets shows a good agreement with the experimental data, apart from the problem with the transition between RQMD and BME. These two targets are of clinical importance because of their similarity to human tissue.
Once the problem with BME is solved it is expected that the agreement between measured and simulated activity distribution will improve. A dramatic improve can be expected for the $\beta^+$-activity produced in the experiments with $^{16}$O beams of 200 $A$MeV because the relative contribution of $\beta^+$-active nuclei produced by BME is higher than in the experiments performed at higher energies.

Therefore, FLUKA is a good candidate for performing the simulations necessary for in-beam PET in a therapy with $^{12}$C and $^{16}$O beams. However, before FLUKA can be used in clinical routine further benchmarks with inhomogeneous targets and patient data from in-beam PET monitoring in $^{12}$C ion therapy are highly desireable.

# Bibliography

[And04]  V. Andersen, F. Ballarini, G. Battistoni, M. Campanella, M. Carboni, F. Cerutti, A. Empl, A. Fassò, A. Ferrari, E. Gadioli *et al. The FLUKA code for space applications: recent developments.* Adv. Space Res. 34 (2004) 1302–1310

[Ant02]  L. E. Antonuk. *Electronic portal imaging devices: a review and historical perspective of contemporary technologies and research.* Phys. Med. Biol. 47 (2002) R31–R65

[Bal07]  F. Ballarini, G. Battistoni, M. Brugger, M. Campanella, M. Carboni, F. Cerutti, A. Empl, A. Fassò, A. Ferrari, E. Gadioli *et al. The physics of the FLUKA code: Recent developments.* Adv. Space Res., *in Press*

[Bar56]  W. Barkas, W. Birnbaum and F. M. Smith. *Mass-ratio method applied to the measurement of L-meson masses and the energy balance in pion decay.* Phys. Rev. 101 (1956) 778–795

[Bat06]  G. Battistoni, F. Cerutti, R. Engel, A. Fassò, A. Ferrari, E. Gadioli, M. V. Garzelli, J. Ranft, S. Rösler and P. R. Sala. *Recent developments in the FLUKA nuclear reaction models. Proc. 11th Int. Conf. on Nuclear Reaction Mechanisms, Varenna (Italy),* in E. Gadioli. (ed), *Ric. Scient. ed Ed. Perm.* S126 (2006) 483–495

[Bet30]  H. Bethe. *Zur Theorie des Durchgangs schneller Korpuskularstrahlung durch Materie.* Ann. Phys. 5 (1930) 325

[Blo33]  F. Bloch. *Zur Bremsung rasch bewegter Teilchen beim Durchgang durch Materie.* Ann. Phys. 16 (1933) 285

[Bru00]  R. Brun, F. Rademakers and S. Panacek. *ROOT, an object oriented data analysis framework. 23rd CERN School of computing, Marathon (Greece)* (2000) 11–41

[Cav98]  M. Cavinato, E. Fabrici, E. Gadioli, E. Gadioli-Erba and G. Risi. *Boltzmann master equation theory of angular distributions in heavy-ion reactions.* Nucl. Phys A 643 (1998) 15-29

[Cav01]  M. Cavinato, E. Fabrici, E. Gadioli, E. Gadioli-Erba and G. Riva. *Monte Carlo calculations of heavy ion cross-sections based on the Boltzmann Master equation theory.* Nucl. Phys A 679 (2001) 753-764

[Cer06]  F. Cerutti, F. Ballarini, G. Battistoni, P. Colleoni, A. Ferrari, S. V. Förtsch, E. Gadioli, M. V. Garzelli, A. Mairani, A. Ottolenghi *et al. Carbon induced reactions at low incident energies.* Journal of Physics: Conference Series 41 (2006) 212–218

[Cer07]  F. Cerutti. *Private communication*, CERN, 2007

[Col00]  G. Collazuol, A. Ferrari, A. Guglielmi and P. R. Sala. *Hadronic models and experimental data for the neutrino beam production.* Nucl. Instr. Meth. A 449 (2000) 609–623

[Cre06]  P. Crespo. *Optimization of In-Beam Positron Emission Tomography for Monitoring Heavy Ion Tumor Therapy.* Ph.D. Thesis, Technische Universität Darmstadt (2005)

[Deb00]  J. Debus, Th. Haberer, D. Schulz-Ertner, O. Jäkel, F. Wenz, W. Enghardt, W. Schlegel, G. Kraft and M. Wannenmacher. *Bestrahlung von Schädelbasistumoren mit Kohlenstoffionen bei der GSI.* Strahlenther. Onkol. 176 (2000) 211–216

[Eng04]  W. Enghardt, P. Crespo, F. Fiedler, R. Hinz, K. Parodi, J. Pawelke and F. Pönisch. *Charged hadron tumour therapy monitoring by means of PET.* Nucl. Instr. Meth. A 525 (2004) 284–288

[Fas95]  A. Fassò, A. Ferrari and J. Ranft and P. R. Sala. *FLUKA: Performances and applications in the intermediate energy range. Proc. 1st AEN/NEA Specialists' Meeting on Shielding Aspects of Accelerators, Targets and Irradiation Facilities (SATIF 1), Arlington (Texas)* (1995) 287–304

[Fas97]  A. Fassò, A. Ferrari, J. Ranft and P. R. Sala. *New developments in FLUKA modelling of hadronic and EM interactions. Proc. 3rd Workshop on Simulating Accelerator Radiation Environments, Tsukuba (Japan)* in H. Hirayama (ed), *KEK Proceedings 97* (1997) 32

[Fas03]  A. Fassò, A. Ferrari, S. Rösler, P. R. Sala, F. Ballarini, A. Ottolenghi, G. Battistoni, F. Cerutti, E. Gadioli, M.V. Garzelli *et al. The physics models of FLUKA: status and recent developments.* Computing in High Energy and Nuclear Physics (CHEP03), La Jolla, California, (2003), arXiv:hep-ph/0306267

[Fas05]  A. Fassò, A. Ferrari, J. Ranft and P. R. Sala. *FLUKA: A Multi-Particle Transport Code.* CERN-2005-10, INFN/TC_05/11, SLAC-R-773 (2005)

[Fer92]  A. Ferrari, P. R. Sala, R. Guaraldi and F. Padoani. *An improved multiple scattering model for charged particle transport.* Nuc. Instr. Meth. B 71 (1992) 412–426

[Fer94]  A. Ferrari and P. R. Sala. *A new model for hadronic interactions at intermediate energies for the FLUKA code.* P. Dragovitsch, S. Linn and M. Burbank (eds) *Proc. Int. Conference on Monte Carlo Simulation in High Energy and Nuclear Physics* (1994) 277–288

[Fer98]   A. Ferrari and P. R. Sala. *The Physics of High Energy Reactions.* A. Gandini and G. Reffo (eds) *Proc. Workshop on Nuclear Reaction Data and Nuclear Reactors Physics, Design and Safety, Miramare-Trieste (Italy)* (1998)

[Fie05]   F. Fiedler, K. Parodi and W. Enghardt. *The $\beta^+$-activity Production during therapeutic Irradiation with Beams of Protons, $^3He$ and $^{12}C$.* Forschungszentrum Rossendorf, Wiss. Techn. Ber. FZR-423 (2005) 81

[Fie06]   F. Fiedler, P. Crespo, K. Parodi, M. Sellesk and W. Enghardt. *The Feasibility of In-Beam PET for Therapeutic Beams of $^3He$.* IEEE Trans. Nucl. Sci. 53 (2006) 2252–2259

[Fie07]   F. Fiedler. *Anwendungen des in-beam PET Therapiemonitorings auf Präzisionsbestrahlungen mit Helium-Ionen.* Ph.D. Thesis, Technische Universität Dresden (2007), submitted

[GSI99]   *Proposal for a dedicated ion beam facility for cancer therapy.* GSI Nachrichten 1 (1999) 14–16

[Gun04]   K. Gunzert-Marx. *Nachweis leichter fragmente aus Scherionenreaktionenmit einem $BaF_2$-Teleskop-Detektor.* Ph.D. Thesis, Technische Universität Darmstadt (2004)

[Hab93]   T. Haberer, W. Becher, D. Schardt and G. Kraft. *Magnetic scanning system for heavy ion therapy.* Nucl. Instr. Meth. A 330 (1993) 296–305

[Hab04]   T. Haberer, J. Debus, H. Eickhoff, O. Jäkel, D. Schulz-Ertner and U. Weber. *The Heidelberg Ion Therapy Center.* Radiother. Oncol. 73 (2004) S186–S190

[Has96]   B. Hasch. *Die physikalischen Grundlagen einer Verifikation des Bestrahlungsplanes in der Schwerionen-Tumortherapie mit der Positronen-Emissions-Tomographie.* Ph.D. Thesis, Technische Universität Dresden (1996)

[Hig75]   V. Highland. *Some practical remarks on multiple scattering.* Nucl. Instr. Meth. 129 (1975) 497

[ICR70]   *Linear energy transfer.* International comission on Radiation Units and Measurements, ICRU Report 16 (1970)

[ICR05]   *Stopping of Ions Heavier than Helium.* International comission on Radiation Units and Measurements, ICRU Report 73 (2005)

[Jäk01]   O. Jäkel, M. Krämer, C. P. Karger and J. Debus. *Treatment planning for heavy ion radiotherapy: clinical implementation and application.* Phys. Med. Biol. 46 (2001) 1101–1116

[Kra00]   G. Kraft. *Tumor therapy with heavy charged particles.* Prog. Part. Nucl. Phys. 45 (2000) 473–544

[Krä00] M. Krämer, O. Jäkel, T. Haberer, G. Kraft, D. Schardt and U. Weber. *Treatment planning for heavy ion radiotherapy: physical beam model and dose optimization.* Phys. Med. Biol. 45 (2000) 3299–3317

[Lla88] J. Llacer. *Positron emission medical measurements with accelerated radioactive ion beams.* Nucl. Sci. Appl. 3 (1988) 111–131

[Miz03] H. Mizuno, T. Tomitani, M. Kanazawa, A. Kitagawa, J. Pawelke, Y. Iseki, E. Urakabe, M. Suda, A. Kawano, R. Iritani *et al.* *Washout measurement of radioisotope implanted by radioactive beams in the rabbit.* Phys. Med. Biol. 48 (2003) 2269–2281

[Mol48] G. Molière. *Theorie der Streuung schneller geladener Teilchen II, Mehrfach- und Vielfachstreuung.* Z. Naturforschung A 3 (1948) 78–97

[Nud07] B. N. L. National Nuclear Data Center, NuDat 2.3 *website*, http://www.nndc.bnl.gov/nudat2 (2007)

[Pön03] F. Pönisch, W. Enghardt and K. Lauckner. *Attenuation and scatter correction for in-beam positron emission tomography monitoring of tumour irradiations with heavy ions.* Phys. Med. Biol. 48 (2003) 2419–2436

[Pön04] F. Pönisch, K. Parodi, B. G. Hasch and W. Enghardt. *The modelling of positron emitter production and PET imaging during carbon ion therapy.* Phys. Med. Biol. 49 (2004) 5217–5232

[Par02] K. Parodi, W. Enghardt and T. Haberer. *In-beam PET measurements of $\beta^+$-radioactivity induced by proton beams.* Phys. Med. Biol. 47 (2002) 21–36

[Par04] K. Parodi. *On the feasibility of dose quantification with in-beam PET data in radiotherapy with $^{12}C$ and proton beams.* Ph.D. Thesis, Technische Universität Dresden (2004)

[Par05] K. Parodi, F. Ponisch and W. Enghardt. *Experimental study on the feasibility of in-beam PET for accurate monitoring of proton therapy.* IEEE Trans. Nucl. Sci. 52 (2005) 778–786

[Par07] K. Parodi, A. Ferrari, F. Sommerer and H. Paganetti. *Clinical CT-based calculations of dose and positron emitter distributions in proton therapy using the FLUKA Monte Carlo code.* Phys. Med. Biol. 52 (2007) 3369–3387

[Rös01] S. Rösler, R. Engel and J. Ranft. *The Monte Carlo event generator DPMJET-III.* A. Kling, F. Barao, M. Nakagawa, L. Tavora and P. Vaz (eds) *Proceedings of the MonteCarlo 2000 Conference* (2001) 1033–1039

[ROO07] ROOT, *website* http://root.cern.ch (2007)

[Sch96a] W. Scharf and O. A. Chomicki. *Medical accelerators in radiotherapy: past, present and future.* Physica Medica (1996) XII (4) 199–226

[Sch96b] M. Scholz and G. Kraft. *Track structure and the calculation of biological effects of heavy charged particles.* Adv. Space Res. 1-2 (2007) 5–14

[Sch02] D. Schulz-Ertner, T. Haberer, O. Jäkel, C. Thilmann, M. Krämer, W. Enghardt, G. Kraft, M. Wannenmacher and J. Debus. *Radiotherapy for chordomas and low-grade chondrosarcomas of the skull base with carbon ions.* Int. J. Radiat. Oncol. 53 (2002) 36–42

[Sch03] D. Schulz-Ertner, A. Nikoghosyan, C. Thilmann, T. Haberer, O. Jäkel, C. Karger, M. Scholz, G. Kraft, M. Wannenmacher, J. Debus. *Carbon ion radiotherapy for chordomas and low grade chondrosarcomas of the skull base.* Strahlenther. Onkol. 179 (2003) 598–605

[Sis05] J. Sisterson. *A Newsletter for those interested in proton, light ion and heavy charged particle radiotherapy.* Particles 36 (2005) 10

[Som06] F. Sommerer, K. Parodi, A. Ferrari, K. Poljanc, W. Enghardt and H. Aiginger. *Investigating the accuracy of the FLUKA code for transport of therapeutic ion beams in matter.* Phys. Med. Biol. 51 (2006) 4385–4398

[Sor89] H. Sorge, H. Stöcker and W. Greiner. *Relativistic quantum molecular dynamics approach to nuclear collisions at ultrarelativistic energies.* Nucl. Phys. A 498 (1989) 567–576

[Ste82] R. M. Sternheimer, S. M. Seltzer and M. J. Berger. *Density effect for the ionization loss of charged particles in various substances.* Phys. Rev. B 26 (1982) 6067–6076

[Tom03] T. Tomitani, J. Pawelke, M. Kanazawa, K. Yoshikawa, K. Yoshida, M. Sato, A. Takami, M. Koga, Y. Futami, A. Kitagawa *et al.* *Washout studies of $^{11}C$ in rabbit thigh muscle implanted by secondary beams of HIMAC.* Phys. Med. Biol. 48 (2003) 875–889

[Ura01] E. Urakabe, T. Kanai, M. Kanazawa, A. Kitagawa, K. Noda, T. Tomitani, M. Suda, Y. Iseki, K. Hanawa, K. Sato *et al. Spot Scanning Using Radioactive $^{11}C$ Beams for Heavy-Ion Radiotherapy.* Jpn. J. Appl. Phys. 40 (2001) 2540–2548

[Web99] U. Weber and G. Kraft. *Design and construction of a ripple filter for a smoothed depth dose distribution in conformal particle therapy.* Phys. Med. Biol. 44 (1999) 2765–2775

[Wey03] W. K. Weyrather and J. Debus. *Particle beams for cancer therapy.* Clin. Oncol. 15 (2003) 23–28

[Wil46] R. Wilson. *Radiobiological use of fast protons.* Radiology 47 (1946) 487–491

[Win06] W. T. Winter, S. J. Freedman, K. E. Rehm and J. P. Schiffer. *The $^{8}B$ neutrino spectrum.* Phys. Rev. C 73 (2006) 025503

# Acknowledgements

My thanks go first to Professor Hannes Aiginger who guides me already for several years, starting with a project thesis in 2003, later during my diploma thesis and now during my doctoral thesis. I thank him for his support and for giving me the possibility to work at CERN.

Further thanks are addressed to Professor Wolfgang Enghardt who suggested the topic of this thesis and provided me the opportunity for participating in the in-beam PET experiments at GSI. The discussions with him were always very fruitful and inspiring.

I appreciated very much the work with Professor Alfredo Ferrari, my supervisor at CERN. He always encouraged me in my scientific work. I have learned a lot about Monte Carlo methods from him. He always could solve my problems very quickly and his suggestions to improve the simulations were essential for the success of this work.

I am especially thankfull and honored that the three persons mentioned before have recommended me for a CERN fellowship.

Two other persons who gave important contributions to the success of this work are Katia Parodi and Francesco Cerutti. I wish to express my thanks to Katia for her selfless support from organizing the experiments, providing data, discussing the data analysis and many, many other things more. Francesco I am thankful for the long, fruitful discussions about the simulations and the results of the experiments.

Further thanks are addressed to Karin Poljanc for everything she has done for me over the last years. Arousing my interest for in-beam PET and establishing the contact to Professor Enghardt was the basis for this PhD thesis. Without her I would have never started this work. I also want to express my sincere thanks to the team at GSI helping to perform the experiments.

Finally I want to express my gratitude to people in private matters. I want to say a very warm thank you to my friends from the *The Grooveberries* and from the *Fanfare du Sergy*. I always enjoyed making music together. A very special thank you goes to Gerard Depraz and his family who helped me a lot in my everyday life, even if we had a quite high language barrier to overcome.

I also want to thank all my friends and colleagues from CERN, in particular Friedrich and Lucia for the great time we had.

Last but no least I want to thank my family and my friends at home for their love and support. The distance made it difficult to keep in touch but I am sure it was the right decision to go to CERN for writing this PhD thesis.

# FLORIAN SOMMERER

Untere Hauptstraße 27
A-3495 Rohrendorf
Tel.: +43 2732 7671
e-mail: florian.sommerer@cern.ch

## Personal Details

| | |
|---|---|
| DATE OF BIRTH | December $22^{nd}$, 1976 |
| PLACE OF BIRTH | Krems an der Donau, Austria |
| NATIONALITY | Austria |
| MARITAL STATUS | Single |

## Career

| | |
|---|---|
| SINCE JUL 2007 | Postdoc position (Fellow) at CERN |
| JAN 2005 - JUN 2007 | Doctoral student at CERN |
| NOV 2004 | Forschungszentrum Dresden-Rossendorf |
| OCT 2004 | Degree of Diplom-Ingenieur, comparable to Master of Science (MSc) |
| FEB - JUL 2004 | Diploma thesis at Forschungszentrum Dresden |
| SEP - OCT 2003 | Project thesis in *Physical Methods in Medicine*: Literature study about in-beam PET |
| MAY-JUN 2003 | Project thesis in *Neutron Activation Analysis*: Calibration of a loss free counting module |
| APR-MAY 2003 | Project thesis in *Radiochemistry*: Developing of a fast activity estimation system for uranium and thorium ores |
| OCT 1996 | Beginning of Studies of Technical Physics at Vienna University of Technology |
| OCT 1995 - MAY 1996 | Mandatory military service |
| JUN 1995 | High school diploma (Matura) at Bundesrealgymnasium Krems, Austria |

## Language Skills

| | |
|---|---|
| GERMAN | native |
| ENGLISH | excellent |
| ITALIAN | medium conversation, reading, basic writing |
| FRENCH | basic conversation, basic reading, basic writing |

## Informatics Skills

| | |
|---|---|
| OPERATING SYSTEMS | Linux/UNIX, Apple/OS X, MS Windows |
| WORD PROCESSING | MS Office, Open Office, iWork, LaTeX |
| DATA ANALYSIS | ROOT, IDL (Interactive Data Language) |
| PROGRAMMING | C/C++, Fortran, Java, Shell scripting (Bash), Python |
| MONTE CARLO | FLUKA (particle transport code) |
| OTHER | HTML |

## Personal Interests

| | |
|---|---|
| WIND MUSIC | flugelhorn and trumpet at "Echo du Crêt de la Neige", Fanfare du Sergy, since May 2005 |
| JAZZ MUSIC | trumpet at "The Grooveberries", a group of the CERN Jazz Club, since June 2005 |
| SPORT | swimming, hiking, cycling |

## Publications

### Publications in refereed journals

- K Parodi, A Ferrari, F Sommerer and H Paganetti *Clinical CT-based calculations of dose and positron emitter distributions in proton therapy using the FLUKA Monte Carlo code*, Phys. Med. Biol., **52** 3369-3387, 2007

- K Parodi, A Ferrari, F Sommerer and H Paganetti *A MC tool for CT-based calculations of dose delivery and $\beta^+$-activation in proton therapye*, Journal of Physics: Conference Series **74** 012013, 2007

- F Ballarini, G Battistoni, M Brugger, M Campanella, M Carboni, F Cerutti, A Empl, A Fassò, A Ferrari, E Gadioli *et al. The physics of the FLUKA code: Recent developments*, Adv. Space Res., *in Press*

- F Sommerer, K Parodi, A Ferrari, K Poljanc, W Enghardt and H Aiginger *Investigating the accuracy of the FLUKA code for transport of therapeutic ion beams in matter*, Phys. Med. Bio. **51** 4385-4398, 2006

- H Aiginger, V Andersen, F Ballarini, G Battistoni, M Campanella, M Carboni, F Cerutti, A Empl, W Enghardt, A Fassò *et al. The FLUKA code: new developments and application to 1 GeV/n Iron beams*, Adv. Space Res. **35** 214-222, 2005

### Other communications

- F Sommerer, W Enghardt, A Ferrari, F Fiedler and K Parodi, *FLUKA Simulations for In-beam PET Monitoring*, Oct 2006, Gent, Belgium, European Workshop on Monte Carlo Treatment planning, talk

- K Parodi, A Ferrari, F Sommerer and H Paganetti, *CT-based calculations of dose and positron emitter distributions in proton therapy using the FLUKA Monte Carlo code*, Oct 2006, Gent, Belgium, European Workshop on Monte Carlo Treatment planning, talk by K Parodi

- F Sommerer, W Enghardt, K Parodi, K Poljanc, H Aiginger, *Simulationsrechnungen zur Validierung des Monte Carlo Codes FLUKA für die Vorhersage der bei Tumorbestrahlungen mit Ionen erzeugten $\beta^+$-Aktivität*, Sep 2004, Linz, Annual meeting of the Austrian Physical Society, talk

- F Sommerer, K Parodi, K Poljanc, A Ferrari, W Enghardt and H Aiginger, *Modelling the interaction of therapeutic ion beams with matter by means of* FLUKA, Wiss.-Techn. Ber. FZR-423, 2005, Institute of Nuclear and Hadron Physics, Forschungszentrum Dresden, annual report